ULSAN NATIONAL INSTITUTE OF
SCIENCE AND TECHNOLOGY

Doctoral Thesis

Synthesis and characterization of surface engineered nanomaterials via catechol derivatives

Hyunhong Kim

Department of Chemical Engineering

Graduate School of UNIST

2020

ULSAN NATIONAL INSTITUTE OF
SCIENCE AND TECHNOLOGY

Synthesis and characterization of surface engineered nanomaterials via catechol derivatives

Hyunhong Kim

Department of Chemical Engineering

Graduate School of UNIST

ULSAN NATIONAL INSTITUTE OF
SCIENCE AND TECHNOLOGY

Synthesis and characterization of surface engineered nanomaterials via catechol derivatives

A thesis/dissertation
submitted to the Graduate School of UNIST
in partial fulfillment of the
requirements for the degree of
Doctor of Philosophy

Hyunhong Kim

12.09.2019
Approved by

____
Advisor
Jongnam Park

Synthesis and characterization of surface engineered nanomaterials via catechol derivatives

Hyunhong Kim

This certifies that the thesis/dissertation of Hyunhong Kim is approved.

12.09.2019

signature

Advisor: Jongnam Park

signature

Sebyung Kang

signature

So Youn Kim

signature

Jae Sung Son

signature

Sung You Hong

Abstract

All nanomaterials exhibit large surface to volume ratio in common and their surfaces have great influence with physicochemical properties of them. Therefore, surface engineering of nanomaterials is key to the utilization of unique nanomaterials properties and flexible strategies for deign of advanced materials. In this respect, catechol based nanocoating have been significantly attracted for application of nanocrystals and functionalization of substrates because of its adaptability to universal surface and high affinity in harsh condition. This dissertation demonstrates fabrication and characterization of nanocoating through amine mediated redox modulation of catechol. Synthetic mechanism of the nanocoating was suggested and surface engineering of metal oxide nanoparticles by the coating method have been studied. In addition, compact, biocompatible, and charge modulated iron oxide nanoparticles were synthesized and its bio-application was reported.

First, conformal nanocoatings to nanostructured materials was achieved through amine-mediated redox control of a catechol system by separating catechol and amine, which effectively suppress cohesion and enhance a adhesion to yield an optimized nanocoating. The amine-assisted catechol nanocoating exhibits roughness of <0.358 nm and thickness of 1.69 nm on flat substrates; the hydrodynamic diameter of coated iron oxide nanoparticles is less than 20 nm. Surface characterization, density functional theory calculations, and effect of separated amine were investigated to elucidate the coating mechanism. Three key roles of separated amine in the catechol-based nanocoating were suggested as follows, adhesion promotion, suppression of polymerization, and additional stabilization through an in-situ generated, newly designed catechol-amine adduct.

Second, multidentate catechol based polyethylene glycol random copolymer ligands was synthesized by reverse addition and fragmentation transfer polymerization. Compact, biocompatible and colloidal stable iron oxide nanoparticles have been synthesized by the ligands via the amine assisted catechol nanocoating method and applied into *in vivo* magnetic resonance contrast agents. High resolution magnetic resonance angiography with long circulation time was reported.

Finally, charge modulated metal oxide nanoparticles were synthesized by surface engineering with multidentate catechol based polymeric ligands. The charged iron oxide nanoparticles exhibit different behavior *in vitro* cell experiments and gene delivery into cell by positive charged nanoparticles was demonstrated.

Contents

List of Figures

reproduced from ref. 24, National Academy of Sciences. Panel d-h reproduced from ref. 25, AAAS.

Figure 1.8. (a) Structure of cyclic trichrysobactin. (b) Mechanism of mica modification through amine functional catechol. Panel a reproduced from ref. 27, AAAS. Panel b reproduced from ref. 28, Wiley-VCH.

Figure 1.9. (a) Key amino acid in Mfp-3s and its synthetic analogue copolymer. (b) Charge of Mfp mimetic zwitterion catecholic molecule. Panel a reproduced from ref. 29, American Chemical Society. Panel b reproduced from ref. 30, Nature Publishing Group.

Figure 1.10. (a) I. Schematic illustration of the assembly of tannic acid and iron ion on a various substrates. II. Tannic acid assembly (green) on protein loaded $CaCO_3$ (red) particles. (b) I. poly phenol rich grape, cacao, and green tea. II. Molecular structures of polyphenol derivatives from nature. III. Polyphenol coatings. IV. Colorless polyphenol coating on glass with red wine. $AgNO_3$ treatment for visualization of coating layer (right). Panel a reproduced from ref. 31, AAAS. Panel b reproduced from ref. 19, Wiley-VCH.

Figure 1.11. Mechanism of reduction by cysteine rich Mfp-6. The DOPA adsorb directly on rock surface and the oxidized DOPA are reduced by thiol of cysteine. The adhesion of DOPA is recovered and the cohesion of oxidized DOPA are suppressed. Adapted from ref. 32 with permission from Nature Publishing Group.

Figure 2.1. (a) Rhombohedral primitive unit cell of Fe_3O_4. (b) Inverse spinel structure of Fe_3O_4. (c) Side view of the slab model with (001) surface of Fe_3O_4, which is a (1 × 2) supercell extended from a $\left(\sqrt{2}\times\sqrt{2}\right)\mathbf{R45^\circ}$ unit cell. The fixed bottom layer in the slab model is colored orange, and V_{Fe} indicates the tetrahedral Fe^{3+} sites that were removed to eliminate the *z*-directional dipole effect of the surface. (d) Top view of (001) surface showing only the top layer. (e) Molecular structures of 4-*tert*-butylbenzo-1,2-quinone (left) and AEE molecule (right). Carbon atoms in the benzene group are numbered in the clockwise direction.

Figure 2.2. (a) Schematic illustration of catechol coating on metal oxide surface with only TBC (above) and with addition of AEE (below). (b) AFM images of TBC-only coating (TBC 0.5 mmol/ml, pH 10) and (c) mixture of TBC and AEE coating (TBC 0.5 mmol/ml, TBC:AEE = 1:20) after 24 h of coating. (b) Thicknesses of TBC and TBC-AEE films versus time. The TBC film was analyzed by alpha-step, and the TBC-AEE film was measured by AFM. XPS C 1s spectra of (e) TBC-only on sapphire and (f) TBC-AEE. (g) Carbon K-edge X-ray absorption fine structure spectra of TBC (black) and TBC-AEE (red) coated on sapphire wafers. The data were collected in PEY mode with an incident angle of the linearly polarized X-ray beam of 55°.

peak occurs at 401.2 eV along with the amide bond signal, which means that secondary amines exist on the surface of IONPs.

Figure 2.12. FT-IR spectra of as-syn IONPs, CP, IONP@CP, and IONP@CP with AEE. Surfaces of IONPs after coating were also analyzed by FT-IR.

Figure 2.13. (a) Photographs of CP-coated 12 nm Fe_3O_4 and Fe_2O_3 NPs in THF with water additives. Aggregation was detected only in Fe_2O_3 NP samples. (b) DLS data of CP coated on Fe_2O_3 NPs in THF with water, TEA, and AEE additives.

Figure 2.14. (a) Adsorption forms of TBC and TBC-AEE on a tetrahedral Fe^{3+} site in bidentate chelating mode (left) and on octahedral Fe^{2+} and Fe^{3+} sites in bidentate bridging mode (right), where only the top of surface layer is shown. The insets indicate each adsorption mode, and subscripts (t) and (o) indicate tetrahedral Fe^{3+} and octahedral Fe^{2+} and Fe^{3+} TBC adsorption sites, respectively. (b) Adsorption energies of TBC and TBC-AEE on Fe_3O_4 (001) surface. The terms ‘C3,’ ‘C5,’ and ‘C6’ denote TBC-AEE(Cx) molecules on the Fe_3O_4 (001) surface where the AEE molecule is bound at C3, C5, and C6 sites, respectively. The colored dashed lines in the graph indicate average adsorption energies of TBC and TBC-AEE(Cx) molecules.

Figure 2.15. (a) Relative energy profiles referenced to the total energy of Step 1. Step 1 to Step 4 indicate the reaction process for the reduction of quinone to TBC with the aid of AEE. Note that Cx-Oy (i.e., $x = 3, 5, 6$, $y = 1, 2$) indicates the reaction path where AEE is bound on the Cx site and Oy is preferentially reduced. (b) Schematic representation of the reaction procedure. O1 and O2 represent the preferentially reduced oxygen sites in the reaction. Inset shows the detailed reduction procedure of oxygen atoms in the case of C6-O1.

Figure 2.16. Adsorbed forms of TBC and TBC-AEE on (a, c, e, g) a tetrahedral Fe^{3+} site in bidentate chelating mode and on (b, d, f, h) octahedral Fe^{2+} and Fe^{3+} sites in bidentate bridging mode. ‘C3,’ ‘C5,’ and ‘C6’ denote TBC-AEE molecules on the Fe_3O_4 (001) surface where the AEE molecule is bound at the C3, C5, and C6 site, respectively. Subscripts (t) and (o) indicate tetrahedral Fe^{3+} and octahedral Fe^{2+} and Fe^{3+} adsorption sites for TBC, respectively.

Figure 2.17. (a) Proposed mechanism for the formation of a catechol coating with no AA. Catechol loses its adhesion properties due to oxidation. Catechol-Fe^{3+} coordination on the substrate and electron transfer between catechol and Fe^{3} (left) occur, but the catechol-Fe^{2+} coordination maintains its bonding. The reduced Fe^{2+} ion elutes from the surface to the solution, and the oxidized catechol moves to the nearby iron ion (middle). Additional oxidation of the semiquinone causes detachment of the ligand in quinone form (right). (b) Proposed mechanisms for the formation of AANC. In the

Figure 4.4. Characterization of Fe3O4 NPs. (a) TEM images of Fe3O4 NPs before and after ligand exchange with DOPA-Tertiary amine (positive), DOPA-mPEG (neutral), and DOPA-Sulfonic acid (negative). (b) DLS and zeta-potential of Fe3O4 NPs with different surface ligands (positive, neutral, and negative) (c) Images of ligand exchanged MNPs dispersed in various aqueous solutions. Results showed that surface modified Fe3O4 NPs were stable in various pH values and 1 M NaCl solution.

Figure 4.5. (A) DLS analysis to observe the stability of ligand exchanged MNPs in 1X PBS, DI water, buffer at pH ranging from 5 to 11 and in 1 M NaCl solution.

Figure 4.6. (a) Oleic acid coated Fe_3O_4 NPs, (b) MNP@DOPA-Tertiary amine, (c) MNP@DOPA-mPEG, (d) MNP@DOPA-Sulfonic acid. Images show the distribution of selected ligands in micro-size pattern of Fe_3O_4 NPs. (mc = maximum counts in one pixel, scale bar = 50 μm). (e) Table of molecular weights, fragment ions and assigned ligands of ToF-SIMS secondary positive and negative ions obtained from ligand-conjugated Fe_3O_4 NPs.

Figure 4.7. ToF-SIMS spectra of positive and negative ions related to Fe_3O_4 NPs and their ligands (a)-(c). The first layer shows free ligand and second layer represents ligand-conjugated Fe_3O_4 NPs; (a) tertiary amine, (b) PEG, and (c) sulfonic acid. Iron-related ions of Fe_3O_4 NPs ($[Fe]^+$ and $[FeO_2]^-$) are indicated by blue diamonds and fragment ions of polymer ligands for tertiary amine, PEG, and sulfonic acid are indicated by orange diamonds.

Figure 4.8. ToF-SIMS images of positive ions from PEG treated Fe_3O_4 NPs without an anchoring group. This image shows the distribution of Fe_3O_4 NPs- and PEG-related fragment ion in an area with micro-sized aggregations patterns. The spatial distribution of the $[(OCH_2CH_2)_2CH_3]^+$ ion was not overlapped with the Fe^+ distribution, indicating that the PEG ligands were not bound to the Fe_3O_4 NP surface.

Figure 4.9. FT-IR images of (a) MNP@DOPA-Tertiary amine, (b) MNP@DOPA-mPEG, and (c) MNP@DOPA-Sulfonic acid. FT-IR images obtained from related peaks of ligand-conjugated Fe3O4 NPs for anchoring group (ν(C=O)) and characteristic functional groups ((a) tertiary amine ligand (ν(C–N)), (b) PEG ligand (νas(C–O–C)), and (c) sulfonic acid ligand (ν(SO3))). ToF-SIMS images (d-f) show the [Fe2O]+ ion distributions from the same area that the FT-IR images were measured. (scale bar = 100 μm). (g) Assigned functional group of FT-IR vibrational modes of free ligands and ligand-conjugated NPs.

Figure 4.10. FT-IR spectra of (a) positively charged Fe_3O_4 NPs, (b) neutral Fe_3O_4 NPs, and (c) negatively charged Fe_3O_4 NPs. The first layer shows free polymer ligands and the second layer represents (a) tertiary amine, (b) PEG, and (c) sulfonic acid-coated Fe_3O_4 NPs, respectively.

List of Tables

List of Schemes

List of Abbreviation

IONP	Iron oxide nanoparticles
DMA	Dopamine methacrylamide
AIBN	Azobisisobutyonitrile
RAFT	Reversible addition-fragmentation chain trasfer
PEG	Poly(ethylene glycol)
DLS	Dynamic light scattering
FPLC	Fast protein liquid chromatography
GPC	Gel permeation chromatography
AEE	2-(2-aminoethoxy) ethanol
DOPA	3,4-dihydroxylphenylalanine
Mfp	Mussel foot protein
HMDA	Hexamethylenediamine

Chapter 1. Surface engineered nanomaterials and dissertation overview

1.1 Introduction

Surface engineering of nanoparticles have been researched for wide application field and fundamental studies, because of inherent large surface to volume properties of nanomaterials. Surface of nanoparticles has great influence to intrinsic characteristic of nanoparticles including solubility, conductivity, catalytic activity, stimuli responsibility and photoluminescence. All of the factors directly affect to synthetic mechanism, processing and application of nanoparticles. Traditionally, high quality nanoparticles have been synthesized in thermal-decomposition of metal precursor, solvothermal in organic solvent, and reduction method in aqueous solution with surfactant, which can effectively lower surface energy of unstable surface of particles. Although, high crystallinity, narrow size distribution, controllable size and morphology have been achieved by the above mentioned synthetic techniques in various kinds of nanocrystals such as transition metal oxide, noble metal, semiconductor, and rare earth metal oxide nanoparticles, the resultant nanoparticles involve ligand adsorbed surface which is especially a long hydrocarbon tethered anchor (Figure 1).[1] In most of application, the inherent long hydrocarbon chain functionalized nanocrystals limit their usage potential. To overcome the issues for biocompatible nanomaterials, ligand exchange can be one of the most effective strategies to endow water-dispersibility to nanoparticles by direct replacement of hydrophobic ligand to desired surface (Figure 2).[2] The direct ligand exchange have advantage to compact size and facile functionalization compared to previously micellization by amphiphilic molecules and silanization method. Among the binding anchor groups, catechol derivatives have been attracted as ligand for synthesis of biocompatible nanomaterials because their high binding affinity to metal oxide even in harsh sea water condition and versatility to universe substrates. Nanocoatings on substrates have been successfully fabricated through controlled polymerization of dopamine and polyphenol derivatives, coacervation of catecholic zwitterions, salt replacement by catechol with flexible amino groups, and coordination complexes of polyphenols and Fe^{3+} ions. Although these film fabrication methods represent the state-of-the-art in the substrate nanocoating field, their application to nano-sized materials with high curvatures has been limited. Mussel-inspired nanocoatings on inorganic nanoparticles have depended on dopamine and catechol derivatives; however, degradation and etching, heterogeneous coating layers, and agglomeration of NPs due to unstable and thick coating layers compared with original NP sizes have been reported as challenging issues. Fabrication of delicately surface modulated nanoparticles has still been limited because of above issues and as a result, it is meaningful to apply and study for stable, uniform and compact sized surface engineered nanoparticles to *in vitro* and *in vivo* bio-application.

In this chapter, the research background and trends for catechol-based coating on nanomaterials will be discussed.

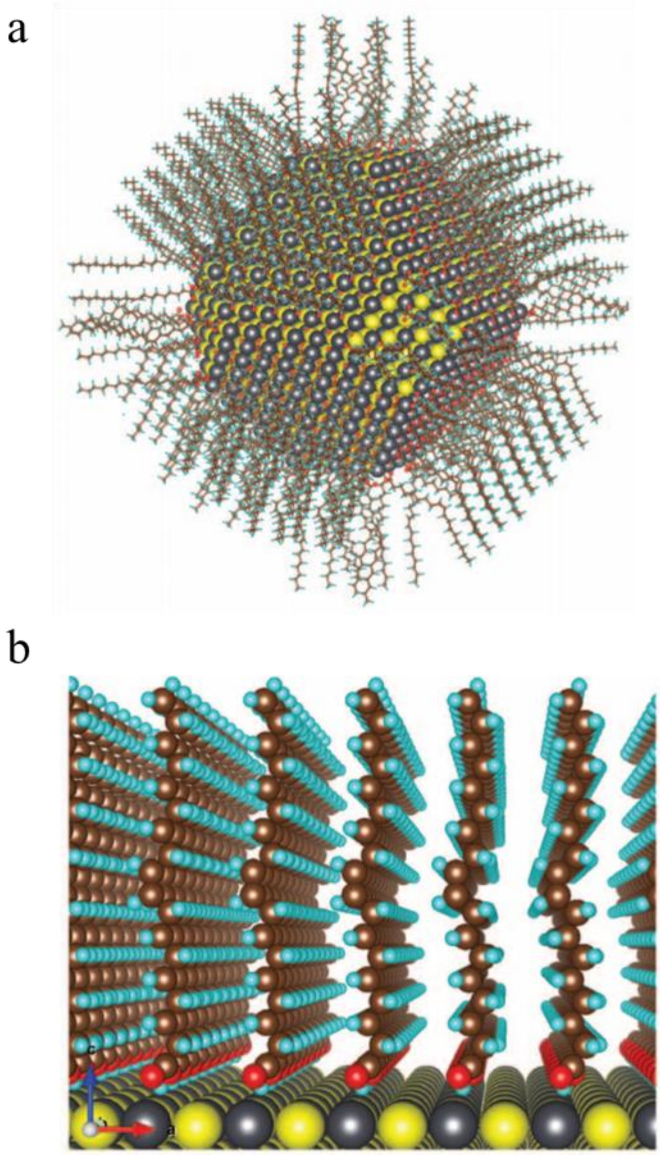

Figure 1.1. (a) Calculated atomic illustration of oleic acid passivated PbS nanoparticles. (b) Configuration of oleic acid molecules on the PbS(001) surface. The figure is reproduced with permission from ref. 1, AAAS.

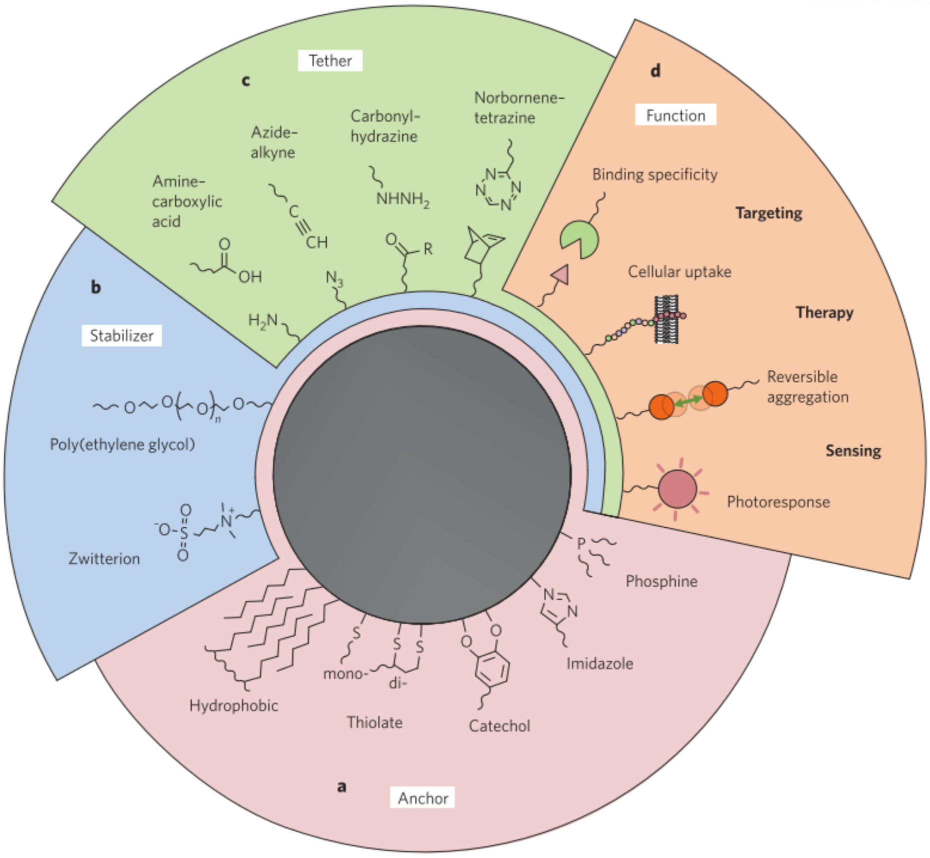

Figure 1.2. Representative design of ligands for biocompatible nanoparticles. (a) Various anchor group, (b) Hydrophilic group for water solubility and non-specific binding properties, (c) Functional group for conjugation reaction, and (d) biomolecule conjugation for bioapplication. The figure is reproduced with permission from ref. 2, Nature Publishing Group.

1.2 Previous researches on surface engineered nanomaterials

1.2.1. Micellization via amphiphilic molecules

Hydrophobic organic ligands coated nanocrystals is the main challenge for expansion of their application, especially in biological application. Phospholipid and glycocluster amphiphile encapsulated quantum dots were known as first approaches of surface engineered nanoparticles (Figure 3).[3-5] The amphiphilic molecules are a kind of surfactant and have a characteristics about micelle formation. A hydrophobic tail stabilizes the hydrophobic nanocrystals and a hydrophilic head comprises a dense layer of biocompatibility and water solubility. From the encapsulation method, high colloidal stability and passivation of surface from external chemicals are achieved in aqueous phase through rigid core protection layer. However, modulation of functionalization of nanoparticles except for charge and hydrophilic group is difficult due to intrinsic properties of core-shell structured micelle. Additionally, enlarged hydrodynamic diameter of nanocrystals because of inner hydrocarbon shell limit renal clearance, access to a crowded neuronal synapse, and penetration to connected cells.

1.2.2. Silica coatings

Silica coated nanoparticles have been widely used surface engineering method due to facile surface chemistry, biocompatibility, high transparency and its controllable porosity. Sol-gel method on the nanoparticles through hydrolysis/condensation of a

tetraethyl orthosilicate is established (Figure 4). For the procedure, hydroxyl group is required to facilitate the hydrolysis and condensation of silicon alkoxide. For example, hydorxyl group functional citrate capped gold NPs and dextran coated IONPs induce robust silica shell layer on their surface.[6] Molecular transformation of polyvinylpyrrolidone (PVP) to enol form can be also one of the example of hydroxyl functionalization of PVP coated nanoparticles.[6, 7]

Silica coating through reverse microemusion is synthetic method for hydrophobic nanoparticles.[8] Silica precursor is injected to hydrophobic nanoparticles in cyclohexane with surfactant and ammonium solution. Then, silica encapsulated nanoparticles is produced and the thickness of silica shell can be controlled by synthetic parameters.

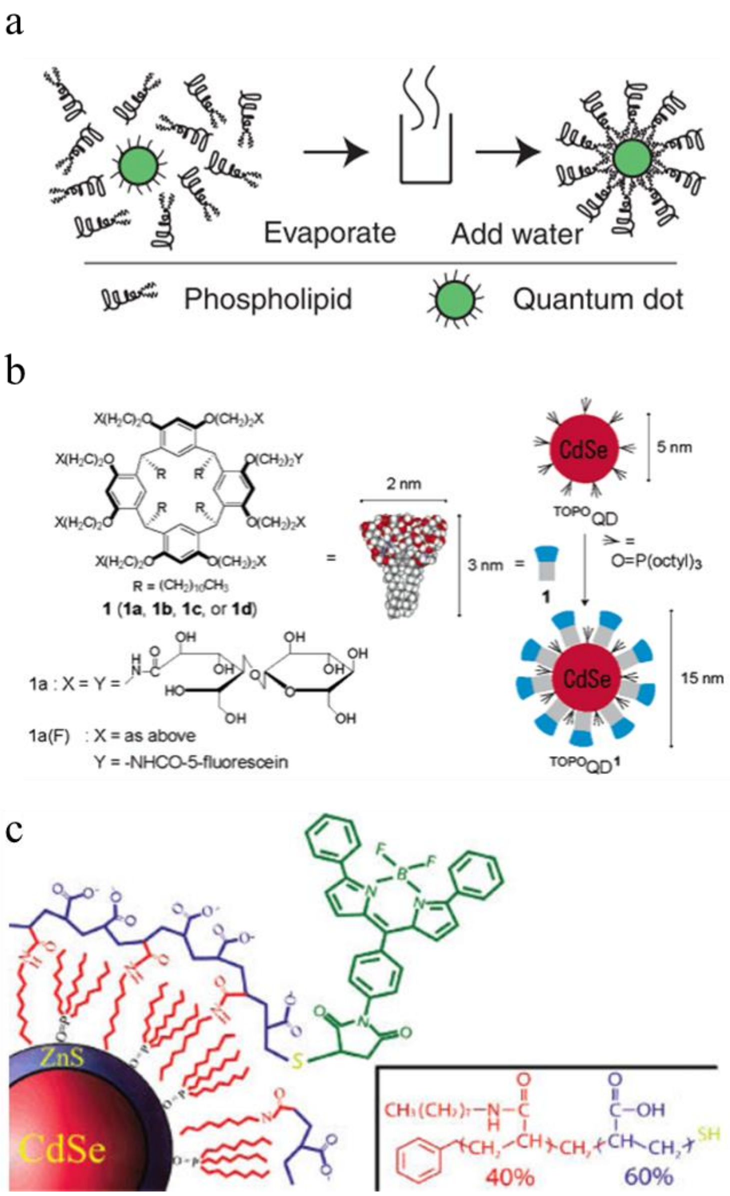

Figure 1.3. Encapsulation of nanoparticles using (a) phospholipid derivatives[3], (b) glycocluster amphiphile[4], and (c) octyl amine modified poly acrylic acid[5]. Panel **a** reproduced from ref. 3, AAAS, Panel **b** reproduced from ref. 4, American Chemical Society, Panel **c** reproduced from ref 5, American Chemical Society.

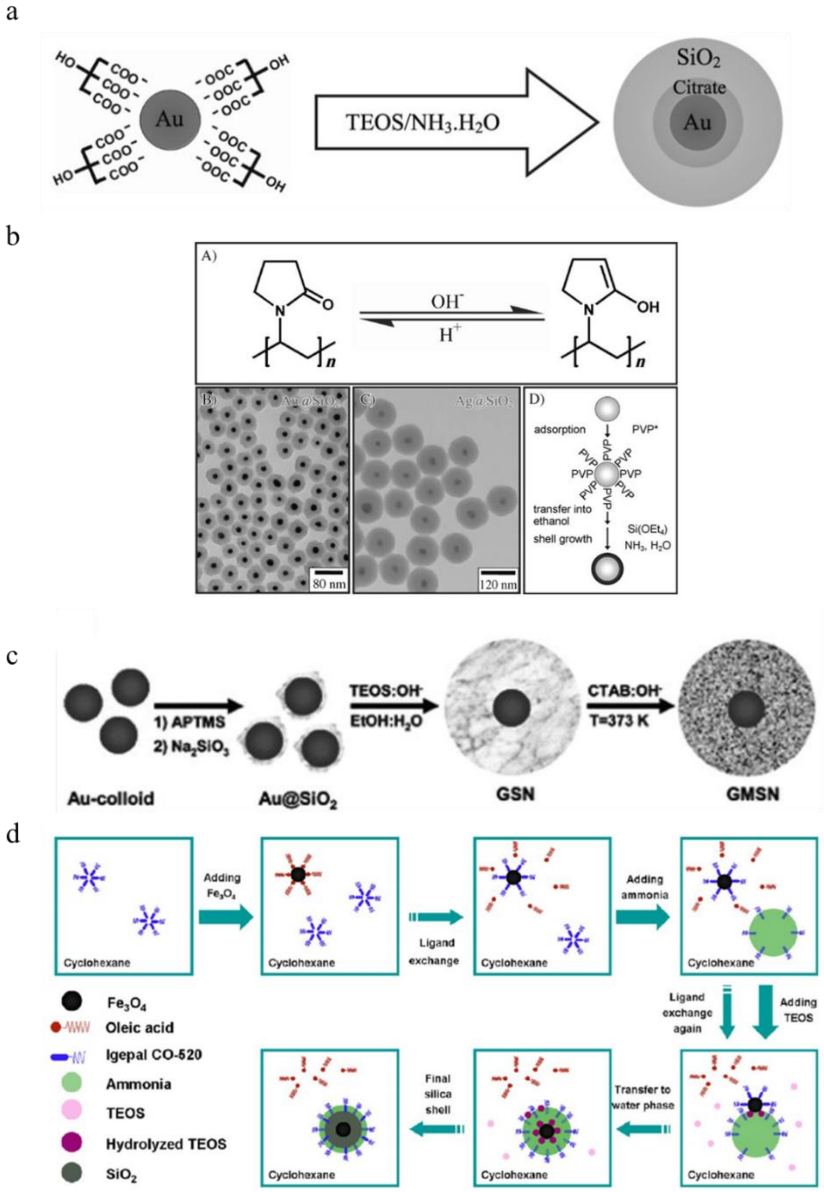

Figure 1.4. Synthetic illustration of silica coating on (a) citrate capped nanoparticles[6] and (b) PVP stabilized nanoparticles[6], Synthetic scheme of (c) mesoporous silica coated nanoparticles[6] and (d) silanization through reverse microemulsion method[8]. Panel a-c reproduced from ref. 6, Wiley-VCH. Panel d reproduced from ref. 8, American Chemical Society.

1.2.3. Direct ligand exchange via monodentate ligands

Ligand exchange strategies of nanoparticles is direct covalent attachment of ligands to the nanoparticle surface with bifunctional hydrophilic ligands.[9] The ligands consist of metal coordinating anchor group and functional group simultaneously. For example, monothiol ligands such as mercaptoacetic acid, mercaptopropionic acid, cystamine, and cystein have been used to stabilize quantum dots (Figure 5). The L-type ligands exhibit high binding affinity to quantum dot surface so, facilitate desorbing the formal ligands from surface. In contrast quantum dots, X-type ligands such as phosphate, catechol, and carboxyl function are established for their high binding affinity on metal oxide nanoparticles.[10, 12] High negative charge density on surface of nanoparticles is induced from the small monodentate molecules and it is advantageous for water solubility of nanoparticles. Low stability in acidic solution and non-specific binding properties of the monodentate ligands was overcome through the development of polyethyleneglycol linked bidentate thiol ligands. The new class of ligands also contains functional group such as hydroxyl, carboxylic acid, and biotin for conjugation with biomolecules.

1.2.4. Direct ligand exchange via multidentate polymeric ligands

Although the monodentate ligand based cap exchange reaction is facile strategies for providing functional surface to nanoparticles, its low binding stability from the dynamic binding interaction between the anchor and nanoparticles make them to have short colloidal stability in solution. Detachment of surface ligand cause non-specific binding in cellular application and decrease of quantum yield of quantum dots. To overcome the inherent low binding affinity of monodentate ligands, multiple pendent anchor group along the polymer backbone have been researched (Figure 6). Multiple lipoic acid[13], catechol[14], and imidazole[15] function included polymeric ligands were reported and their enhanced pH/ionic stability was proved.

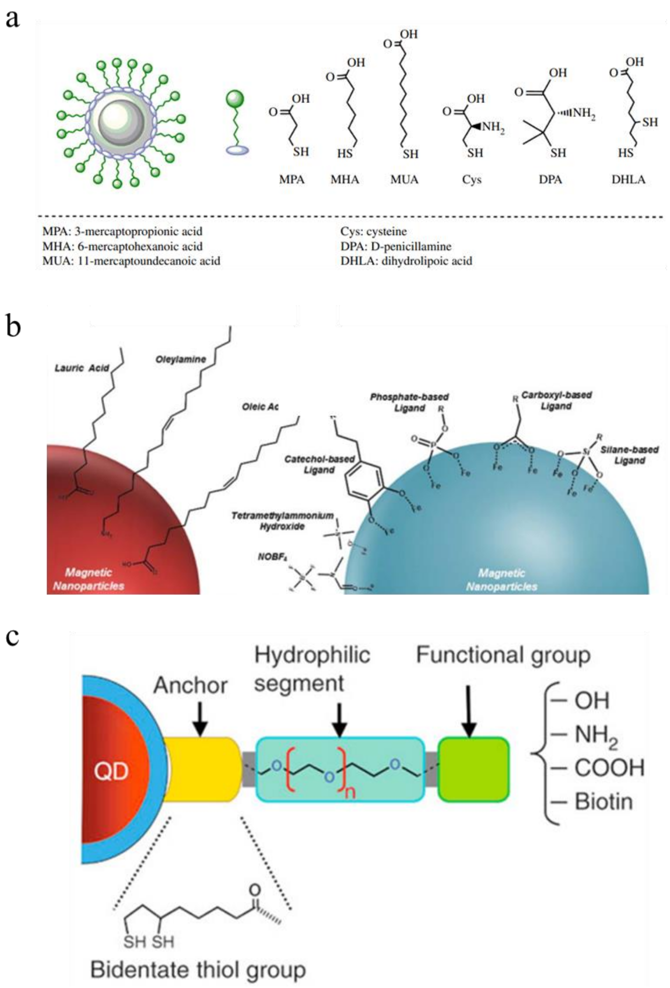

Figure 1.5. Monodentate molecules with affinity towards (a) the noble metal nanoparticles and quantum dots[9], (b) metal oxide nanoparticles[10]. PEG tethered bidentate ligands with various terminal functional group[11]. Panel a reproduced from ref. 9, The Royal Society Publishing. Panel b reproduced from ref. 10, The Royal Society Publishing. Panel c reproduced from ref. 11, American Chemical Society.

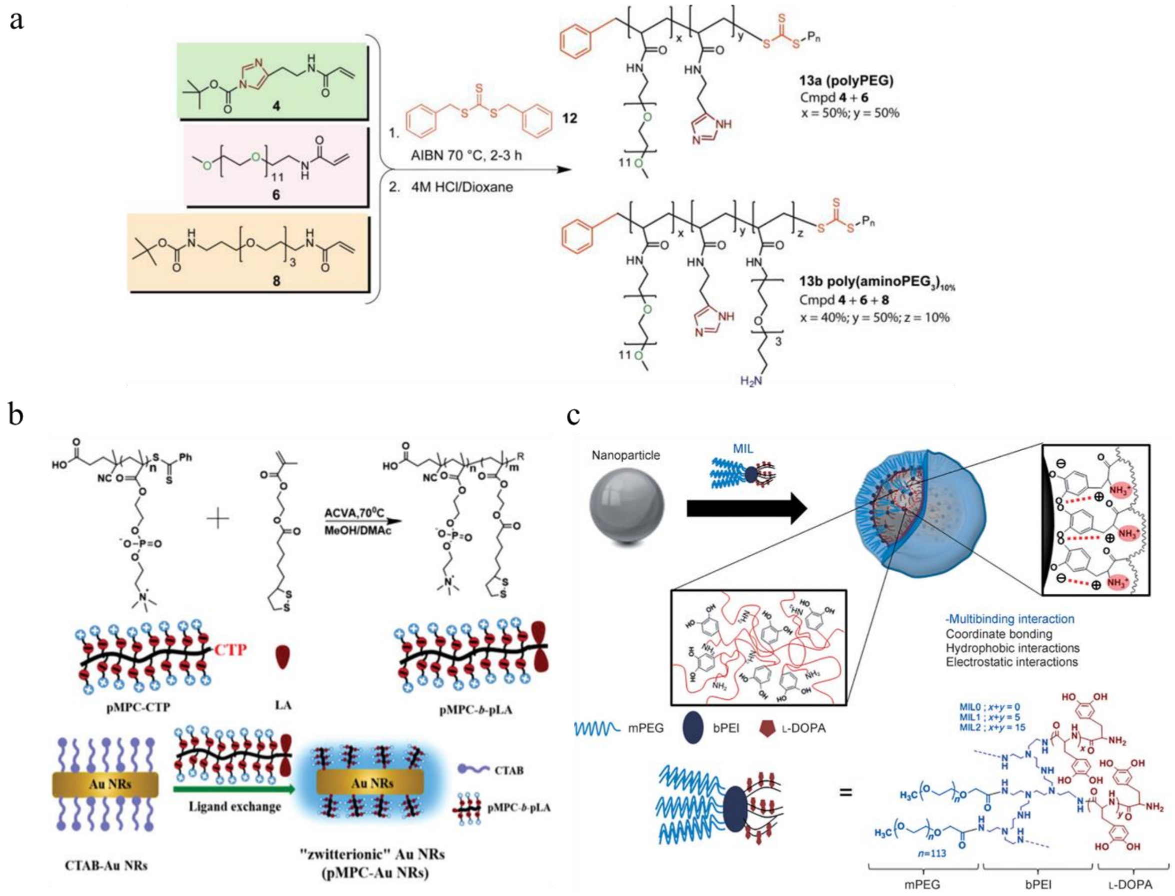

Figure 1.6. Synthetic scheme of (a) reverse addition fragmentation transfer mediated synthesized multidentate imidazole-based random copolymer[12], (b) multidentate lipoic acid block copolymer[13], and (c) multidentate DOPA-based polymer[14]. Panel **a** reproduced from ref. 12, American Chemical Society. Panel **b** reproduced from ref. 13, The royal society of chemistry. Panel **c** reproduced from ref. 14, Wiley-VCH.

1.3 Catechol chemistry related to surface engineering: Research background

1.3.1. Introduction of catechol chemistry

Catechol is a 1,2-hydroxylbenzene and its derivatives are prevalent in surrounding nature including mussels[16], sandcastle worms[17], squids[18], teas[19], and fruits. Among them, marine mussel lives on rocks even under harsh sea water condition contains lots of salt, basic pH, and microorganism against wind and wave.[20] A catechol containing DOPA in Mfp is a crucial amino acid related to adhesive characteristics of mussel so, extensive studies about DOPA have been researched to copy their high adhesion performance (Figure 7a).[21] Current molecular control of surface has depended upon thiol, silane, and phosphonic group however, requirement of oxide free surfaces, low stability, and non-uniform layer are impediments to further use. Mfp-3 and Mfp-5 which is prominent at the interface contain high amount of DOPA contents ~25% so lots of paper have focused to the DOPA to mimic them as synthetic polymers containing catechol as adhesive.[22] For fabrication of stable and uniform nanocoating layer, a specific anchor group of adsorbates such as catechol is essential due to its high adhesion capability. However, the adhesion force of DOPA included chemicals is controversy and remains unclear.[23, 24] Oxidative vulnerability of catechol decrease the affinity to substrate and the unique oxidative properties are origin of complex catechol based cohesion properties. Loss of affinity to substrate and uncontrollable polymerization induced from the oxidized catechol, quinone are not still fully identified. Lysine is another rich amino acid related to adhesion properties and has been adopted to enhance adhesion. Dopamine is a representative molecules for universal coating reagent which is amine function tethered catechol. Although the high adhesion properties can be achieve by combination of catechol and amine, the uncontrollable cohesion limit their application potential (Figure 7b). Polymerization of dopamine go through via 5,6-dihydroxyindole intermediate which is generated from intramolecular amine addition to quinone.[25] Recently, not only covalent reaction but also, physical pathway involves cation-π, π-π stacking, and hydrogen bond is revealed as a one of coating mechanism of dopamine by Hong et al.[26]

Although the mussel inspired dopamine exhibited excellent adhesion and cohesion properties in basic condition, susceptibility to air oxidation of DOPA deteriorate affinity of DOPA. To overcome the phenomenon, the real mussel secreted cysteine rich Mfp-6 to recover oxidized DOPA to fresh one through thiol mediated reduction process (Figure 11).[27]

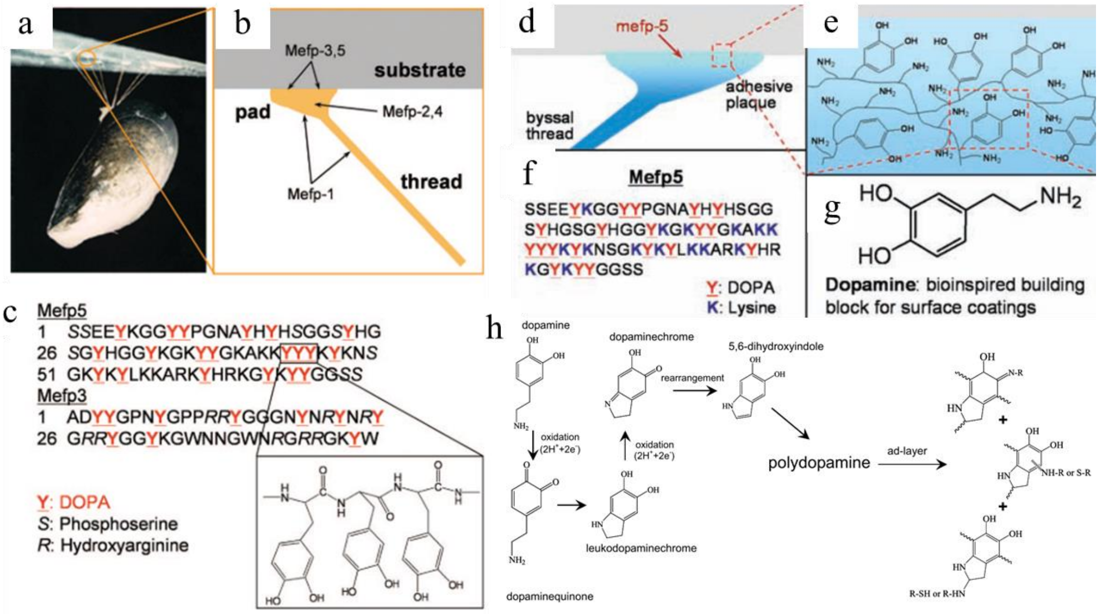

Figure 1.7. (a) Photograph of mussel foot protein of *M. edulis*.[24] (b) Scheme of the bio-distribution of Mfp. (c) Amino sequence of Mfp-3 and Mfp-5. (d) Illustration of Mfp-5 and (e and f) its amino sequence.[25] (g) Molecular structure of dopamine. (h) Mechanism of polydopamine coating. Panel **a-c** reproduced from ref. 24, National Academy of Sciences. Panel **d-h** reproduced from ref. 25, AAAS.

1.3.2. Introduction of catecholic based nanocoating

By optimizing the molecular structure of amine functional catechol, catechol based nanocoating layer have been achieved. One of the example is cyclic trichrysobactin which contains derivatives of 2,3-dihydroxybenzoic acid and lysine in a molecule (Figure 8a).[28] The lysine of the structure evicts hydrated cations from the substrates resulting adsorption of cyclic trichrysobactin derivatives to substrates. Extremely simplified amino group linked catechol anchor also have been proved for its nanocoating ability (Figure 8b).[29] In Figure 9a, synthetic copolyampholytes inspired by a Mfp were introduced. Seo et al. focused key functional amino sequence of Mfp-3s involving DOPA, cationic, anionic, non-ionic polar and non-polar group.[30] The synthetic copolymer exhibited coating layer under 3 nm and high adhesion force under water. In the paper, electrostatic and hydrophobic interactions with catechol group are significant for wet adhesion and coacervation. Similar approaches from the catecholic zwitterionic surfactants was proposed for nanocoating layer (Figure 9b). Molecularly smooth, ultrathin, and high adsorption force was achieved via the molecules. Aggregates as coacervates above the critical aggregation concentration, uniformly distributed the coacervates on the substrates, and rearrangement of the coacervates as bilayers occurred during coating procedure.

Polyphenol nanocoating through tannic acid and Fe(III) ions was described by Ejima et al. in 2013 (Figure 10a). The low cost and facile coating mechanism on universal substrates have been widely after the paper. Fe(III) ion act as crosslinker and the resultant tannic acid aggregates deposited on surface. Multifunctional coating by trihydroxyphenyl containing molecules have also been established as thin coating fabrication method (Figure 10b). The method has similar mechanism with polydopamine but, the method provide colorless coating layer and cost-effective compared to polydopamine coating. The coating mechanism of the method has not been revealed but, the authors ascribed that oxidation of polyphenol induce decrease solubility via polymerization and enhanced adsorption own affinity of increased number of anchor to surface may facilitate surface coating.

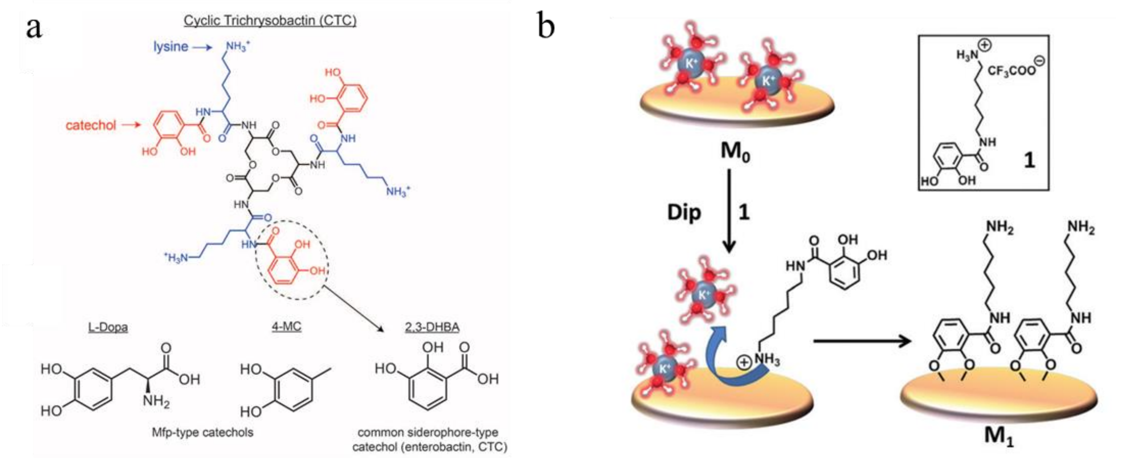

Figure 1.8. (a) Structure of cyclic trichrysobactin.[28] (b) Mechanism of mica modification through amine functional catechol.[29] Panel **a** reproduced from ref. 27, AAAS. Panel **b** reproduced from ref. 28, Wiley-VCH.

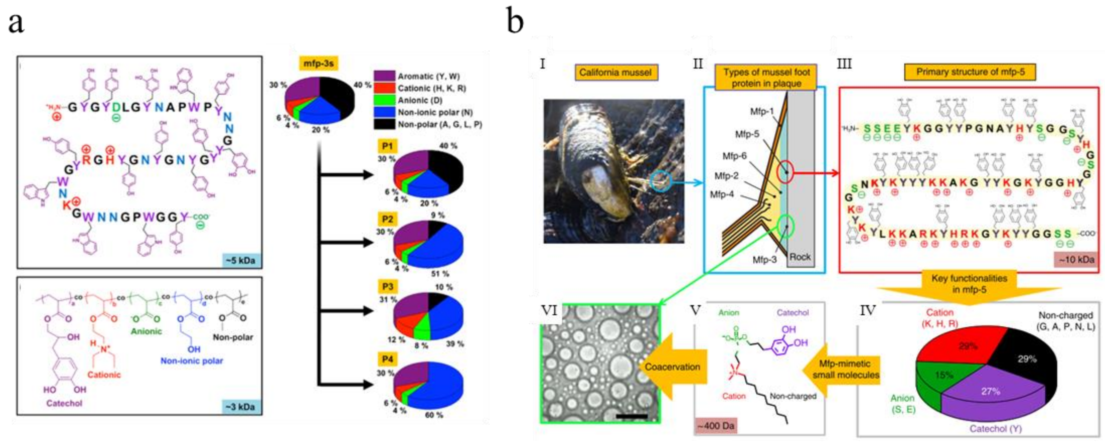

Figure 1.9. (a) Key amino acid in Mfp-3s and its synthetic analogue copolymer.[30] (b) charge of Mfp mimetic zwitterion catecholic molecule.[31] Panel **a** reproduced from ref. 29, American Chemical Society. Panel **b** reproduced from ref. 30, Nature Publishing Group.

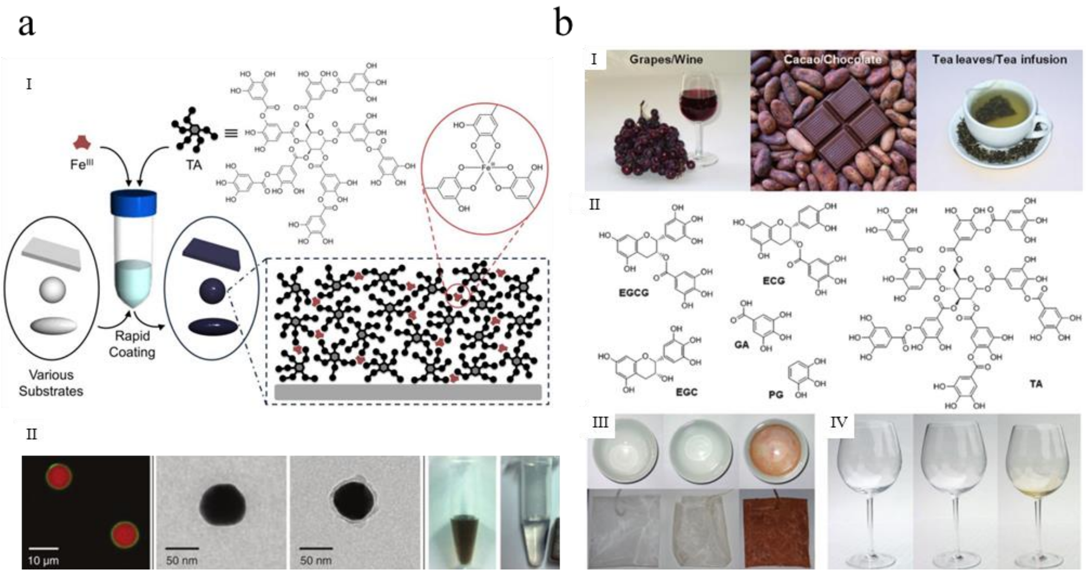

Figure 1.10. (a) I. Schematic illustration of the assembly of tannic acid and iron ion on a various substrates. II. Tannic acid assembly (green) on protein loaded $CaCO_3$ (red) particles.[32] (b) I. poly phenol rich grape, cacao, and green tea. II. Molecular structures of polyphenol derivatives from nature. III. Polyphenol coatings. IV. Colorless polyphenol coating on glass with red wine. $AgNO_3$ treatment for visualization of coating layer (right).[19] Panel **a** reproduced from ref. 31, AAAS. Panel **b** reproduced from ref. 19, Wiley-VCH.

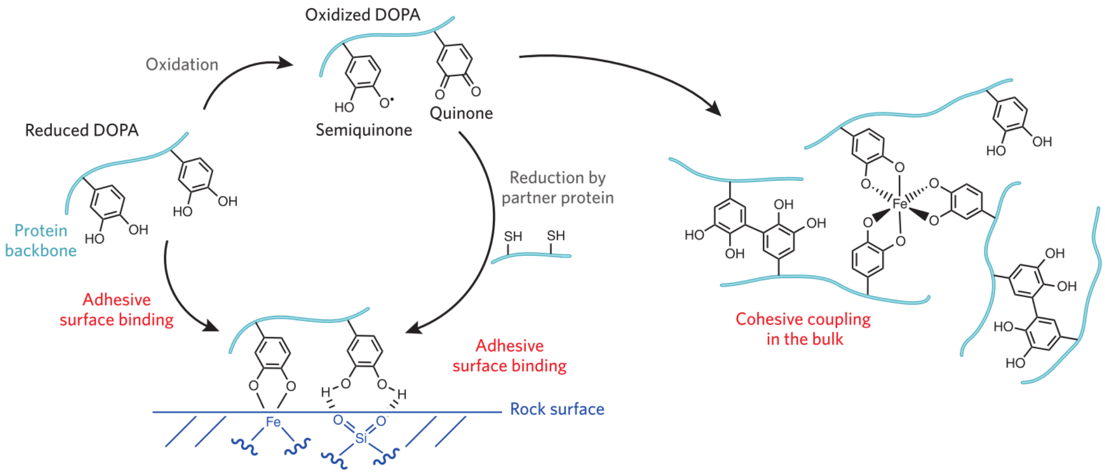

Figure 1.11. Mechanism of reduction by cysteine rich Mfp-6. The DOPA adsorb directly on rock surface and the oxidized DOPA are reduced by thiol of cysteine. The adhesion of DOPA is recovered and the cohesion of oxidized DOPA are suppressed.[27] Adapted from ref. 32 with permission from Nature Publishing Group.

1.4 References

1. Zherebetskyy, D.; Scheele, M.; Zhang, Y.; Bronstein, N.; Thompson, C.; Britt, D.; Salmeron, M.; Alivisatos, P.; Wang, L.-W., Hydroxylation of the surface of PbS nanocrystals passivated with oleic acid. *Science* **2014,** *344* (6190), 1380-1384.

2. Boles, M. A.; Ling, D.; Hyeon, T.; Talapin, D. V., The surface science of nanocrystals. *Nat Mater* **2016,** *15* (2), 141-153.

3. Dubertret, B.; Skourides, P.; Norris, D. J.; Noireaux, V.; Brivanlou, A. H.; Libchaber, A., In Vivo Imaging of Quantum Dots Encapsulated in Phospholipid Micelles. *Science* **2002,** *298* (5599), 1759-1762.

4. Osaki, F.; Kanamori, T.; Sando, S.; Sera, T.; Aoyama, Y., A Quantum Dot Conjugated Sugar Ball and Its Cellular Uptake. On the Size Effects of Endocytosis in the Subviral Region. *J. Am. Chem. Soc.* **2004,** *126* (21), 6520-6521.

5. Chen, Y.; Thakar, R.; Snee, P. T., Imparting Nanoparticle Function with Size-Controlled Amphiphilic Polymers. *J. Am. Chem. Soc.* **2008,** *130* (12), 3744-3745.

6. Liu, S.; Han, M.-Y., Silica-Coated Metal Nanoparticles. *Chemistry – An Asian Journal* **2010,** *5* (1), 36-45.

7. Graf, C.; Vossen, D. L. J.; Imhof, A.; van Blaaderen, A., A General Method To Coat Colloidal Particles with Silica. *Langmuir* **2003,** *19* (17), 6693-6700.

8. Ding, H. L.; Zhang, Y. X.; Wang, S.; Xu, J. M.; Xu, S. C.; Li, G. H., Fe3O4@SiO2 Core/Shell Nanoparticles: The Silica Coating Regulations with a Single Core for Different Core Sizes and Shell Thicknesses. *Chem. Mater.* **2012,** *24* (23), 4572-4580.

9. Banerjee, A.; Pons, T.; Lequeux, N.; Dubertret, B., Quantum dots-DNA bioconjugates: synthesis to applications. *Interface Focus* **2016,** *6* (6), 20160064.

10. Peng, E.; Wang, F.; Xue, J. M., Nanostructured magnetic nanocomposites as MRI contrast agents. *Journal of Materials Chemistry B* **2015,** *3* (11), 2241-2276.

11. Susumu, K.; Uyeda, H. T.; Medintz, I. L.; Pons, T.; Delehanty, J. B.; Mattoussi, H., Enhancing the Stability and Biological Functionalities of Quantum Dots via Compact Multifunctional Ligands. *J. Am. Chem. Soc.* **2007,** *129* (45), 13987-13996.

12. Liu, Y.; Chen, T.; Wu, C.; Qiu, L.; Hu, R.; Li, J.; Cansiz, S.; Zhang, L.; Cui, C.; Zhu, G.; You, M.; Zhang, T.; Tan, W., Facile Surface Functionalization of Hydrophobic Magnetic Nanoparticles. *J. Am. Chem. Soc.* **2014,** *136* (36), 12552-12555.

13. Jiang, H.; Chen, D.; Guo, D.; Wang, N.; Su, Y.; Jin, X.; Tong, G.; Zhu, X., Zwitterionic gold nanorods: low toxicity and high photothermal efficacy for cancer therapy. *Biomaterials Science*

2017, *5* (4), 686-697.

14. Ling, D.; Park, W.; Park, Y. I.; Lee, N.; Li, F.; Song, C.; Yang, S.-G.; Choi, S. H.; Na, K.; Hyeon, T., Multiple-Interaction Ligands Inspired by Mussel Adhesive Protein: Synthesis of Highly Stable and Biocompatible Nanoparticles. *Angew. Chem. Int. Ed.* **2011,** *50* (48), 11360-11365.

15. Liu, W.; Greytak, A. B.; Lee, J.; Wong, C. R.; Park, J.; Marshall, L. F.; Jiang, W.; Curtin, P. N.; Ting, A. Y.; Nocera, D. G.; Fukumura, D.; Jain, R. K.; Bawendi, M. G., Compact Biocompatible Quantum Dots via RAFT-Mediated Synthesis of Imidazole-Based Random Copolymer Ligand. *J. Am. Chem. Soc.* **2010,** *132* (2), 472-483.

16. Monnier, C. A.; DeMartini, D. G.; Waite, J. H., Intertidal exposure favors the soft-studded armor of adaptive mussel coatings. *Nature Communications* **2018,** *9* (1), 3424.

17. Wang, C. S.; Stewart, R. J., Multipart Copolyelectrolyte Adhesive of the Sandcastle Worm, Phragmatopoma californica (Fewkes): Catechol Oxidase Catalyzed Curing through Peptidyl-DOPA. *Biomacromolecules* **2013,** *14* (5), 1607-1617.

18. Zvarec, O.; Purushotham, S.; Masic, A.; Ramanujan, R. V.; Miserez, A., Catechol-Functionalized Chitosan/Iron Oxide Nanoparticle Composite Inspired by Mussel Thread Coating and Squid Beak Interfacial Chemistry. *Langmuir* **2013,** *29* (34), 10899-10906.

19. Sileika, T. S.; Barrett, D. G.; Zhang, R.; Lau, K. H. A.; Messersmith, P. B., Colorless Multifunctional Coatings Inspired by Polyphenols Found in Tea, Chocolate, and Wine. *Angew. Chem. Int. Ed.* **2013,** *52* (41), 10766-10770.

20. Lee, B. P.; Messersmith, P. B.; Israelachvili, J. N.; Waite, J. H., Mussel-Inspired Adhesives and Coatings. *Annual Review of Materials Research* **2011,** *41* (1), 99-132.

21. Yang, J.; Cohen Stuart, M. A.; Kamperman, M., Jack of all trades: versatile catechol crosslinking mechanisms. *Chem. Soc. Rev.* **2014,** *43* (24), 8271-8298.

22. Faure, E.; Falentin-Daudré, C.; Jérôme, C.; Lyskawa, J.; Fournier, D.; Woisel, P.; Detrembleur, C., Catechols as versatile platforms in polymer chemistry. *Prog. Polym. Sci.* **2013,** *38* (1), 236-270.

23. Li, Y.; Qin, M.; Li, Y.; Cao, Y.; Wang, W., Single Molecule Evidence for the Adaptive Binding of DOPA to Different Wet Surfaces. *Langmuir* **2014,** *30* (15), 4358-4366.

24. Lee, H.; Scherer, N. F.; Messersmith, P. B., Single-molecule mechanics of mussel adhesion. *Proceedings of the National Academy of Sciences* **2006,** *103* (35), 12999-13003.

25. Lee, H.; Dellatore, S. M.; Miller, W. M.; Messersmith, P. B., Mussel-Inspired Surface Chemistry for Multifunctional Coatings. *Science* **2007,** *318* (5849), 426-430.

26. Hong, S.; Wang, Y.; Park, S. Y.; Lee, H., Progressive fuzzy cation-π assembly of biological catecholamines. *Science Advances* **2018,** *4* (9), eaat7457.

27. Wilker, J. J., Biomaterials: Redox and adhesion on the rocks. *Nat Chem Biol* **2011,** *7* (9), 579-580.

28. Maier, G. P.; Rapp, M. V.; Waite, J. H.; Israelachvili, J. N.; Butler, A., Adaptive synergy

between catechol and lysine promotes wet adhesion by surface salt displacement. *Science* **2015,** *349* (6248), 628-632.

29. Sen, R.; Gahtory, D.; Carvalho, R. R.; Albada, B.; van Delft, F. L.; Zuilhof, H., Ultrathin Covalently Bound Organic Layers on Mica: Formation of Atomically Flat Biofunctionalizable Surfaces. *Angew. Chem. Int. Ed.* **2017,** *56* (15), 4130-4134.

30. Seo, S.; Das, S.; Zalicki, P. J.; Mirshafian, R.; Eisenbach, C. D.; Israelachvili, J. N.; Waite, J. H.; Ahn, B. K., Microphase Behavior and Enhanced Wet-Cohesion of Synthetic Copolyampholytes Inspired by a Mussel Foot Protein. *J. Am. Chem. Soc.* **2015,** *137* (29), 9214-9217.

31. Ahn, B. K.; Das, S.; Linstadt, R.; Kaufman, Y.; Martinez-Rodriguez, N. R.; Mirshafian, R.; Kesselman, E.; Talmon, Y.; Lipshutz, B. H.; Israelachvili, J. N.; Waite, J. H., High-performance mussel-inspired adhesives of reduced complexity. *Nat Commun* **2015,** *6*.

32. Ejima, H.; Richardson, J. J.; Liang, K.; Best, J. P.; van Koeverden, M. P.; Such, G. K.; Cui, J.; Caruso, F., One-Step Assembly of Coordination Complexes for Versatile Film and Particle Engineering. *Science* **2013,** *341* (6142), 154-157.

Chapter 2. Molecularly smooth and conformal nanocoating by amine-mediated redox modulation of catechol

2.1 Introduction

Catechol-based nanocoatings on nanostructured materials have gained interest in areas of molecular recognition, control of physicochemical properties during nanofabrication, and application of nanomaterials due to optimal experimental strategies at the molecular level.[1-4] Nanocoatings on substrates have been successfully fabricated through (a) controlled polymerization of dopamine and polyphenol derivatives, (b) coacervation of catecholic zwitterions, (c) salt replacement by catechol with flexible amino groups, and (d) coordination complexes of polyphenols and Fe^{3+} ions.[5-9] Although these film fabrication methods represent the state-of-the-art in the substrate nanocoating field, their application to nano-sized materials with high curvatures has been limited. Mussel-inspired nanocoatings on inorganic nanoparticles (NPs) have depended on dopamine and catechol derivatives; however, degradation and etching, heterogeneous coating layers, and agglomeration of NPs due to unstable and thick coating layers compared with original NP sizes have been reported as challenging issues.[10-13] Enhanced stability and decreased uncontrollable polymerization are urgent requirements for the formation of robust, monolayer, and smooth catechol-based coatings. Mussels use forces on multiple length scales, including cohesive and adhesive strength, to stick to rocks in the ocean.[14] Cohesive properties are related to the microscale connection of bulk, whereas adhesive force is concentrated on interface at nanometer scale level for adhesion. For nanocoatings, simultaneous suppressing cohesion and increasing adhesion is an ideal strategy to keep thin layer inert by blocking unnecessary growth of coating layer. DOPA and lysine in the Mfp-3 and -5 are well-known adhesion-related amino acids, and many studies have demonstrated highly adhesive synthetic materials by their imitation (Scheme 2.1a).[11,15,16] However, in-situ polymerization and intermolecular cross-linking due to the intrinsic oxidative properties of catechol induce cohesive properties and hinder the fabrication of precisely controlled coating layers.[17,18] We have focused on the restoration ability for oxidized catechol of Mfp-6 revealed by Yu et al.[19,20] Cysteine in Mfp-6 converts oxidized catechol to fresh catechol by coupling the oxidation of thiols to dopaquinone. We hypothesized that separated amine additives (AA) with catechol could function like Mfp-6 via addition reaction due to their nucleophilicity and thereby reduce cohesion and recover adhesion, even under oxidative conditions.

Herein, we report a conformal, molecularly smooth, and robust nanocoating by amine-involved modulation of the redox chemistry of catechol. The amine-assisted catechol nanocoatings (AACNs) on flat substrates and inorganic NPs were unprecedentedly uniform and ultrathin (Scheme 2.1b and

2.1c). The results demonstrate that suppressed cohesive properties, uniformity, and high stability can be achieved by the proposed coating system. The nanocoating layer was extensively analyzed by X-ray photoelectron spectroscopy (XPS), near edge X-ray absorption fine structure (NEXAFS), and high-resolution magic angle spinning (HR-MAS) nuclear magnetic resonance (NMR) spectroscopy to elucidate its molecular structure. We discovered that newly designed catechol-amine adducts were generated in-situ. A remarkable enhancement of the affinity to metal oxide surfaces of the compound was identified by density functional theory (DFT) calculations. We further elucidated three major roles of amine and suggested a mechanism for AACN.

2.2 Experimental section

2.2.1 Materials

Iron chloride hexahydrate, sodium oleate, sodium hydroxide, oleic acid, 4-*tert*-butylcatechol (TBC), dopamine hydrochloride, AEE, triethylamine (TEA), hexylamine, octylamine, dodecylamine, oleylamine, 6-amino-1-hexanol (AH), hexamethylenediamine (HMDA), poly(ethylene glycol) methyl ether acrylate, sodium periodate ($NaIO_4$), *N*-(3-dimethylaminopropyl)-*N′*-ethylcarbodiimide hydrochloride, *N*-hydroxysuccinimide, and 2-[2-(2-methoxyethoxy)ethoxy]acetic acid were purchased from Sigma Aldrich. Oligo ethylene glycol catechol (OEGC) was synthesized via a modified version of a previously reported method.[21] Dopamine methacrylamide and dibenzyl trithiocarbonate were synthesized as previously reported.[22,23] Organic solvents and AIBN were obtained from Junsei.

2.2.2 Instrumentation and analyses

^1H NMR spectra were recorded using a 400 MHz Agilent spectrometer, where the residual proton signal of the deuterated solvent was selected as the reference standard. HR-MAS proton spectra were recorded on an AV-700 NMR Spectrometer (Bruker, Rheinstetten, Germany) operating at 700.13 MHz, 6 KHz spinning rate, and 293 K with an HR-MAS probe. The sizes and morphologies of NPs were studied through transmission electron microscopy (TEM, JEOL, JEM-2100) conducted at 200 kV, for which the dispersed samples were placed on a carbon copper grid for measurement. Dynamic light scattering (DLS) measurements were performed on a Malvern Instruments Zetasizer Nano-ZS90 at 25 °C, and XPS spectra were recorded on an ESCALAB 250XI (Thermo Fisher Scientific). Al Kα radiation (1486.6 eV) under ultrahigh vacuum (1.0×10^{-10} torr) was used, and spectra were measured in high-resolution mode (0.45 eV). The samples were prepared using a freeze dryer before measurement. UV-Vis spectra were taken on a Shimadzu UV-1800 with a quartz cuvette, and infrared (IR) spectra were measured on a Varian 670/620 at room temperature. The surface morphologies of coating layers were analyzed by optical microscopy (OM, Eclipse LV150, Nikon) and atomic force microscopy (AFM, DI 3100, Veeco). All AFM images were obtained in tapping mode using silicon cantilevers (RTESP-300, Bruker).

2.2.3 Preparation of catechol-coated films

Prior to surface modification, the target substrates were rinsed sequentially by sonication for 15 min in distilled water, acetone, and isopropanol. Subsequently, the substrates were dried in an oven for 15 min at 120 °C. The catechol-coated films were formed by a simple dip-coating method under ambient conditions. For TBC and TBC-AEE films, TBC (87.25 mg, 0.52 mmol) was dissolved in pure methanol (10 ml). Then, AEE (1.05 ml, 10.50 mmol) was added to the solution only for TBC-AEE films. For TBC films, the pH of the coating solution was adjusted to 10 by addition of NaOH solution

(0.5 M) because AEE has basic properties as a primary amine. As a result, we evaluated the effect of the nucleophilic properties of AEE except for its basicity. The solution was mixed homogeneously by using a vertex mixer (VM-10, DAIHAN), after which its color changed from light pink to yellow. The rinsed substrates were immersed in the solution vertically and incubated for various times. After the coated films were carefully removed, physisorbed TBC and AEE were washed off by methanol and dried with Ar. We repeated this washing step three times and stored the samples in a desiccator for analysis. For diamine tests, these procedures were carried out in the same manner except that HMDA was used in place of AEE.

2.2.4 Polydopamine coating with AA

Polydopamine coating was performed following a slightly modified version of the method reported by Lee et al.[11] In a typical procedure, dopamine hydrochloride (20 mg, 0.11 mmol) was dissolved in 10 mM Tris buffer (10 ml, pH 8.5). Then, sapphire wafers were immersed vertically into the solution for 24 h. The formed polydopamine films were rinsed with distilled water and dried with Ar. To apply the AACN strategy, AEE (0.21 ml, 2.10 mmol) was added to the dopamine hydrochloride solution. The other procedures were carried out in the same manner except for the addition of AEE. It is worth noting that there were no precipitates in the coating solution with added AEE.

2.2.5 Synthesis of IONPs

IONPs were synthesized using the thermal decomposition of an iron oleate precursor in an organic solvent through a literature method.[24,25] In a typical synthesis of 11 nm sized IONPs, iron oleate (1 mmol) and oleic acid (0.7 mmol) were dissolved in 3 g of octadecene. The mixture was slowly heated to 320 °C, kept at this temperature for 30 min, and cooled under an inert atmosphere. The IONPs were washed twice with acetone and re-dispersed in hexane. The synthetic procedure of 3 nm sized IONPs was as follows. Iron oleate (1 mmol) and oleyl alcohol (6 mmol) were dissolved in 5 g of diphenyl ether. The mixture was heated to 250 °C at a heating rate of 3.3 °C/min under an Ar atmosphere and kept at that temperature for 30 min. The resulting solution was cooled under inert conditions, and the product was collected by centrifugation in acetone and ethanol for 3 min at 5000 rpm.

2.2.6 Polymerization of catechol-based PEG polymer

A catechol-based PEG polymer (CP) was prepared by a reported literature method.[26] Dopamine methacrylamide (0.06 mmol), PEG480 acrylate (0.24 mmol), RAFT agent (0.015 mmol), and AIBN (0.015 mmol) were mixed in a 5 ml vial. DMF (200 μl) was added to dissolve the reagents, and the resulting mixture was transferred to an ampule. The freeze-pump-thaw procedure was repeated three times, followed by sealing with a torch under vacuum and reacting in an oil bath at 70 °C for 12 h. After the reaction, the crude solution was precipitated with ethyl ether and washed three times.

2.2.7 Surface engineering of IONPs

The standard surface modification procedure is described as follows. The prepared OEGC (0.001 mmol) and AEE (0.1 mmol) were mixed in a tetrahydrofuran (THF) solution containing 2 mg of as-syn IONPs. The mixture was stirred at a temperature of 50 °C and reacted for 12 h. After the reaction, the solution was precipitated with the ethylether solvent, and the precipitated pellet was dissolved in MeOH for further use. For mechanism studies, CP was used for the surface engineering of IONPs. Oleic-acid-capped IONPs (2 mg) in 200 µl of THF were mixed with 0.001 mmol of CP and 0.1 mmol of AEE. The solution was reacted in a glass vial at 50 °C with magnetic stirring for 12 h. The crude solution was precipitated with ethylether to remove THF, and the pellet was dispersed in deionized water (D.W) and purified with a centrifugal membrane filter (Amicon Ultra-4 50 k devices).

2.2.8 Film thickness of catechol-coated films

Film thicknesses were measured by AFM and surface profiling (P6, KLA Tencor). For the AEE-added films, the vertical distance (height) between the top of the coated films and the uncovered vacancy was obtained by the NanoScope software from AFM images (1 × 1 μm^2). On the other hand, the step height of TBC-coated films was measured by the surface profiler. Because there were large aggregates with micrometer-scale heights on the TBC-coated surface, the surface profiler was more appropriate than AFM to measure their average thicknesses. All measurements were performed on at least five different areas for each sample.

2.2.9 NEXAFS analysis

Samples for NEXAFS experiments were prepared by dip-coating of catechol and AA onto sapphire substrates. To minimize the charging effect on the surfaces, we bridged the samples with conductive carbon tape. NEXAFS spectra were obtained at the Pohang Light Source II 4D beamline of the Pohang Accelerator Laboratory in Korea. A *P*-polarized synchrotron photon beam (polarization factor P=0.85) with an energy of 270-320 eV for the C K-edge was employed. The spectra were recorded at an incidence angle of 55° between the surface normal and light polarization (electric field vector). Partial electron yield (PEY) detection mode was used to analyze the surface of our nanometer-scale thin films to record the sample current to ground. This mode is more surface sensitive than total electron yield mode. The raw NEXAFS spectra were normalized to the beam current using a grid located upstream of the beamline. All data were obtained at room temperature under ultrahigh vacuum (~10^{-10} torr).

2.2.10 Contact angle measurement

To verify changes in surface properties, we prepared TBC-coated films with AEE, octylamine, dodecylamine, and oleylamine as the selected AAs. As described above in the general method, the coating solution was prepared by dissolving TBC (0.52 mmol) and AA (10.50 mmol) in 10 ml of methanol. After sample preparation, the contact angle of a water droplet was measured using a drop shape analyzer (DSA-100, Krüss). A 3 µl water drop was delivered onto the coated films using a microsyringe. All measurements were performed at five different points on each sample at room temperature.

2.2.11 Analysis of coating solution after AACN

A coating solution was obtained by purification of CP-coated IONPs after AACN with a centrifugal membrane filter. The filtrate dissolved in D.W was analyzed by UV-Vis spectroscopy in the range of 250-800 nm. The filtrate of CP-coated IONPs without AA was also measured, and oxidized CP was prepared for comparison by oxidation in 1× PBS under ambient conditions.

2.2.12 Colorimetric assay of Fe^{2+} elution

A portion of crude solution (10 μl) from AACN with IONPs was precipitated by 4 ml of ethyl ether. The pellet was dissolved in 3 ml of phenanthroline solution (2 mM), and the resulting solution was purified by centrifugal membrane filtration to remove IONPs. The filtrate was analyzed by UV-Vis spectroscopy.

2.2.13 Calculation details

DFT calculations were carried out using the Cambridge Serial Total Energy Package.[27] The Perdew–Burke–Ernzerhof version of the generalized gradient approximation[28,29] was used for exchange-correlation interactions, and norm-conserving pseudopotentials[30] were adopted to describe electron-ion potential. The Hubbard U parameter for Fe_{3d}, which was calculated by Santos-Carballal et al.,[31] was set as 3.7 eV for both Fe^{2+} and Fe^{3+} cations to localize *d*-Fe orbitals. To include van der Waals interactions between the Fe_3O_4 surface and adsorbates, the Tkatchenko–Scheffler method for DFT-D correction was also applied.[32] All calculations were performed with spin-polarized calculations and the energy cutoff of 900 eV. During optimization of the model system, Monkhorst–Pack grids[33] of $7 \times 7 \times 7$ *k*-points and $1 \times 2 \times 1$ *k*-points were applied to the primitive unit cell (i.e., rhombohedral Fe_6O_8) and surface systems, respectively.

The systems were modeled as follows. An inverse spinel structure of Fe_3O_4 was converted from an optimized rhombohedral primitive unit cell to construct a surface system as reported by Santos-Carballal et al.[31] (Figure 2.1a and 2.1b). This modeling scheme resulted in excellent agreement with experimental observations.[31,34] The optimized lattice parameter was 8.451 Å, which is within less than 1% error of the experimental value (8.390 Å).[35] The initial magnetic moments were introduced as a high-spin ferrimagnetic structure, where the tetrahedral sites were occupied by Fe^{3+} assigned with spin down and the octahedral sites were occupied by Fe^{2+} or Fe^{3+} assigned with spin up. The magnetic moments of tetrahedral Fe^{3+}, octahedral Fe^{2+}, and octahedral Fe^{3+} were calculated to be −4.190, 3.760, and 4.250 μ_B, respectively. A (001) surface slab model was constructed with a $(\sqrt{2} \times \sqrt{2})R45°$ unit cell consisting of 24 Fe atoms and 32 O atoms, which was extended to make a (1 × 2) supercell for assessing the adsorption of TBC and TBC-AEE (Figure 2.1c). Note that the (001) surface was chosen because it is the most stable facet.[31] In order to eliminate *z*-directional dipole effects on adsorption energy, a non-polar surface slab was constructed by removing tetrahedral Fe atoms (e.g., V_{Fe} shown in Figure 2.1c and 2.1d) from the top and bottom layers while maintaining the stoichiometry of the bulk state. During geometry optimization calculations, the lowest layer was fixed to impose bulk-like features. Finally, a vacuum height of 20 Å was introduced along the *z*-axis to avoid self-interaction of the surface slab model.

Energy calculations were conducted as follows. The adsorption energies (ΔE_{ads}) of adsorbates (i.e., TBC and TBC-AEE) were calculated as follows:

$$\Delta E_{ads} = E_{ads+\mathrm{Fe_3O_4}} - E_{ads} - E_{\mathrm{Fe_3O_4}}, \qquad (1)$$

where E_{ads} and $E_{\mathrm{Fe_3O_4}}$ represent the total energy of isolated adsorbate molecules and the Fe_3O_4 (001) surface, respectively, and $E_{ads+\mathrm{Fe_3O_4}}$is the total energy of the system that adsorbate molecules adsorbed on the Fe_3O_4 (001) surface. The relative surface slab energy (ΔE_{Surf}), which is referenced to the surface slab energy of the system with adsorbed TBC for each adsorption mode (i.e., TBC (or TBC-AEE) in bidentate chelating mode with tetrahedral Fe^{3+} and TBC (or TBC-AEE) in bidentate bridging mode with octahedral Fe^{2+} and Fe^{3+}), was calculated as follows:

$$\Delta E_{\mathrm{surf}} = E^{TBC-AEE}_{\mathrm{2H+Fe_3O_4}} - E^{TBC}_{\mathrm{2H+Fe_3O_4}}, \qquad (2)$$

where $E^{TBC-AEE}_{\mathrm{2H+Fe_3O_4}}$ and $E^{TBC}_{\mathrm{2H+Fe_3O_4}}$ represent the energy of the Fe_3O_4 (001) surface slab system with adsorbate molecules (TBC-AEE and TBC, respectively) and two dissociated hydrogen atoms. Note that the positive energy values indicate the unstable surface system due to the adsorption of TBC-AEE(C*x*) (i.e., *x* = 3, 5, 6, where C*x* indicates the carbon site AEE attached as shown in Figure 2.1e.

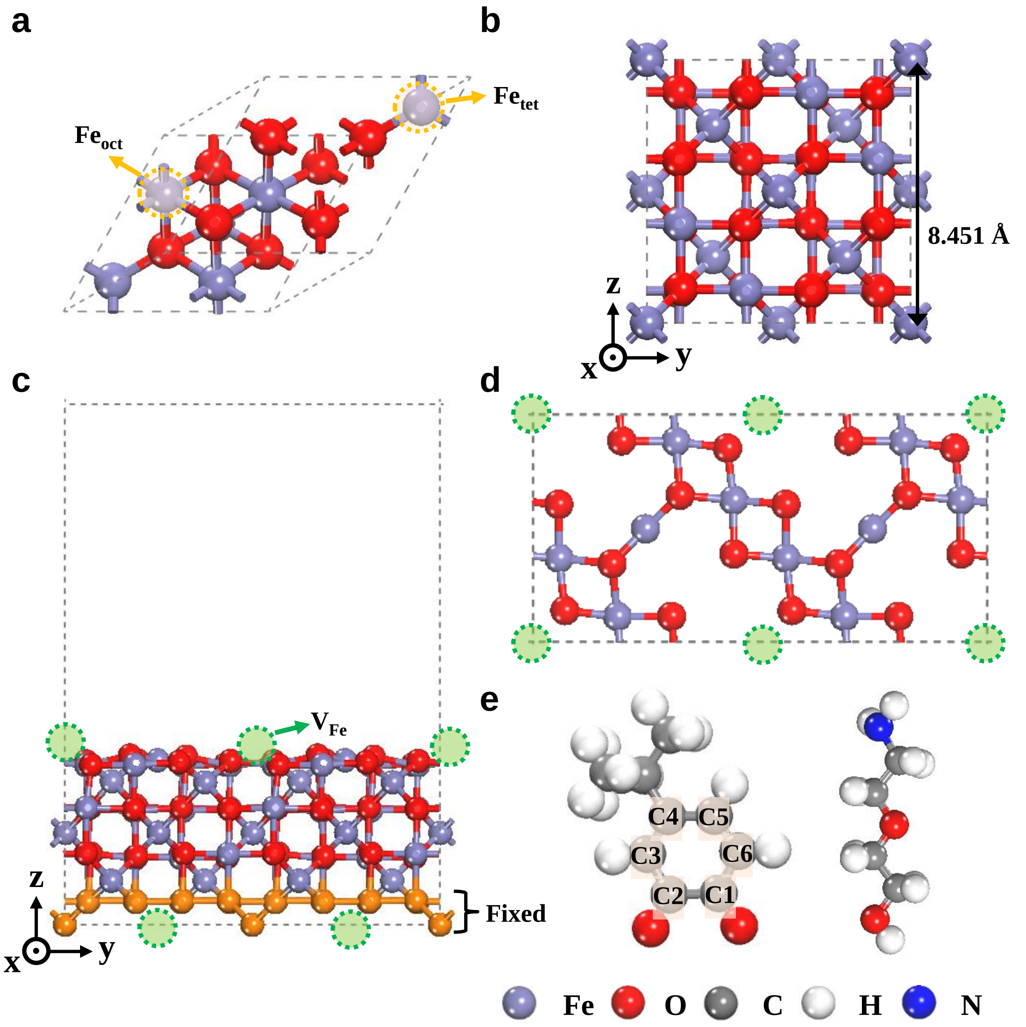

Figure 2.1. (a) Rhombohedral primitive unit cell of Fe_3O_4. (b) Inverse spinel structure of Fe_3O_4. (c) Side view of the slab model with (001) surface of Fe_3O_4, which is a (1 × 2) supercell extended from a $(\sqrt{2} \times \sqrt{2})\mathbf{R45°}$ unit cell. The fixed bottom layer in the slab model is colored orange, and V_{Fe} indicates the tetrahedral Fe^{3+} sites that were removed to eliminate the z-directional dipole effect of the surface. (d) Top view of (001) surface showing only the top layer. (e) Molecular structures of 4-*tert*-butylbenzo-1,2-quinone (left) and AEE molecule (right). Carbon atoms in the benzene group are numbered in the clockwise direction.

2.3 Result and discussion

2.3.1 Separation of lysine and DOPA

Mussels secrete Mfp-3,-5, and -6 primarily on the target surface to fix the byssus and other Mfps to support the main body. It is worth noting that adhesive strength is strongly related to Mfp-3, -5, and -6 optimized proteins for adhesion at nanoscale interfaces. Therefore, understanding the adhesion mechanisms of real mussels at interfaces is critical for the design of nanocoating adhesives. Insight into mechanisms for suppressing cohesion and increasing adhesion properties of catechol in real mussels under oxidation-vulnerable conditions was previously proposed.[20] The major mechanism is to eliminate oxidized catechol, which induces desorption of the coating layer and cohesive properties by polymerization with nearby dopaquinone. Cysteine in Mfp-6 converts oxidized catechol to fresh catechol by coupling the oxidation of thiols to dopaquinone. Amino molecules can also reduce quinone by creating covalent bonding with catechol. Lysine, which contains amino groups, is largely distributed in Mfp-3 and -5 at positions adjacent to DOPA. We hypothesized that lysine in Mfp-3 and -5 can interact in conjunction and function like cysteine in Mfp-6 to enhance adhesion and limit the oxidation of DOPA by modulating the redox chemistry. To realize our idea for nanocoating, we focused on DOPA and lysine and separated them to prevent cohesion from intermolecular cross-linking between molecules and self-polymerization through intramolecular ring closure, like dopamine. To reduce the chemical complexity of the biological model, we selected AEE in place of lysine and TBC in place of DOPA to mimic their moieties for a simple model experimental system.

2.3.2 Flat substrate coating

To demonstrate the hypothesis that separating AA with catechol groups prevents polymerization and forms a smooth nanocoating, we prepared thin films by simple dip-coating of the substrate in a mixture of TBC and AEE or only TBC (Figure 2.2a). Sapphire wafer was selected as a target substrate because its components are similar to that of mica surfaces, and the smoothness of the surface is helpful for elaborating nanoscale film analysis by AFM.

First, we investigated the surface morphologies of the prepared films by OM and AFM to observe the cohesion suppressive effect of AA addition to the TBC coating layer. The TBC-coated film without AEE had a very coarse and rough surface with a high root mean square (RMS) value of 4.78 ± 4.37 nm (Figure 2.2b). The thickness of the TBC film was not controllable, and it accumulated progressively with increasing immersion time (Figure 2.3). On increasing the immersion time from 1 to 24 h, the average thickness of the TBC films increased from 103 nm to 6.22 µm (Figure 2.2d). The thicknesses of TBC-coated films were measured using a surface profiler because the surfaces were too rough to measure by AFM. This surface roughness arises from catechol oxidative chemistry and remains a challenging problem associated with catechol-based surface chemistry. Catechol is prone to oxidation, and oxidized catechol induces chaotic intermolecular crosslinking and aggregation.[36] Van der Waals forces and π-π interactions are also major factors in uncontrollable surfaces.[5] In contrast, when AEE was added to the TBC solution, an ultrasmooth thin film was formed with a thickness of 1.69 nm and an RMS of 0.358 ± 0.09 nm (Figure 2.2c). Surprisingly, the thickness of the AEE-added films remained under 1.70 nm as coating time increased, and there was no sign of agglomeration (Figure 2.2d). Although nanocoating was achieved by controlling the coating time for polyphenol derivatives and modulating chemical structure in previously reported mussel-inspired coating methods,[5,8,9,11,37-41] our system can form ultrasmooth monolayers simply by separation of amine and catechol. In fact, other groups have also studied the effect of non-covalently linked catechol and amine, but they focused on the adhesion force with lab-shear tests and wet adhesion force measurements.[42,43] However, these previous results did not demonstrate suppressed cohesion properties via reaction between separated amine and catechol, which is a significant hypothesis for ultrasmooth nanocoating.

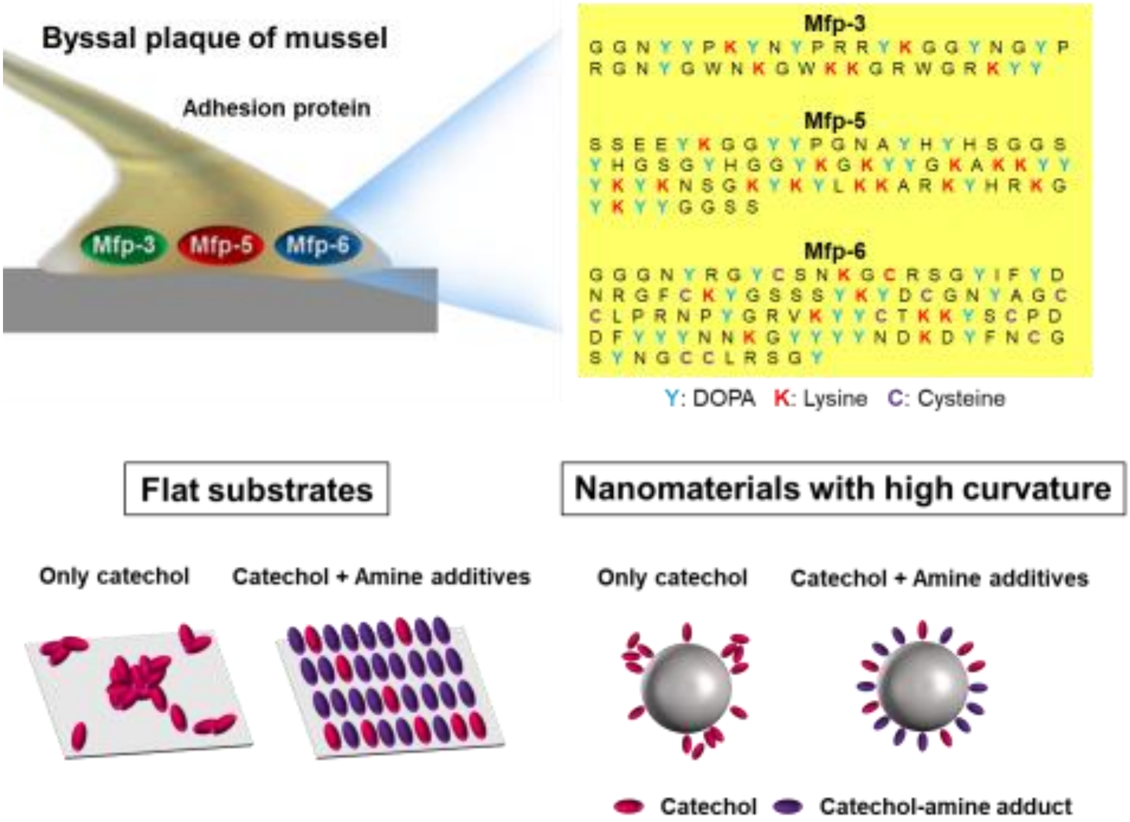

Scheme 2.1. Schematic illustrations of (a) mussel byssal plaque and a catechol-based coating and AACN on flat (a) substrates and (c) nanomaterials with high curvature.

To investigate the role of AA, we performed X-ray surface analyses including XPS and NEXAFS. XPS analysis was carried out to characterize the chemical environments of the coated thin films. The C 1s XPS spectra of the TBC and AEE-added films were deconvoluted to peaks at 284.5, 286.0, and 287.9 eV representing C-C/C-H, C-N/C-O, and C=O bonds, respectively.[38,44,45] For the AEE-added film, the peak intensity at 286 eV increased compared with TBC films (Figure 2.2e and 2.2f). The N 1s spectra also showed a peak at 399.7 eV, indicating a C-N bond (Figure 2.4). These results implied the generation of catechol-amine adducts on AEE-coated films because of the newly formed C-N bond in the secondary amine and the C-O bond of AEE.[38] Furthermore, C K-edge NEXAFS spectra were obtained to analyze the electronic structure and orientation of the catechol molecules on the coated surfaces (Figure 2.2g). We used PEY detection mode for NEXAFS spectra to acquire surface-sensitive signals with a probing depth of approximately a few nanometers.[46] As shown in Fig 1g, the intensity of the peaks at 284.9, 288.5, and 293 eV increased in the AEE-added film. Because the peaks at 284.9 and 288.5 eV are associated with the π* C=C and π* C=O orbitals of TBC, their increased intensities indicated that the degree of arrangement among catechol molecules was improved. In contrast, their arrangement in the TBC film was relatively random.[46,47] The increased signal at 293 eV suggested the generation of C-N/C-O bonds,[48] which corresponded to the XPS data. The in situ generated catechol-amine adduct reveals that AA participates in an addition reaction with oxidized catechol. These results support that the addition reaction step is a key point in the fabrication of nanocoatings through suppression of uncontrollable polymerization.

To demonstrate the versatility of our strategy, we modified the type of AA (R_n, n=1-4) with different alkyl chain lengths and terminal groups, including AEE (R_1), octylamine (R_2), dodecylamine (R_3), and oleylamine (R_4) (Figure 2.5). When the AA amine group was incorporated into the TBC molecule on the sapphire substrate, the other terminal part of the AA changed the surface properties. The effect was investigated by water contact angle measurements. The hydroxyl group of AEE yielded a more hydrophilic film with a contact angle of 39.8±0.6°, whereas that of the unmodified sapphire substrate was 48.3±1.7°. With longer AA alkyl chain lengths with a methyl group, the water contact angle gradually increased up to 75.6±1.4°. Thus, the AACN method can change surfaces and yield versatile properties via appropriate selection of the AA. This facile control of surfaces was proven to be a versatile platform for diverse functional uses. To confirm the Michael reaction during AACN, we studied the diamine system using HMDA as an example of AA, which could act as a cross-linker in the AACN system because of its primary amine groups on both end sites. AFM analysis was performed to observe the thickness and roughness of films dependent on the ratio of HMDA to AEE. As expected, the coated films became thicker and rougher as the amount of HMDA increased (Figure 2.6). This result supports that amine groups covalently bonded to catechol by the Michael reaction.

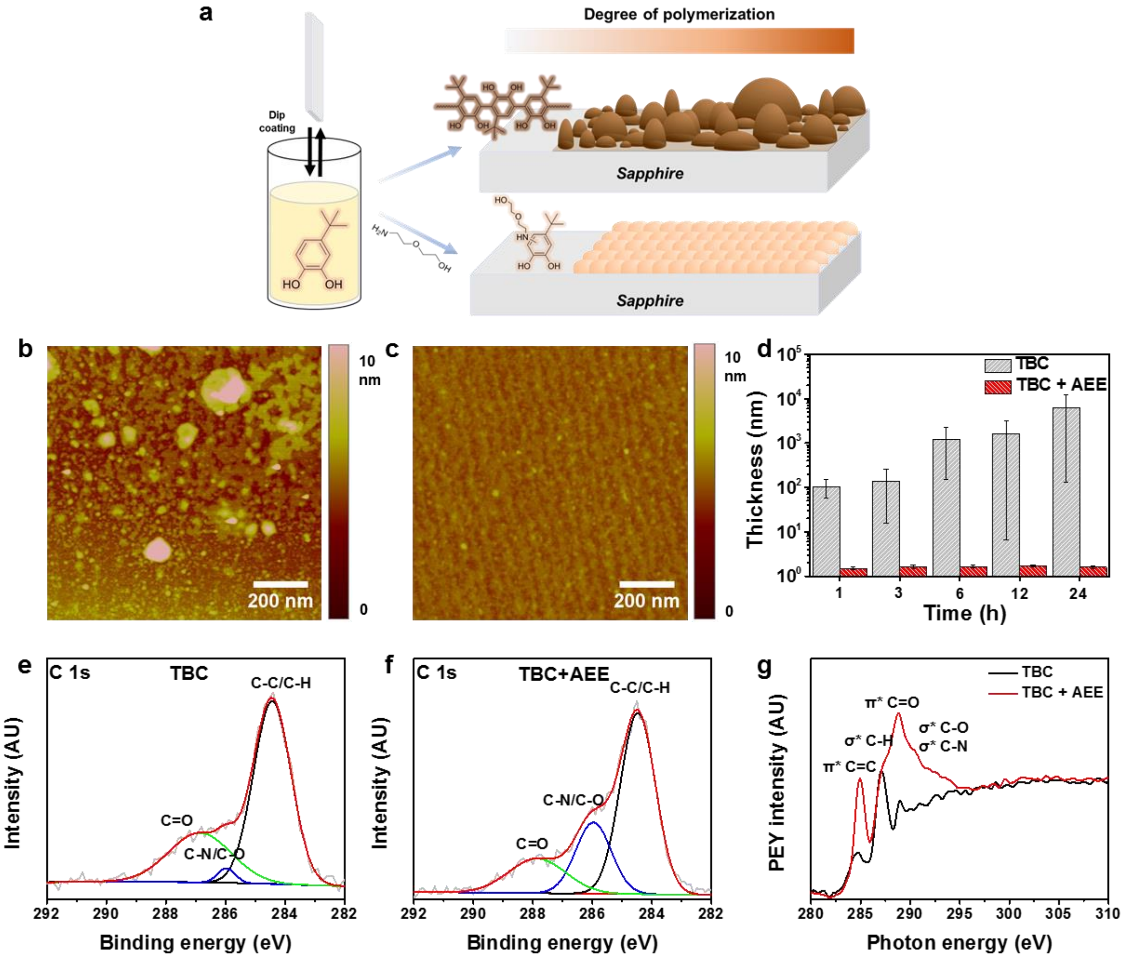

Figure 2.2. (a) Schematic illustration of catechol coating on metal oxide surface with only TBC (above) and with addition of AEE (below). (b) AFM images of TBC-only coating (TBC 0.5 mmol/ml, pH 10) and (c) mixture of TBC and AEE coating (TBC 0.5 mmol/ml, TBC:AEE = 1:20) after 24 h of coating. (b) Thicknesses of TBC and TBC-AEE films versus time. The TBC film was analyzed by alpha-step, and the TBC-AEE film was measured by AFM. XPS C 1s spectra of (e) TBC-only on sapphire and (f) TBC-AEE. (g) Carbon K-edge X-ray absorption fine structure spectra of TBC (black) and TBC-AEE (red) coated on sapphire wafers. The data were collected in PEY mode with an incident angle of the linearly polarized X-ray beam of 55°.

The application of the AACN method can be expanded substantially with diverse chemical structures that contain catechol derivatives. For example, AACN can be applied to polydopamine, one of the most famous catecholamines noted for its excellent adhesion and cohesion properties.[11] When AA was added during polydopamine coating, agglomerates disappeared and a uniform, transparent thin coating was made possible (Figure 2.7). This phenomenon originated from dopamine-AEE adducts preventing the formation of 5,6-dihydroxyindole polymerizable intermediates.

Although we have exhibited that the AACN approach is a versatile platform for functionalization of flat substrates, nanocoating on highly curved nanostructures should also be studied in depth. The surface engineering of nanomaterials by AACN has great potential to sustain the NP properties through passivation of individual NPs with thin-layer coatings.[49] Their dispersion in solvents is controlled, and surface functionalization ability is provided by the nanocoating layer. For example, surface modification is essential for applying inorganic NPs to bioapplications. Biocompatibility, biological targeting, and biodistribution are directly determined by the NP interface.[50] A compact hydrodynamic diameter (HD) is also a significant factor for short clearance time and targeting ability.[51] Therefore, nanocoating techniques can widen the potential of inorganic NPs for various applications and contribute to the field of nanoscience.

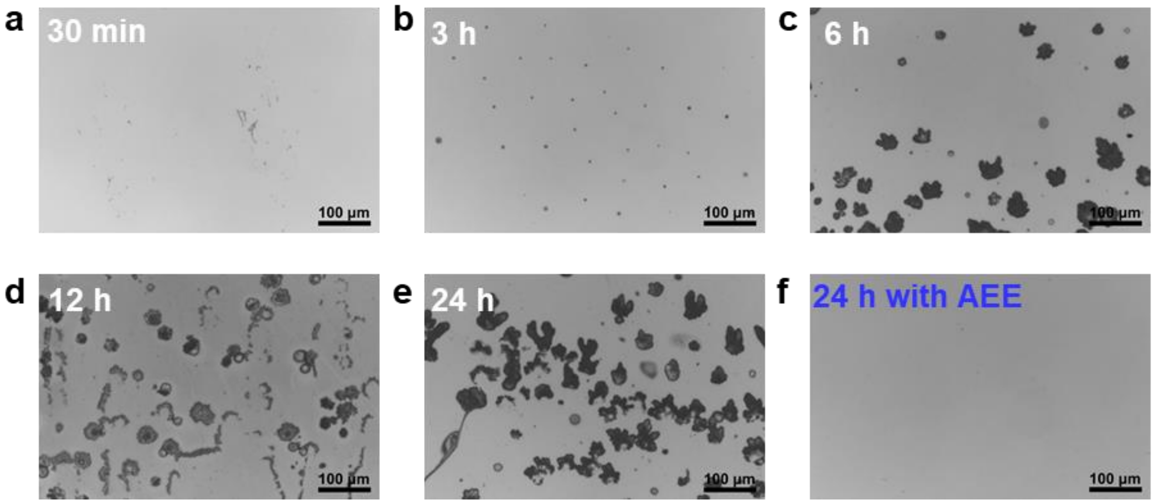

Figure 2.3. Optical microscopy images for different coating incubation times. TBC coating on sapphire wafer without AEE (pH 10) for (a) 30 min, (b) 3 h, (c) 6 h, (d) 12 h, and (e) 24 h and with AEE for (f) 24 h.

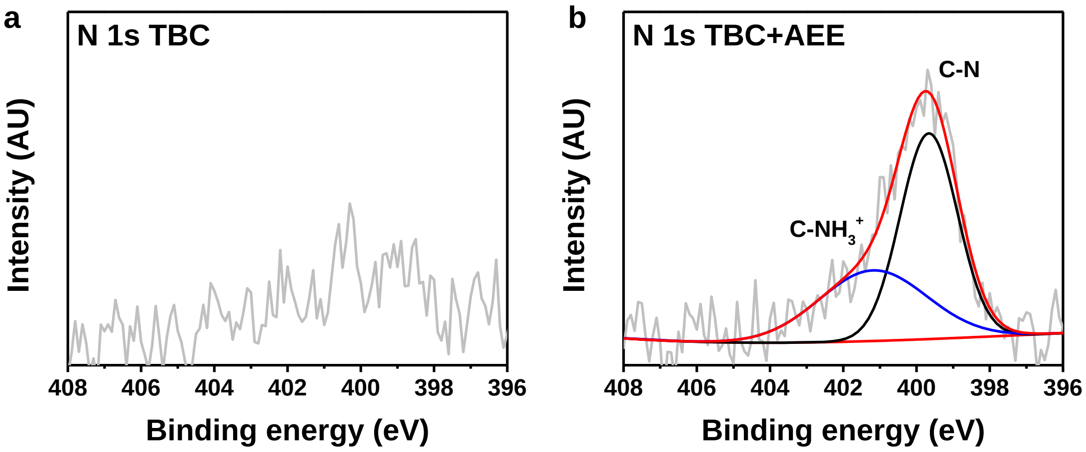

Figure 2.4. XPS N 1s spectra of (a) TBC-only and (b) TBC with AEE on sapphire wafers.

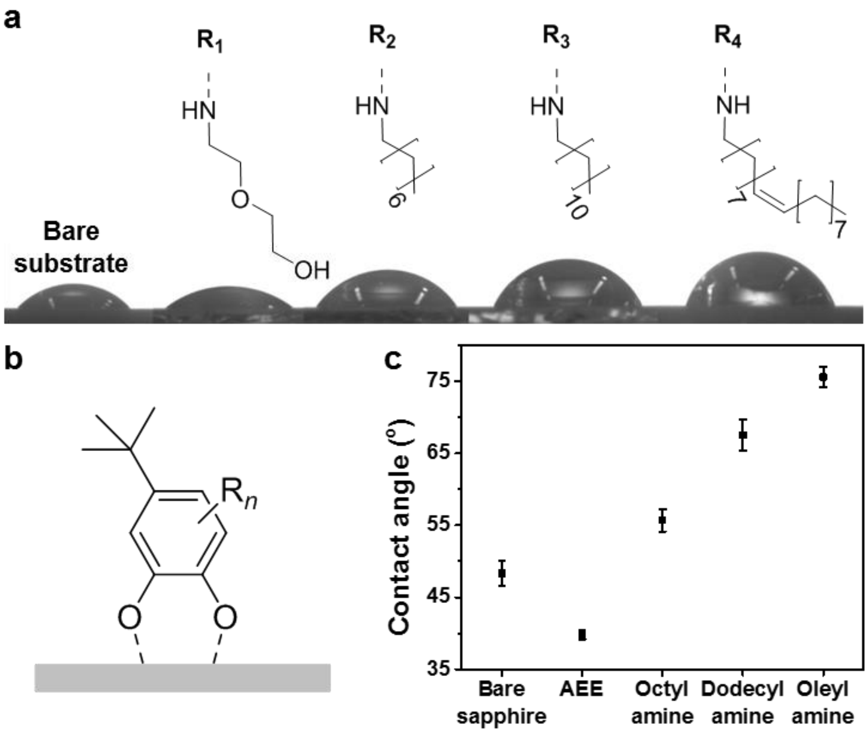

Figure 2.5. (a) Differences in contact angle in the presence of various types of AA (AEE, octylamine, dodecylamine, and oleylamine). (b) Schematic of sapphire substrate modified by TBC and AA. (c) Static water contact angles of TBC coatings on sapphire wafer according to the type of AA.

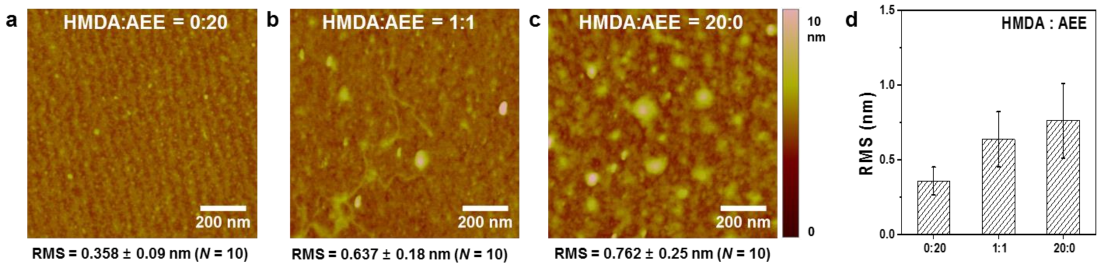

Figure 2.6. Effects of diamine as AA. AFM images of TBC-coated film on sapphire wafer (1 × 1 μm^2) with molar ratios of AEE to HMDA of (a) 20:0, (b) 1:1, and (c) 0:20. (d) Average RMS values of the TBC-coated films (*N*=10).

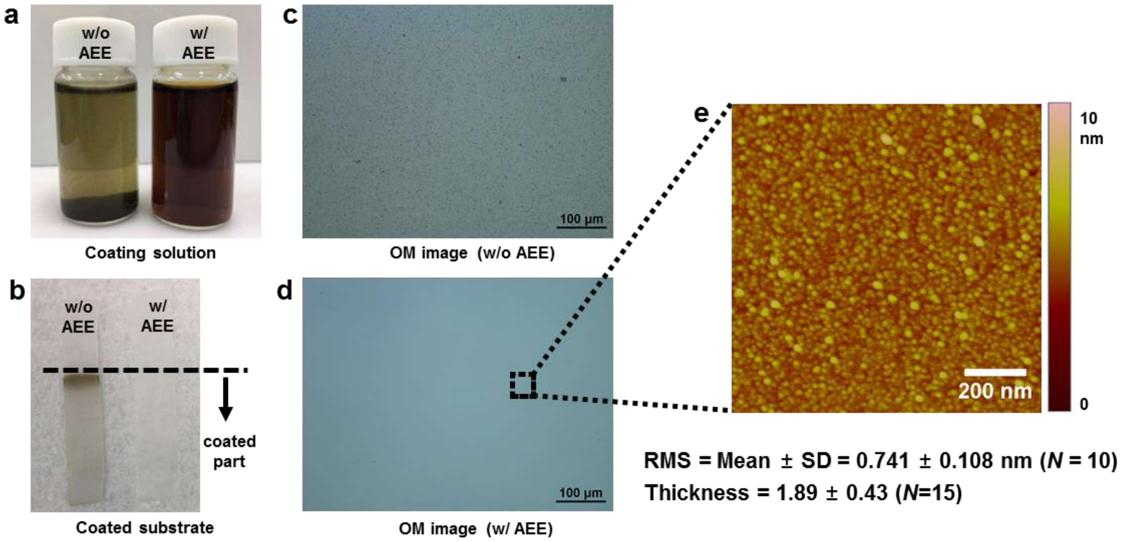

Figure 2.7. AACN applied to polydopamine (PDA) coating (2 mg/ml in Tris buffer, pH 8.5). (a) Photograph of PDA coating solutions depending on the presence of AEE after 24 h of incubation. (b) Photograph of washed PDA-coated sapphire wafer. One is dark brown (without AEE) and the other is colorless (with AEE). (c, d) OM images of PDA-coated substrates depending on the presence of AEE. (e) Morphology, roughness, and thickness of PDA-coated film with AEE on a sapphire wafer determined by AFM.

2.3.3 Nanomaterial coating

The IONP is a representative nanomaterial that has the unique nanosized effect of superparamagnetic properties. To confirm the feasibility of AACN for coating IONPs, we used OEGC instead of TBC because the *tert*-butyl group of TBC is insufficient for dispersing IONPs in solvents. AEE was also changed to AH to avoid interference with OEGC in ^{1}H NMR analyses (Figure 2.8a). We have already demonstrated the general applicability of various kinds of AAs and catechol derivatives as AACN reagents. THF was used as a coating solvent because oleic-acid-capped IONPs and other reagents are homogenously soluble in THF.

As shown in Figure 2.8b, OEGC-coated IONPs precipitated in MeOH, and significant aggregation occurred. The hydrodynamic sizes of OEGC-coated IONPs were several hundred nanometers due to incomplete coating of the OEGC (Figure 2.8d). In contrast, the OEGC and AH coating solution successfully transferred IONPs to the methanol phase. The DLS data in Figure 2.8d determined an HD of OEGC-coated IONPs with AH of 8 nm with no sign of aggregation. This dramatically enhanced stability of IONPs by addition of AA is an extraordinary result.

To investigate the organic coating layer of both types of coated IONPs, ^{1}H HR-MAS NMR was performed. Conventional NMR analysis of IONP surfaces is challenging because of the large broadening effect from paramagnetic disturbance and decreased mobility of the ligands on the surface.[52] In contrast, HR-MAS NMR is a powerful and effective analytical technique because the paramagnetic effects and chemical shift anisotropy can be decreased.[52,53]

Figure 2.8e, f, and g show the normal NMR spectra of AH, OEGC, and mixture of AH and OEGC with oxidant ($NaIO_4$), respectively. It is well known that catechol reacts with nucleophilic additives under oxidative conditions, and thus OEGC and AH with $NaIO_4$ were measured as references to compare changes in the aromatic structure patterns with coating layer on IONPs.[54] Above the spectra are references for comparison with coating layers of IONPs. Figure 2.8h, i, and j are ^{1}H HR-MAS NMR spectra of OEGC/AH-coated IONPs, OEGC-coated IONPs, and oleic-acid-capped IONPs, respectively. The NMR data were analyzed by separation into three areas denoted as (I), (II), and (III). (I) is the area between approximately 3.3 and 4.2 ppm and is optimal for observing $-CH_2$ of OEG signals from OEGC. (II) is an enlargement of the area between 1.0 and 2.4 ppm for detecting the alkyl groups of AH and oleic acid. (III) is between 5.4 and 7.2 ppm and focuses on the proton of the aromatic group of OEGC and its derivatives to provide information on reactions between OEGC and AH, like Michael addition. Area (I) in Figure 2.8h shows a signal between 3.5 and 3.7 ppm, indicating that OEGC and AH exist in the coating layer of IONPs (yellow box). In Figure 2.8i, only the OEGC signal appeared for the OEGC-coated IONPs. Peaks appeared at 1.2~1.8 ppm for AH, which were assigned to the $–CH_2-$ of the alkyl group. In Figure 2.8h, an AH signal was detected in area (II), meaning that AH and OEGC co-existed in the nanocoating layer of IONPs@OEGC/AH (gray box).

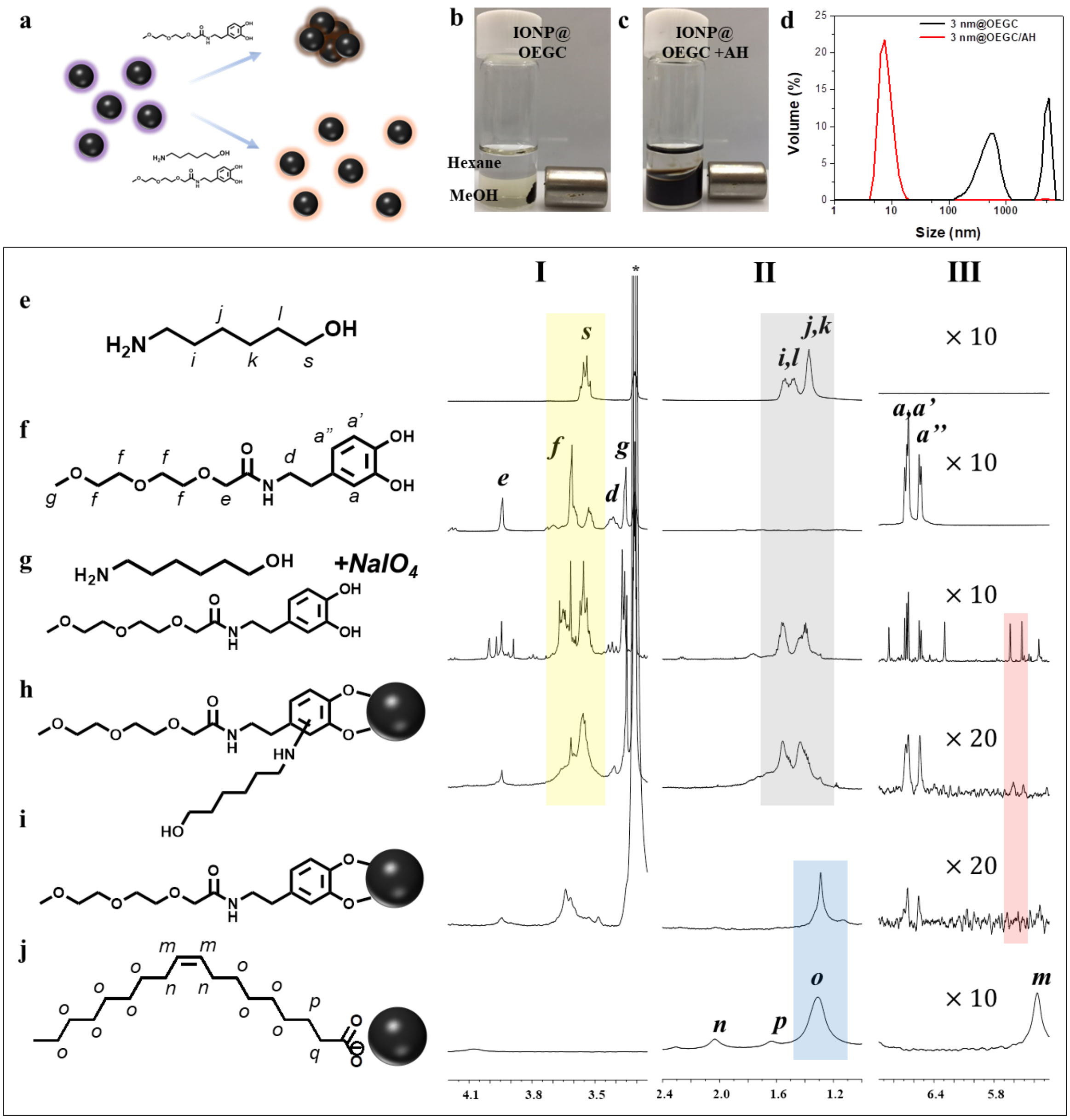

Figure 2.8. (a) Schematic illustration of catechol coating on metal oxide NPs. Photograph of (b) aggregated IONPs after coating with only OEGC and (c) dispersed IONPs in MeOH after AACN with OEGC. (d) DLS data of AACN IONPs with OEGC and OEGC-only coated IONPs, ^{1}H NMR spectra of (e) AH, (f) OEGC, and (g) OEGC and AH mixture with oxidant ($NaIO_4$). ^{1}H HR-MAS NMR spectra of (h) OEGC and AH-coated IONPs, (i) OEGC-coated IONPs, and (j) oleic-acid-coated IONPs at 6 kHz MAS rate.

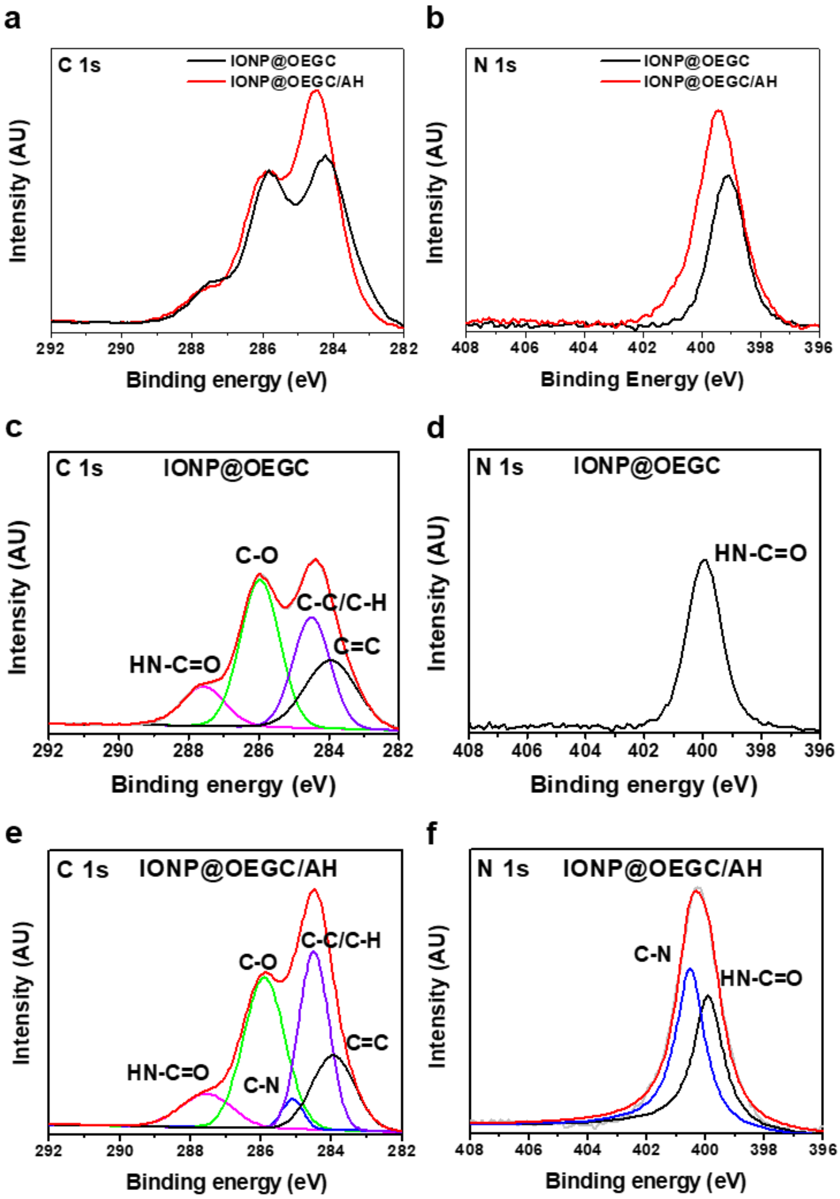

Figure 2.9. Combined XPS (a) C 1s and (b) N 1s spectra of IONP@OEGC with AH and IONP@OEGC. Deconvolutions of (c, e) C 1s XPS spectra and (d, f) N 1s XPS spectra of IONP@OEGC/AH and IONP@OEGC.

On the other hand, oleic acid (1.2~1.4 ppm) remained on IONPs in the case of OEGC-only coating (blue box). The results indicate that the affinity of OEGC is not enough to replace oleic acid on the IONP surfaces under these experimental conditions and that desorption of OEGC by surface catalyzed oxidation is also possible.[10]

Proton signals from 6.53 to 6.66 ppm in area (III) indicate the aromatic structure of OEGC and were detected in the spectra shown in Figure 2.8f, 2.8g, 2.8h, and 2.8i. When Michael addition was induced, new signals at 5.3~5.7 ppm, near 6.29 and 6.84 ppm, and at 6.53~6.66 ppm developed, as shown in Figure 2.8g. These newly developed peaks suggested a change in the substitution pattern of the aromatic part of OEGC. Interestingly, OEGC/AH-coated IONPs showed new signals at approximately 5.63 and 5.52 ppm, and similar proton peaks were also detected in the spectrum shown in Figure 2.8g (red box). All of above the signals suggested the existence of catechol-amine adducts on the surface of IONP@OEGC/AH.

XPS spectra was analyzed to confirm the chemical environments of the IONP coating layers. As shown in Figure 2.9a, the C 1s spectrum of IONP@OEGC/AH has a larger and positive-shifted photopeak at approximately 284 eV compared with IONP@OEGC. Similarly, the N 1s spectrum of IONP@OEGC/AH also exhibited a larger and positive-shifted signal compared with IONP@OEGC (Figure 2.9b). Each C 1s spectrum was deconvoluted, and Figure 2.9c shows the C 1s XPS spectrum of OEGC-coated IONPs and the corresponding deconvoluted peaks at 287.6, 286.0,

284.5, and 284.0 eV. As shown in Figure 2.9e, the C 1s XPS spectrum of IONP@OEGC/AH was deconvoluted into 287.5, 285.1, 285.9, 284.5, and 283.9 eV peaks. These peaks represent HN-C=O, C-O, C-N, C-C/C-H, and C=C, respectively.[55] Since IONP@OEGC/AH and IONP@OEGC have the amide group of OEGC in common, a comparison analysis was performed by normalization based on the C 1s peak of -NH-C=O (287.5 eV). Interestingly, AH addition during the coating process with OEGC gave rise to a C-N signal (285.1 eV), and the content of C-C/C-H bonds increased to 31.2% from 27.3% compared with the OEGC-only coating layer because of the alkyl chain of AH. These results indicate that AH was included in the nanocoating in the form of OEGC-AH adducts. Furthermore, a structural change in the amine group was observed in the N 1s XPS spectra (Figure 2.9d and 2.9f). The signal of IONP@OEGC/AH (Figure 2.9f) is wider and downshifted compared with IONP@OEGC, as shown in Figure 2.9d. The spectrum in Figure 2.9f was deconvoluted to 400.5 and 399.9 eV, which indicate C-N and HN-C=O, respectively. The newly developed 400.5 eV photopeak indicates that a secondary amine was generated in situ during film fabrication since the signal at 399.9 eV is attributed to the amide group of OEGC (Figure 2.9d).[56] According to the above data, it was confirmed that AA participates in the formation of the nanocoating. It seems that the in situ generated catechol-amine adduct plays an important role in maximizing the adhesion force by direct reaction of amine with catechol during coating. These results from IONPs are well consistent with the data obtained from flat substrates.

2.3.4 Coating mechanism

The mechanism of AACN was explored by using macromolecules, a catechol-based PEG polymer (CP), as a model system. The water-soluble properties of the polymer facilitate the purification of excess ligand after the coating reaction through a centrifugal membrane filter. Wide application possibilities were also considered due to the high stability and biocompatibility of the PEG group. Multidentate polymer-based ligands are more stable than mono-anchor ligands, and therefore PEG-based polymers

with multiple anchor groups were synthesized in our previous work (Figure 2.10a).[26,57] XPS and FT-IR were used to analyze AACN on IONPs with CP (Figure 2.11 and Figure 2.12). To investigate the role of AA, stability tests with various base additives were carried out to demonstrate that the adhesion force was induced by the basicity of AA. Released iron ions and ligand states after AACN were analyzed by UV-Vis spectroscopy to demonstrate the interaction of the catechol and IONP surfaces.

IONPs with a size of 12 nm were coated with CP under four different conditions: THF with no additives and addition of water, TEA, and AEE to elucidate which is the main factor between strong basicity and nucleophilicity of AA for nanocoating (Figure 2.10b). Oleic-acid-capped 12 nm IONPs were coated with CP in dry THF and exhibited micrometer sizes by DLS due to the low adhesive force of CP (Figure 2.10b). Addition of 5% (v/v%) water during coating increased the colloidal stability dramatically compared with the dry THF solution (Figure 2.10b), and a monomodal size distribution of 33 nm was observed. Water can act as a weak proton acceptor from the dihydroxyl group of catechol, thereby facilitating metal coordination of the deprotonated catechol.[58,59] However, the coating thickness of 11.5 nm was still large

compared with the theoretical PEG length of CP (~3 nm).[60] The large HD value is caused by IONP-catalyzed oxidation of catechol. Shultz et al.[10] reported dopamine-mediated degradation of IONPs and suggested that Fe^{3+} accelerates the oxidation of dopamine. The lower stability of Fe^{3+}-rich Fe_2O_3 NPs than Fe_3O_4 supports the idea that the surface state of the substrate significantly influences the quality of the coating

layer because of electron transfer between catechol and iron ions (Figure 2.13).[61,62] The oxidation potential of catechol and reduction potential of Fe^{3+} are similar.[36] Thus, to minimize the surface-catalyzed oxidation of catechol, TEA as a stronger base than water was used as an additive because the catechol-Fe^{3+} complex prevents the oxidation of catechol at a high pH.[62] In experiments using TEA, the HD value was 34 nm, similar to the case of water as an additive (Figure 2.10b). The effect

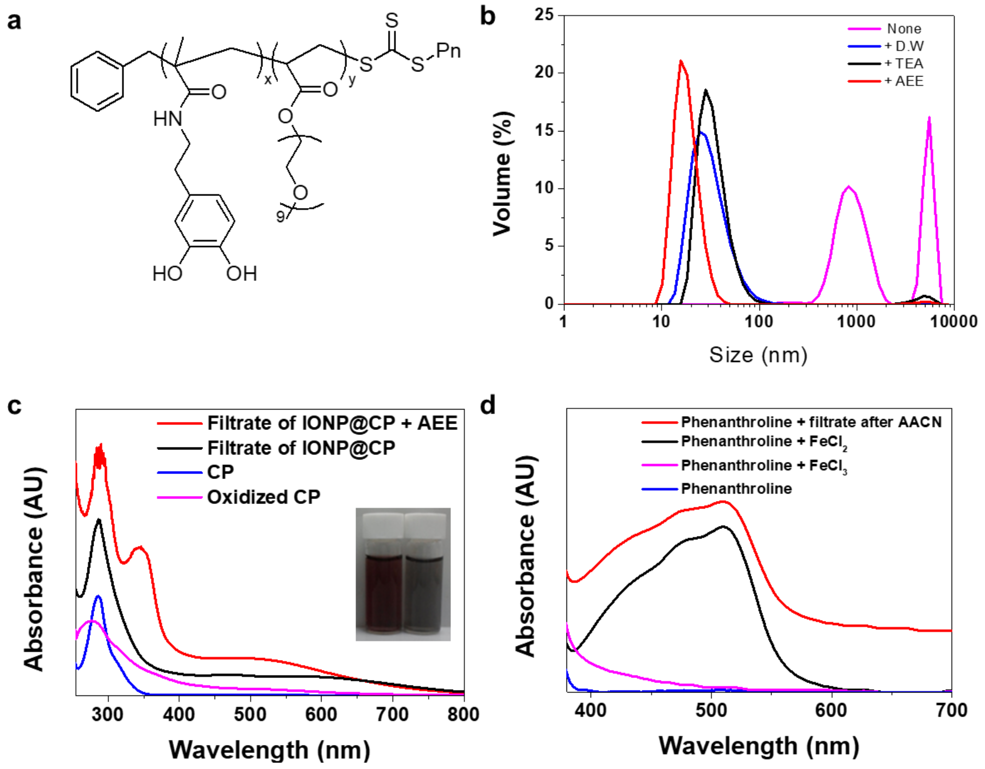

Figure 2.10. (a) Molecular structure of CP. (b) DLS data of CP-coated 12 nm Fe_3O_4 NPs in dry THF, THF+D.W, THF+TEA, and THF+AEE. (c) UV-Vis spectra of CP, oxidized CP, and filtrates of IONP@CP and IONP@CP + AEE with a photograph of filtrates after AACN on IONPs. (d) UV-Vis spectra for detection of Fe^{2+} dissolved from IONPs. The absorbance peak near 550 nm indicates that Fe^{2+} ions exist in the solution.

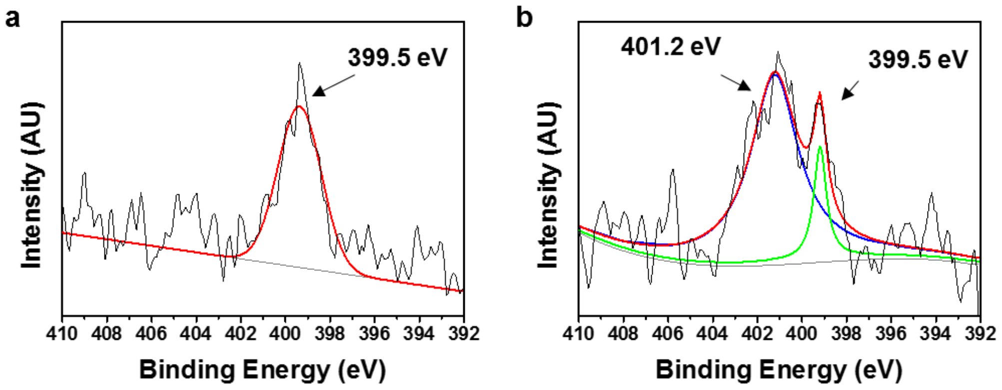

Figure 2.11. XPS N 1s spectra of (a) IONP@CP and (b) IONP@CP with AEE. The peak at 399.5 eV in (a) is the N 1s of the amide bond of DMA from CP. In the case of coating with AEE in (b), a new peak occurs at 401.2 eV along with the amide bond signal, which means that secondary amines exist on the surface of IONPs.

of TEA was remarkable in the Fe^{3+}-rich Fe_2O_3 NPs (Figure 2.13b). Although aggregates of 59 nm were observed, HD became small (16 nm) and less agglomeration occurred compared with water as an additive for Fe_2O_3 NPs (Figure 2.13b). Based on this result, basicity is an important factor for adhesion to NPs during the coating process. However, a basic environment alone cannot prevent cohesion of catechol, and a nonuniform coating layer formed on the NPs. Surprisingly, AEE addition yielded compact HD values of 21 and 18 nm and narrow size distributions on both γ-Fe_2O_3 and Fe_3O_4 NPs (Figure 2.10b and Figure 2.13b), respectively. The thicknesses of the shells are 4.5 nm and 3.5 nm, respectively, and which are close to monolayer coatings. This result is notable because oxidized IONPs could not be nanocoated even with nitro-catechol, which is known as a more stable anchor than catechol and has been reported to be decomposed by dopamine.[10,59] Only AA can produce a monolayer through the reduction of oxidized catechol; this is the second role of amine in our coating system. This result is contrary to the work of Rapp et al., which showed that separated catechol and amine do not have a synergistic effect on adhesion to mica.[43] Furthermore, in general, a high pH causes detrimental effects to adhesion because of the oxidation of catechol.[63] We ascribe our conflicting results to the different substrate (iron oxide) and basic pH conditions of our experiment. Yu et al. also reported the enhanced adhesion of Mfp-3 to TiO_2 surfaces at a high pH due to a coordination bonding mode despite the increased oxidation of DOPA.[64]

After AACN on IONPs, excess CP ligand was separated using a membrane filter, and the separated ligand was characterized by UV/VIS to analyze the state of its oxidation and metal-ion complexes (Figure 2.10c). The purple filtrate after AACN on IONPs had different absorbance spectra from CP, oxidized CP, and filtrate of the CP-only coating (Figure 2.10c). A prominent point is the new peak at 343 nm, which has been reported in previous studies of amine-catechol adducts generated by the reaction of amine and catechol.[65,66] Additionally, a large UV absorbance shoulder was detected at an Abs_{max} of 537 nm, indicating that catechol exists in the form of tris catechol and iron ion complexes.[9,67] This suggests that the basic environment by AA is critical for strong adhesion of catechol to IONPs because the tris catechol-iron complex has the highest stability constant among metal-ligand chelates ($\log K_s \cong 40$).[68] A phenanthroline photometric method for the determination of Fe^{2+} was conducted to prove that oxidation of catechol occurs at the same time as reduction of Fe^{3+} to Fe^{2+} (Figure 2.10d).[62] The phenanthroline solution changes its color to deep red in the presence of Fe^{2+} but does not change with Fe^{3+}. A strong absorbance at ~550 nm developed in the reaction mixture of phenanthroline and filtrate after AACN, which was equal to that of a mixture of phenanthroline and $FeCl_2$. This demonstrates that Fe^{2+} dissolved into solution during AACN of IONPs and supports the above conclusion that interactions exist between catechol and IONPs.

The stabilization effect of catechol-amine adducts is also a potential role of amine in the overall adhesive performance. To prove this assumption, we conducted DFT simulations of AACN on an iron oxide substrate with TBC and AEE as a model system.

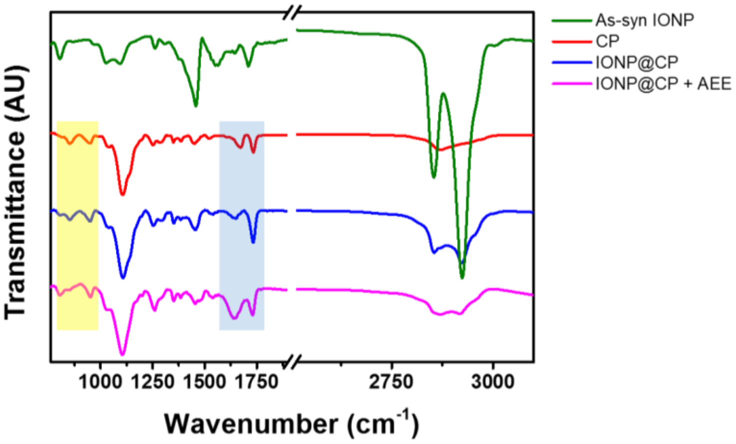

Figure 2.12. FT-IR spectra of as-syn IONPs, CP, IONP@CP, and IONP@CP with AEE. Surfaces of IONPs after coating were also analyzed by FT-IR. The 1670 cm^{-1} peak of the catechol aromatic group shifted to 1644 cm^{-1} due to binding with iron ions after IONP coating. The intensity of the peak did not decrease compared with the peak at 1730 cm^{-1}, which is an indicator of amide and ester bonds. This means that the catechol group maintained its 1,2-dihydroxy benzene structure and was not in an oxidized form. The 948 and 852 cm^{-1} peaks of CP are derived from the CH out of plane deformation peaks of 1,2,4-trisubstituted benzene. After coating with AEE, the peak at 852 cm^{-1} compared with that at 948 cm^{-1} largely decreased compared with IONP@CP, indicating a change in the substituent pattern of the aromatic ring.

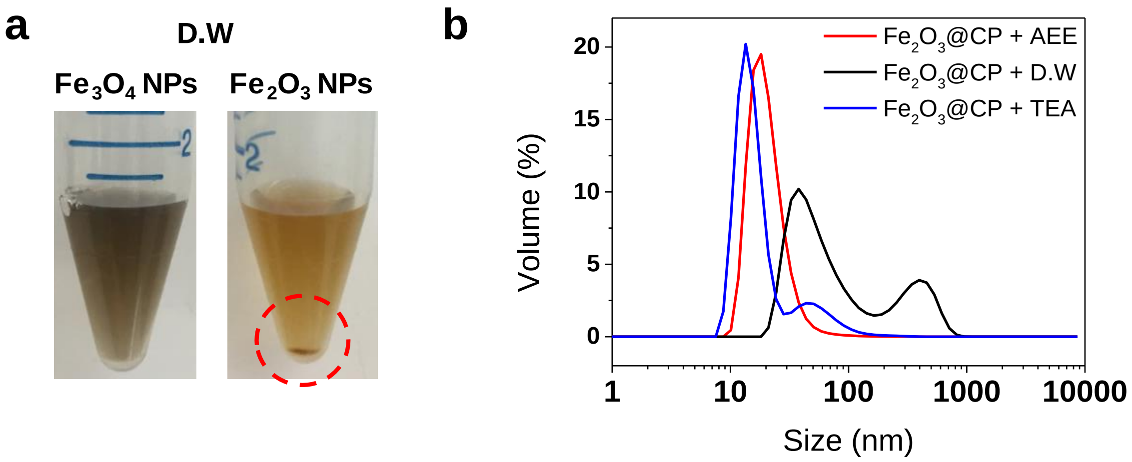

Figure 2.13. (a) Photographs of CP-coated 12 nm Fe_3O_4 and Fe_2O_3 NPs in THF with water additives. Aggregation was detected only in Fe_2O_3 NP samples. (b) DLS data of CP coated on Fe_2O_3 NPs in THF with water, TEA, and AEE additives.

2.3.5 Calculations

DFT calculations were carried out to elucidate the reaction of quinone and AEE and the adsorption tendency of catechol-amine adducts. The primary amine in AEE can be adsorbed on the carbon ring of the quinone, which is known to form catechol by reducing quinone.[36,69,70] Since catechol is more adsorptive than quinone, the reduction of quinone is considered important for surface coating. In order to determine the preferred carbon site for AEE adsorption, the primary amine was attached to the C3, C5, or C6 carbon site of quinone (Figure 2.14a and Figure 2.1e). It was found that AEE preferred to bind on C6 rather than on C3 or C5 since the binding of AEE near the *tert*-butyl group induced a relatively large destabilization of the molecule (Step 2 in Figure 2.15a). After the amine group of AEE attached to C3, C5, or C6, a hydrogen atom from the amine group is detached, and moves toward the solution side. Subsequently, O1 or O2 of the quinone was reduced (Figure 2.15b).[71] As shown in the reaction mechanism graph (see Step 3 in Figure 2.15a), the first oxygen to be reduced was O2 for C3 and C5 and O1 for C6. Next, the remaining unreduced oxygen in the quinone was reduced after the hydrogen on the AEE-bound carbon detached (see inset in Figure 2.15b).[72] As both oxygen atoms were reduced, the quinone eventually adopted the TBC-AEE form. The stability of the TBC-AEE forms decreased in the order of AEE attached to C6, C5, and C3 (see Step 4 in Figure 2.15a). Finally, the C6-O1 reaction path, with the lowest energy barrier (Step 2) and most stable energy (Step 4), was found to be the most favorable. Based on this reaction procedure, it is expected that quinone could regain its reactivity to Fe_3O_4 by adopting the catechol form.

The adsorption tendency of TBC on iron oxide was also investigated to compare the adsorption energy of the TBC-AEE(C*x*) adduct on iron oxide. To be as thorough as possible, we considered both octahedral and tetrahedral iron sites. Additionally, two adsorption modes that were estimated to be the most probable were studied: TBC (or TBC-AEE) in bidentate chelating mode with tetrahedral Fe^{3+} and TBC (or TBC-AEE) in bidentate bridging mode with octahedral Fe^{2+} and Fe^{3+} (Figure 2.14a and Figure 2.16). As shown in Figure 2.14b, the average adsorption affinity of TBC-AEE(C*x*) was greater than that of the TBC molecule alone, and TBC-AEE(C6) showed the strongest adsorption. It was noteworthy that the TBC-AEE(C6) was most likely to form in the reaction of AEE and quinone (Figure 2.15a). We found that the attachment of AEE on TBC always improved the adsorption, except for TBC-AEE(C3) on tetrahedral Fe^{3+}, where the surface was strongly destabilized by the adsorbate molecule. This was demonstrated by its high relative surface slab energy (ΔE_{Surf}, see Calculation details for the definition) of +2.24 eV compared with those of other systems, which were in the range of −1.01 ~ +1.3 eV. Considering that the occurrence of TBC-AEE(C3) on tetrahedral Fe^{3+} is the least probable (i.e., one out of nine cases), AEE can be treated as an adsorption promoter for the TBC coating of Fe_3O_4 because of its desirable roles in reducing quinone and improving adsorption affinity. From the DFT calculations, we confirmed the enhanced stabilization effect by in situ formed catechol-

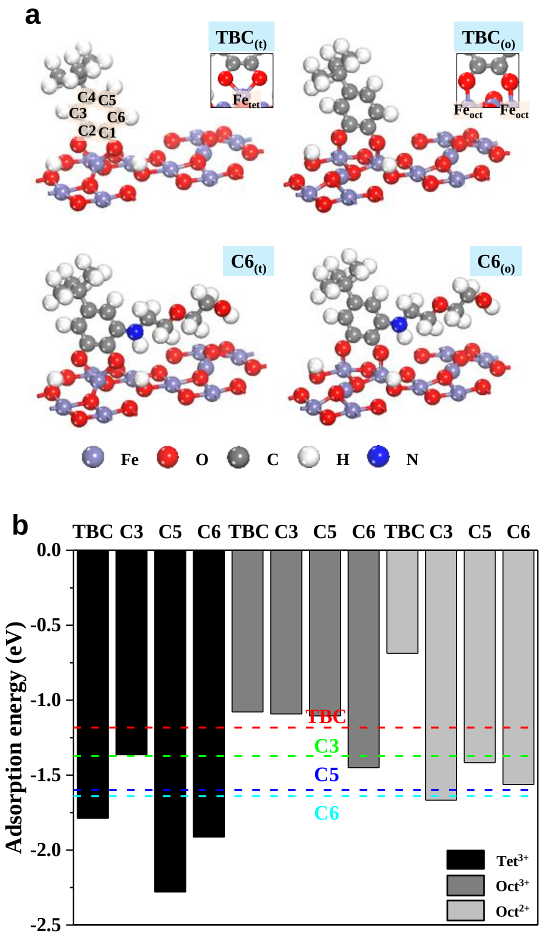

Figure 2.14. (a) Adsorption forms of TBC and TBC-AEE on a tetrahedral Fe^{3+} site in bidentate chelating mode (left) and on octahedral Fe^{2+} and Fe^{3+} sites in bidentate bridging mode (right), where only the top of surface layer is shown. The insets indicate each adsorption mode, and subscripts (t) and (o) indicate tetrahedral Fe^{3+} and octahedral Fe^{2+} and Fe^{3+} TBC adsorption sites, respectively. (b) Adsorption energies of TBC and TBC-AEE on Fe_3O_4 (001) surface. The terms ‘C3,’ ‘C5,’ and ‘C6’ denote TBC-AEE(C*x*) molecules on the Fe_3O_4 (001) surface where the AEE molecule is bound at C3, C5, and C6 sites, respectively. The colored dashed lines in the graph indicate average adsorption energies of TBC and TBC-AEE(C*x*) molecules.

amine adducts. The charge transfer between iron and catechol was also studied by DFT calculations. When a catechol-amine adduct was bound to the iron ion, the iron was supplied an additional electron compared with TBC (Table 1). This result suggests that the catechol-amine adduct provides stable bonding with iron ions by the electron donating effects of the amine substituent to iron ions. The transfer of additional electrons between catechol-amine adducts and iron ions is limited by the changed redox potential of the catechol-amine adduct. Furthermore, partially reduced Fe^{3+} cannot easily obtain an additional electron from catechol.[73]

As a result of investigating AACN versus basicity, substrate control, and DFT calculations, three roles of AA can be summarized following Scheme 2. The first role of AA is an increase in the basicity of the solution, which facilitates the coordination of catechol to the metal oxide surface. The second role is a suppression of cohesion and recovery of adhesion of catechol by the reduction of oxidized catechol. Catechol on the surface is oxidized and reacts with AA through an addition reaction, which prevents detachment of ligands from the surface and polymerization of the coating layer. After generation of a catechol-amine adduct, the amine substituent supplies electrons to the aromatic ring and substrates and enhances the binding affinity of the chemicals to substrates. Additionally, this phenomenon is speculated to endow catechol with resistance to oxidation by changing the redox potential between it and iron ions. Additional steric hindrance from the amine substituent protects binding sites from access by attacking molecules.

We propose an AACN mechanism according to the data presented above. Initially, catechol binds strongly to both Fe^{2+} and Fe^{3+} on the surface due to high pH conditions. Electron transfer from catechol to Fe^{3+} occurs, and Fe^{3+} is simultaneously reduced to Fe^{2+}. The generated semiquinone moves to an adjacent iron ion, and the reduced Fe^{2+} is eluted from the surface to the solution. When there are no additives, the oxidation of catechol occurs sequentially, and finally catechol detaches from the surface in the form of a quinone (Figure 2.17a).[10] With AA addition, the semiquinone is recovered through Michael addition of AA (Figure 2.17b, i). The additional oxidation of semiquinone is prevented and it instead binds with an Fe^{3+} ion. A different route can also be suggested. The quinone recovers its adhesion affinity by the formation of a catechol-amine adduct and binds again to an iron ion (Figure 2.17b, ii). In a multidentate catechol-based polymer, some catechol anchor binds well with the surface, and the others can be fully oxidized. The oxidized catechol can remain near the surface and have enough time to react with AA.

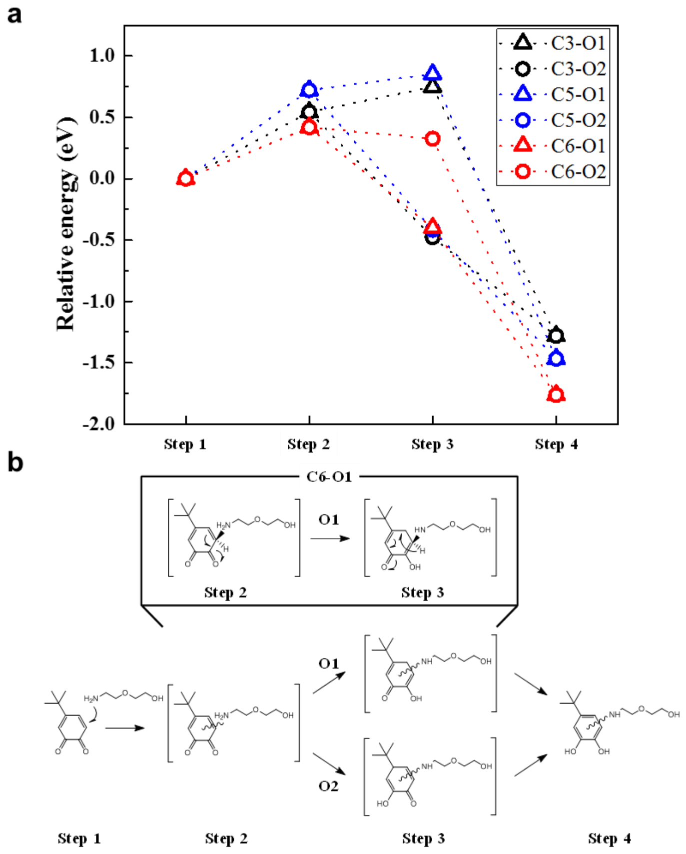

Figure 2.15. (a) Relative energy profiles referenced to the total energy of Step 1. Step 1 to Step 4 indicate the reaction process for the reduction of quinone to TBC with the aid of AEE. Note that C*x*-O*y* (i.e., *x* = 3, 5, 6, *y* = 1, 2) indicates the reaction path where AEE is bound on the C*x* site and O*y* is preferentially reduced. (b) Schematic representation of the reaction procedure. O1 and O2 represent the preferentially reduced oxygen sites in the reaction. Inset shows the detailed reduction procedure of oxygen atoms in the case of C6-O1.

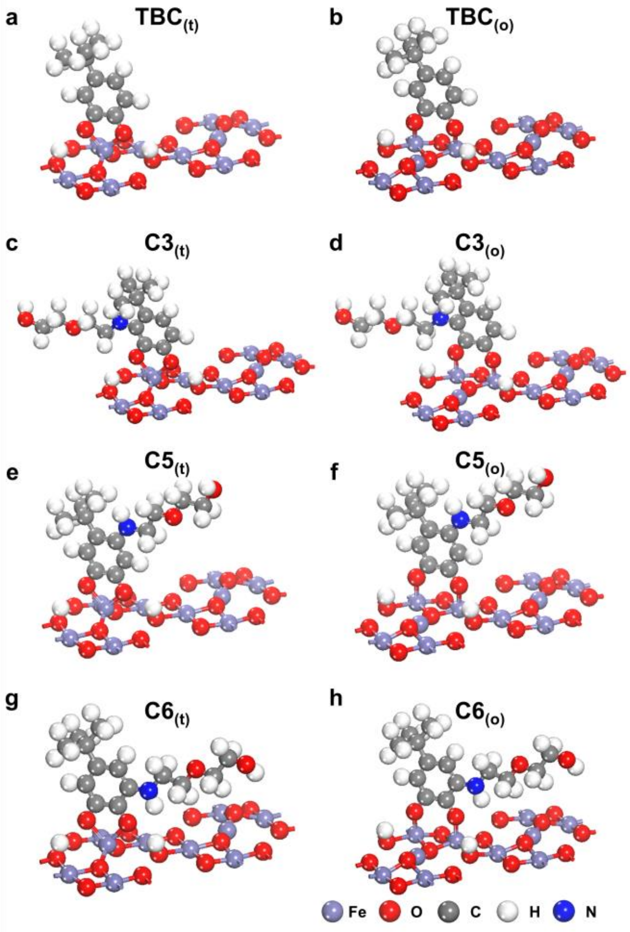

Figure 2.16. Adsorbed forms of TBC and TBC-AEE on (a, c, e, g) a tetrahedral Fe^{3+} site in bidentate chelating mode and on (b, d, f, h) octahedral Fe^{2+} and Fe^{3+} sites in bidentate bridging mode. 'C3,' 'C5,' and 'C6' denote TBC-AEE molecules on the Fe_3O_4 (001) surface where the AEE molecule is bound at the C3, C5, and C6 site, respectively. Subscripts (t) and (o) indicate tetrahedral Fe^{3+} and octahedral Fe^{2+} and Fe^{3+} adsorption sites for TBC, respectively.

Table 1. Charge transfer from catechol derivatives to iron ions.

Charge transfer [*e*]	-	Oct Fe^{2+}	Oct Fe^{3+}	Tet Fe^{3+}
TBC	-	0.110	0.140	0.260
TBC-AEE	C3	0.110	0.000	0.000
	C5	-0.120	-0.310	0.050
	C6	-0.020	-0.040	-0.140

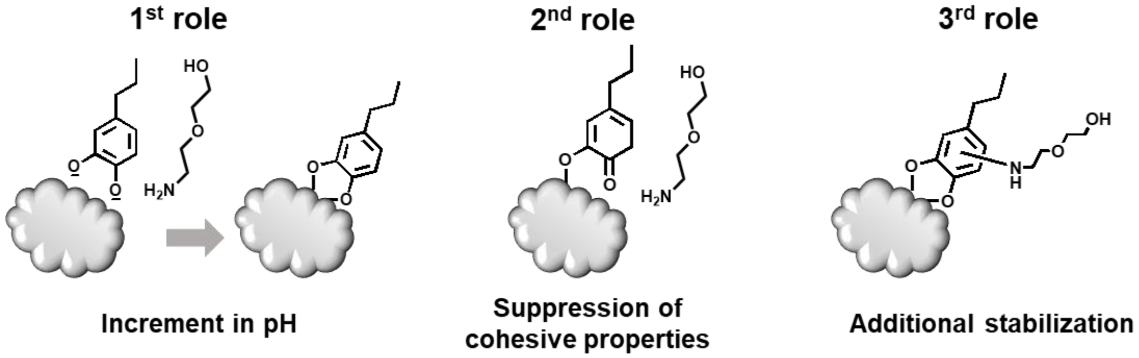

Scheme 2.2. Proposed three roles of AA during overall coating process.

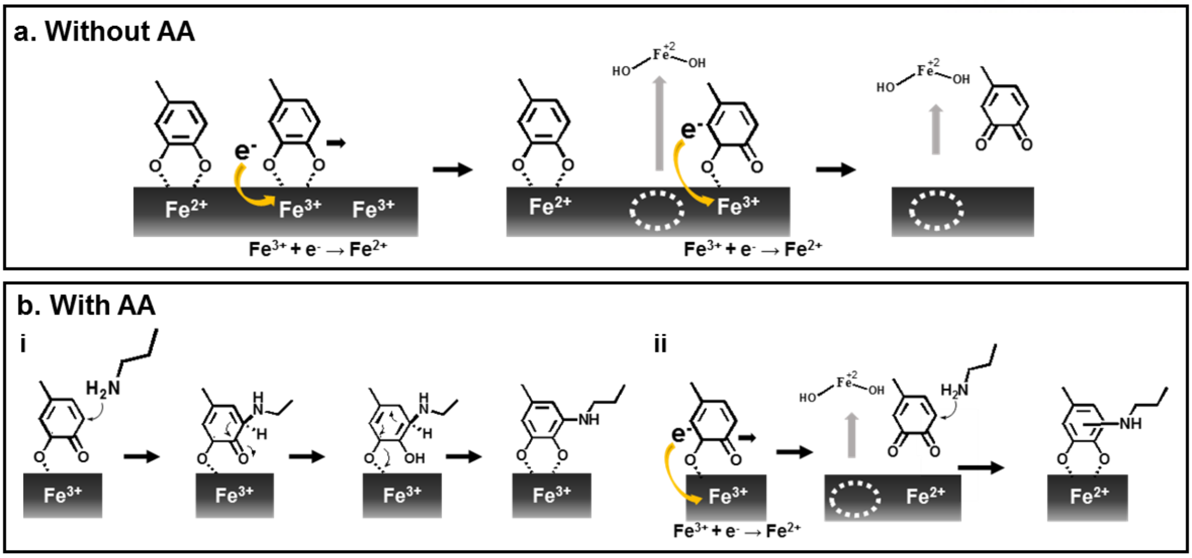

Figure 2.17. (a) Proposed mechanism for the formation of a catechol coating with no AA. Catechol loses its adhesion properties due to oxidation. Catechol-Fe^{3+} coordination on the substrate and electron transfer between catechol and Fe^{3} (left) occur, but the catechol-Fe^{2+} coordination maintains its bonding. The reduced Fe^{2+} ion elutes from the surface to the solution, and the oxidized catechol moves to the nearby iron ion (middle). Additional oxidation of the semiquinone causes detachment of the ligand in quinone form (right). (b) Proposed mechanisms for the formation of AANC. In the presence of AA, (i) the semiquinone can be recovered to a catechol-amine adduct by Michael addition of AA, and (ii) quinone can be recovered to a catechol-amine adduct.

2.4 Conclusion

We introduced an amine-mediated redox-controlled catechol-based nanocoating method. An extremely uniform (RMS < 0.358 ± 0.09 nm) and ultrathin (1.69 nm) coating was formed on flat substrates, and monodisperse layers with compact HD (<22 nm) on IONPs were achieved. The AACN method is not limited to certain chemicals but can expand its versatility by using various catecholic molecules and amino groups. This method is powerful for controlling the physicochemical properties of surfaces and is even applicable to areas of high curvature. Extensive characterization and mechanistic analyses were highlighted. The suggested mechanism of AACN, including the three key roles of the AA, provides new insight into understanding real mussel adhesion chemistry. The coating method can be applied to various nanostructured materials and provides a versatile platform. This study will provide inspiration and interesting themes for future studies of mussel adhesion and open a new gateway in conformal surface chemistry.

2.5 References

1. Deng, X.; Mammen, L.; Butt, H.-J.; Vollmer, D., Candle Soot as a Template for a Transparent Robust Superamphiphobic Coating. *Science* **2012,** *335* (6064), 67-70.

2. Hong, B. J.; Oh, S. J.; Youn, T. O.; Kwon, S. H.; Park, J. W., Nanoscale-Controlled Spacing Provides DNA Microarrays with the SNP Discrimination Efficiency in Solution Phase. *Langmuir* **2005,** *21* (10), 4257-4261.

3. Das, S.; Lee, B. H.; Linstadt, R. T. H.; Cunha, K.; Li, Y.; Kaufman, Y.; Levine, Z. A.; Lipshutz, B. H.; Lins, R. D.; Shea, J.-E.; Heeger, A. J.; Ahn, B. K., Molecularly Smooth Self-Assembled Monolayer for High-Mobility Organic Field-Effect Transistors. *Nano Lett.* **2016,** *16* (10), 6709-6715.

4. Gillich, T.; Benetti, E. M.; Rakhmatullina, E.; Konradi, R.; Li, W.; Zhang, A.; Schlüter, A. D.; Textor, M., Self-Assembly of Focal Point Oligo-catechol Ethylene Glycol Dendrons on Titanium Oxide Surfaces: Adsorption Kinetics, Surface Characterization, and Nonfouling Properties. *J. Am. Chem. Soc.* **2011,** *133* (28), 10940-10950.

5. Hong, S.; Kim, J.; Na, Y. S.; Park, J.; Kim, S.; Singha, K.; Im, G.-I.; Han, D.-K.; Kim, W. J.; Lee, H., Poly(norepinephrine): Ultrasmooth Material-Independent Surface Chemistry and Nanodepot for Nitric Oxide. *Angew. Chem. Int. Ed.* **2013,** *52* (35), 9187-9191.

6. Ahn, B. K.; Das, S.; Linstadt, R.; Kaufman, Y.; Martinez-Rodriguez, N. R.; Mirshafian, R.; Kesselman, E.; Talmon, Y.; Lipshutz, B. H.; Israelachvili, J. N.; Waite, J. H., High-performance mussel-inspired adhesives of reduced complexity. *Nat Commun* **2015,** *6*.

7. Sen, R.; Gahtory, D.; Carvalho, R. R.; Albada, B.; van Delft, F. L.; Zuilhof, H., Ultrathin Covalently Bound Organic Layers on Mica: Formation of Atomically Flat Biofunctionalizable Surfaces. *Angew. Chem. Int. Ed.* **2017,** *56* (15), 4130-4134.

8. Sileika, T. S.; Barrett, D. G.; Zhang, R.; Lau, K. H. A.; Messersmith, P. B., Colorless Multifunctional Coatings Inspired by Polyphenols Found in Tea, Chocolate, and Wine. *Angew. Chem. Int. Ed.* **2013,** *52* (41), 10766-10770.

9. Ejima, H.; Richardson, J. J.; Liang, K.; Best, J. P.; van Koeverden, M. P.; Such, G. K.; Cui, J.; Caruso, F., One-Step Assembly of Coordination Complexes for Versatile Film and Particle Engineering. *Science* **2013,** *341* (6142), 154-157.

10. Shultz, M. D.; Reveles, J. U.; Khanna, S. N.; Carpenter, E. E., Reactive Nature of Dopamine

as a Surface Functionalization Agent in Iron Oxide Nanoparticles. *J. Am. Chem. Soc.* **2007,** *129* (9), 2482-2487.

11. Lee, H.; Dellatore, S. M.; Miller, W. M.; Messersmith, P. B., Mussel-inspired surface chemistry for multifunctional coatings. *Science* **2007,** *318* (5849), 426-430.

12. Sara, M.; Carmelo, D.; Anna, M. F.; Alessandra, P.; Alessandro, P., Colloidal stability of iron oxide nanocrystals coated with a PEG-based tetra-catechol surfactant. *Nanotechnology* **2013,** *24* (10), 105702.

13. Ren, Y.; Rivera, J. G.; He, L.; Kulkarni, H.; Lee, D.-K.; Messersmith, P. B., Facile, high efficiency immobilization of lipase enzyme on magnetic iron oxide nanoparticles via a biomimetic coating. *BMC Biotechnology* **2011,** *11* (1), 63.

14. Lee, B. P.; Messersmith, P. B.; Israelachvili, J. N.; Waite, J. H., Mussel-Inspired Adhesives and Coatings. *Annual Review of Materials Research* **2011,** *41* (1), 99-132.

15. Maier, G. P.; Rapp, M. V.; Waite, J. H.; Israelachvili, J. N.; Butler, A., Adaptive synergy between catechol and lysine promotes wet adhesion by surface salt displacement. *Science* **2015,** *349* (6248), 628-632.

16. Gebbie, M. A.; Wei, W.; Schrader, A. M.; Cristiani, T. R.; Dobbs, H. A.; Idso, M.; Chmelka, B. F.; Waite, J. H.; Israelachvili, J. N., Tuning underwater adhesion with cation–π interactions. *Nat Chem* **2017,** *advance online publication*.

17. Wei, Q.; Achazi, K.; Liebe, H.; Schulz, A.; Noeske, P.-L. M.; Grunwald, I.; Haag, R., Mussel-Inspired Dendritic Polymers as Universal Multifunctional Coatings. *Angew. Chem. Int. Ed.* **2014,** *53* (43), 11650-11655.

18. Xu, H.; Nishida, J.; Ma, W.; Wu, H.; Kobayashi, M.; Otsuka, H.; Takahara, A., Competition between Oxidation and Coordination in Cross-Linking of Polystyrene Copolymer Containing Catechol Groups. *ACS Macro Letters* **2012,** *1* (4), 457-460.

19. Wilker, J. J., Biomaterials: Redox and adhesion on the rocks. *Nat Chem Biol* **2011,** *7* (9), 579-580.

20. Yu, J.; Wei, W.; Danner, E.; Ashley, R. K.; Israelachvili, J. N.; Waite, J. H., Mussel protein adhesion depends on interprotein thiol-mediated redox modulation. *Nat Chem Biol* **2011,** *7* (9), 588-590.

21. Hong, R.; Fischer, N. O.; Emrick, T.; Rotello, V. M., Surface PEGylation and Ligand Exchange Chemistry of FePt Nanoparticles for Biological Applications. *Chem. Mater.* **2005,** *17* (18), 4617-4621.

22. Lee, H.; Lee, B. P.; Messersmith, P. B., A reversible wet/dry adhesive inspired by mussels and geckos. *Nature* **2007,** *448* (7151), 338-341.

23. Aoyagi, N.; Endo, T., Functional RAFT agents for radical-controlled polymerization: Quantitative synthesis of trithiocarbonates containing functional groups as RAFT agents using equivalent amount of CS2. *J. Polym. Sci., Part A: Polym. Chem.* **2009,** *47* (14), 3702-3709.

24. Park, J.; An, K.; Hwang, Y.; Park, J.-G.; Noh, H.-J.; Kim, J.-Y.; Park, J.-H.; Hwang, N.-M.; Hyeon, T., Ultra-large-scale syntheses of monodisperse nanocrystals. *Nat Mater* **2004,** *3* (12), 891-895.

25. Kim, B. H.; Lee, N.; Kim, H.; An, K.; Park, Y. I.; Choi, Y.; Shin, K.; Lee, Y.; Kwon, S. G.; Na, H. B.; Park, J.-G.; Ahn, T.-Y.; Kim, Y.-W.; Moon, W. K.; Choi, S. H.; Hyeon, T., Large-Scale Synthesis of Uniform and Extremely Small-Sized Iron Oxide Nanoparticles for High-Resolution T_1 Magnetic Resonance Imaging Contrast Agents. *J. Am. Chem. Soc.* **2011,** *133* (32), 12624-12631.

26. Kwon, N. K.; Kim, H.; Han, I. K.; Shin, T. J.; Lee, H.-W.; Park, J.; Kim, S. Y., Enhanced Mechanical Properties of Polymer Nanocomposites Using Dopamine-Modified Polymers at Nanoparticle Surfaces in Very Low Molecular Weight Polymers. *ACS Macro Letters* **2018,** *7* (8), 962-967.

27. Segall, M. D.; Philip, J. D. L.; Probert, M. J.; Pickard, C. J.; Hasnip, P. J.; Clark, S. J.; Payne, M. C., First-principles simulation: ideas, illustrations and the CASTEP code. *J. Phys.: Condens. Matter* **2002,** *14* (11), 2717.

28. Perdew, J. P.; Zunger, A., Self-interaction correction to density-functional approximations for many-electron systems. *Physical Review B* **1981,** *23* (10), 5048-5079.

29. Perdew, J. P.; Burke, K.; Wang, Y., Generalized gradient approximation for the exchange-correlation hole of a many-electron system. *Physical Review B* **1996,** *54* (23), 16533-16539.

30. Hamann, D. R.; Schlüter, M.; Chiang, C., Norm-Conserving Pseudopotentials. *Phys. Rev. Lett.* **1979,** *43* (20), 1494-1497.

31. Santos-Carballal, D.; Roldan, A.; Grau-Crespo, R.; de Leeuw, N. H., A DFT study of the structures, stabilities and redox behaviour of the major surfaces of magnetite Fe_3O_4. *PCCP* **2014,** *16* (39), 21082-21097.

32. Tkatchenko, A.; Scheffler, M., Accurate Molecular Van Der Waals Interactions from Ground-State Electron Density and Free-Atom Reference Data. *Phys. Rev. Lett.* **2009,** *102* (7), 073005.

33. Monkhorst, H. J.; Pack, J. D., Special points for Brillouin-zone integrations. *Physical Review B* **1976,** *13* (12), 5188-5192.

34. Roldan, A.; Santos-Carballal, D.; Leeuw, N. H. d., A comparative DFT study of the mechanical and electronic properties of greigite Fe_3S_4 and magnetite Fe_3O_4. *The Journal of Chemical Physics* **2013,** *138* (20), 204712.

35. Wright, J. P.; Attfield, J. P.; Radaelli, P. G., Charge ordered structure of magnetite Fe_3O_4 below the Verwey transition. *Physical Review B* **2002,** *66* (21), 214422.

36. Yang, J.; Cohen Stuart, M. A.; Kamperman, M., Jack of all trades: versatile catechol crosslinking mechanisms. *Chem. Soc. Rev.* **2014,** *43* (24), 8271-8298.

37. Hong, S.; Wang, Y.; Park, S. Y.; Lee, H., Progressive fuzzy cation-π assembly of biological catecholamines. *Science Advances* **2018,** *4* (9), eaat7457.

38. Hong, S.; Yeom, J.; Song, I. T.; Kang, S. M.; Lee, H.; Lee, H., Pyrogallol 2-Aminoethane: A Plant Flavonoid-Inspired Molecule for Material-Independent Surface Chemistry. *Advanced Materials Interfaces* **2014,** *1* (4), 1400113.

39. Geißler, S.; Barrantes, A.; Tengvall, P.; Messersmith, P. B.; Tiainen, H., Deposition Kinetics of Bioinspired Phenolic Coatings on Titanium Surfaces. *Langmuir* **2016,** *32* (32), 8050-8060.

40. Yang, L.; Sun, H.; Jiang, W.; Xu, T.; Song, B.; Peng, R.; Han, L.; Jia, L., A Chemical Method for Specific Capture of Circulating Tumor Cells Using Label-Free Polyphenol-Functionalized Films. *Chem. Mater.* **2018,** *30* (13), 4372-4382.

41. Maerten, C.; Lopez, L.; Lupattelli, P.; Rydzek, G.; Pronkin, S.; Schaaf, P.; Jierry, L.; Boulmedais, F., Electrotriggered Confined Self-assembly of Metal–Polyphenol Nanocoatings Using a Morphogenic Approach. *Chem. Mater.* **2017,** *29* (22), 9668-9679.

42. Hu, H.; Dyke, J. C.; Bowman, B. A.; Ko, C.-C.; You, W., Investigation of Dopamine Analogues: Synthesis, Mechanistic Understanding, and Structure–Property Relationship. *Langmuir* **2016,** *32* (38), 9873-9882.

43. Rapp, M. V.; Maier, G. P.; Dobbs, H. A.; Higdon, N. J.; Waite, J. H.; Butler, A.; Israelachvili, J. N., Defining the Catechol–Cation Synergy for Enhanced Wet Adhesion to Mineral Surfaces. *J. Am. Chem. Soc.* **2016,** *138* (29), 9013-9016.

44. Cui, W.; Li, M.; Liu, J.; Wang, B.; Zhang, C.; Jiang, L.; Cheng, Q., A Strong Integrated Strength and Toughness Artificial Nacre Based on Dopamine Cross-Linked Graphene Oxide. *ACS Nano* **2014,** *8* (9), 9511-9517.

45. Han, L.; Lu, X.; Liu, K.; Wang, K.; Fang, L.; Weng, L.-T.; Zhang, H.; Tang, Y.; Ren, F.; Zhao, C.; Sun, G.; Liang, R.; Li, Z., Mussel-Inspired Adhesive and Tough Hydrogel Based on Nanoclay Confined Dopamine Polymerization. *ACS Nano* **2017,** *11* (3), 2561-2574.

46. Kang, T.; Oh, D. X.; Heo, J.; Lee, H. K.; Choy, S.; Hawker, C. J.; Hwang, D. S., Formation, Removal, and Reformation of Surface Coatings on Various Metal Oxide Surfaces Inspired by Mussel Adhesives. *Acs Appl Mater Inter* **2015,** *7* (44), 24656-24662.

47. Kang, T.; Banquy, X.; Heo, J. H.; Lim, C. N.; Lynd, N. A.; Lundberg, P.; Oh, D. X.; Lee, H. K.; Hong, Y. K.; Hwang, D. S.; Waite, J. H.; Israelachvili, J. N.; Hawker, C. J., Mussel-Inspired Anchoring of Polymer Loops That Provide Superior Surface Lubrication and Antifouling Properties. *Acs Nano* **2016,** *10* (1), 930-937.

48. Petoral, R. M.; Uvdal, K., Structural investigation of 3,4-dihydroxyphenylalanine-terminated propanethiol assembled on gold. *J Phys Chem B* **2003,** *107* (48), 13396-13402.

49. Boles, M. A.; Ling, D.; Hyeon, T.; Talapin, D. V., The surface science of nanocrystals. *Nat Mater* **2016,** *15* (2), 141-153.

50. Liu, W.; Howarth, M.; Greytak, A. B.; Zheng, Y.; Nocera, D. G.; Ting, A. Y.; Bawendi, M. G., Compact Biocompatible Quantum Dots Functionalized for Cellular Imaging. *J. Am. Chem. Soc.* **2008,** *130* (4), 1274-1284.

51. Ma, L.; Tu, C.; Le, P.; Chitoor, S.; Lim, S. J.; Zahid, M. U.; Teng, K. W.; Ge, P.; Selvin, P. R.; Smith, A. M., Multidentate Polymer Coatings for Compact and Homogeneous Quantum Dots with Efficient Bioconjugation. *J. Am. Chem. Soc.* **2016,** *138* (10), 3382-3394.

52. Polito, L.; Colombo, M.; Monti, D.; Melato, S.; Caneva, E.; Prosperi, D., Resolving the Structure of Ligands Bound to the Surface of Superparamagnetic Iron Oxide Nanoparticles by High-Resolution Magic-Angle Spinning NMR Spectroscopy. *J. Am. Chem. Soc.* **2008,** *130* (38), 12712-12724.

53. Henoumont, C.; Laurent, S.; Muller, R. N.; Vander Elst, L., HR-MAS NMR Spectroscopy: An Innovative Tool for the Characterization of Iron Oxide Nanoparticles Tracers for Molecular Imaging. *Anal. Chem.* **2015,** *87* (3), 1701-1710.

54. Lyu, Q.; Zhang, J.; Neoh, K. G.; Li Lin Chai, C., A one step method for the functional and property modification of DOPA based nanocoatings. *Nanoscale* **2017,** *9* (34), 12409-12415.

55. Tischer, T.; Claus, T. K.; Bruns, M.; Trouillet, V.; Linkert, K.; Rodriguez-Emmenegger, C.; Goldmann, A. S.; Perrier, S.; Börner, H. G.; Barner-Kowollik, C., Spatially Controlled

Photochemical Peptide and Polymer Conjugation on Biosurfaces. *Biomacromolecules* **2013,** *14* (12), 4340-4350.

56. Yu, Y.; Zhang, H.; Cui, S., Fabrication of robust multilayer films by triggering the coupling reaction between phenol and primary amine groups with visible light irradiation. *Nanoscale* **2011,** *3* (9), 3819-3824.

57. Liu, W.; Greytak, A. B.; Lee, J.; Wong, C. R.; Park, J.; Marshall, L. F.; Jiang, W.; Curtin, P. N.; Ting, A. Y.; Nocera, D. G.; Fukumura, D.; Jain, R. K.; Bawendi, M. G., Compact Biocompatible Quantum Dots via RAFT-Mediated Synthesis of Imidazole-Based Random Copolymer Ligand. *J. Am. Chem. Soc.* **2010,** *132* (2), 472-483.

58. Bonin, J.; Costentin, C.; Louault, C.; Robert, M.; Savéant, J.-M., Water (in Water) as an Intrinsically Efficient Proton Acceptor in Concerted Proton Electron Transfers. *J. Am. Chem. Soc.* **2011,** *133* (17), 6668-6674.

59. Amstad, E.; Gehring, A. U.; Fischer, H.; Nagaiyanallur, V. V.; Hähner, G.; Textor, M.; Reimhult, E., Influence of Electronegative Substituents on the Binding Affinity of Catechol-Derived Anchors to Fe3O4 Nanoparticles. *The Journal of Physical Chemistry C* **2010,** *115* (3), 683-691.

60. Oesterhelt, F.; Rief, M.; Gaub, H. E., Single molecule force spectroscopy by AFM indicates helical structure of poly(ethylene-glycol) in water. *New Journal of Physics* **1999,** *1*, 6-6.

61. Mentasti, E.; Pelizzetti, E.; Saini, G., Reactions between iron(III) and catechol (o-dihydroxybenzene). Part II. Equilibria and kinetics of the redox reaction in aqueous acid solution. *J. Chem. Soc., Dalton Trans.* **1973,** (23), 2609-2614.

62. Fullenkamp, D. E.; Barrett, D. G.; Miller, D. R.; Kurutz, J. W.; Messersmith, P. B., pH-dependent cross-linking of catechols through oxidation via Fe3+ and potential implications for mussel adhesion. *RSC Advances* **2014,** *4* (48), 25127-25134.

63. Lee, H.; Scherer, N. F.; Messersmith, P. B., Single-molecule mechanics of mussel adhesion. *Proceedings of the National Academy of Sciences* **2006,** *103* (35), 12999-13003.

64. Yu, J.; Wei, W.; Menyo, M. S.; Masic, A.; Waite, J. H.; Israelachvili, J. N., Adhesion of Mussel Foot Protein-3 to TiO2 Surfaces: the Effect of pH. *Biomacromolecules* **2013,** *14* (4), 1072-1077.

65. Lee, B. P.; Dalsin, J. L.; Messersmith, P. B., Synthesis and Gelation of DOPA-Modified Poly(ethylene glycol) Hydrogels. *Biomacromolecules* **2002,** *3* (5), 1038-1047.

66. Madrakian, T.; Afkhami, A.; Khalafi, L.; Mohammadnejad, M., Spectrophotometric

determination of catecholamines based on their oxidation reaction followed by coupling with 4-aminobenzoic acid. *Journal of the Brazilian Chemical Society* **2006,** *17*, 1259-1265.

67. Holten-Andersen, N.; Harrington, M. J.; Birkedal, H.; Lee, B. P.; Messersmith, P. B.; Lee, K. Y. C.; Waite, J. H., pH-induced metal-ligand cross-links inspired by mussel yield self-healing polymer networks with near-covalent elastic moduli. *Proceedings of the National Academy of Sciences* **2011,** *108* (7), 2651-2655.

68. Avdeef, A.; Sofen, S. R.; Bregante, T. L.; Raymond, K. N., Coordination chemistry of microbial iron transport compounds: Stability constants for catechol models of enterobactin. *J. Am. Chem. Soc.* **1978,** *100* (17), 5362-5370.

69. Rydzek, G.; Schaaf, P.; Voegel, J.-C.; Jierry, L.; Boulmedais, F., Strategies for covalently reticulated polymer multilayers. *Soft Matter* **2012,** *8* (38), 9738-9755.

70. Wu, J.; Zhang, L.; Wang, Y.; Long, Y.; Gao, H.; Zhang, X.; Zhao, N.; Cai, Y.; Xu, J., Mussel-Inspired Chemistry for Robust and Surface-Modifiable Multilayer Films. *Langmuir* **2011,** *27* (22), 13684-13691.

71. Asghari, A.; Ameri, M.; Baraee, B.; Rajabi, M.; Bakherad, M.; Amoozadeh, A., Mechanistic investigation of the electro-oxidation of catechols in the presence of N-methylbenzylamine at room temperature: synthesis of new quinone derivatives. *Progress in Reaction Kinetics and Mechanism* **2015,** *40* (1), 77-85.

72. Kramer, K. J.; Kanost, M. R.; Hopkins, T. L.; Jiang, H.; Zhu, Y. C.; Xu, R.; Kerwin, J. L.; Turecek, F., Oxidative conjugation of catechols with proteins in insect skeletal systems. *Tetrahedron* **2001,** *57* (2), 385-392.

73. Fouineau, J.; Brymora, K.; Ourry, L.; Mammeri, F.; Yaacoub, N.; Calvayrac, F.; Ammar-Merah, S.; Greneche, J. M., Synthesis, Mössbauer Characterization, and Ab Initio Modeling of Iron Oxide Nanoparticles of Medical Interest Functionalized by Dopamine. *The Journal of Physical Chemistry C* **2013,** *117* (27), 14295-14302.

Chapter 3. Amine-assisted catechol-based nanocoating on iron oxide nanoparticles for high-resolution magnetic resonance angiography

3.1 Introduction

IONPs have been extensively researched in the past decade as theranostic agent due to their superparamagnetism, large surface area, magnetic hyperthermia, and non-toxicity.[1-4] In bio-application, surface engineering of the IONPs is required for use in *in vitro* and in vivo experiments to obtain colloidal stability and stealth functionality in bio-media.[5, 6]Direct ligand exchange with catechol-tethered molecules is one of the established functionalization methods for metal oxide NPs since the pioneering research by Bing Xu et al. in 2004.[7] However, catechol-based ligands react with IONPs following a complex oxidative reaction pathway. Oxidation of catechol on the surface of IONPs is caused by a redox potential similar to that between catechol and Fe^{3+}.[8] Owing to this property, issues such as heterogeneous and large hydrodynamic diameters[9], low coating yields[10], and even etching of IONPs[11, 12] have been observed. Although cyclic brushes[13], long polyethylene glycol (PEG) chain length above 2kDa[14], and nitro-catechol derivatives[15] can provide catechol-based surface modified IONPs, catechol-based nanocoating on highly oxidative IONPs such as ultra-small IONP and maghemite (γ-Fe_2O_3) have still hampered by the presence of high amount of Fe^{3+}.[16]

The above mentioned issues have been rarely considered in the literature. Recently, an amine-assisted catechol-based nanocoating (AACN) was reported to provide a molecularly smooth monolayer by adding amines that mediated redox reaction of catechol. Suppressed detachment and polymerization of catechol from IONPs were accomplished using the AACN method. This strategy allows reproducible, compact, and uniform conformal coatings on metal oxide NPs.

Herein, we report our work on AACN applied to 3-nm-sized IONPs coated with a multidentate catechol-based PEG brush polymer (MCP). The resultant IONPs exhibited monodisperse hydrodynamic diameters, high compactness, and high colloidal stability. *In situ*-generated catechol-amine adducts on IONPs during AACN were analyzed by Fourier transform infrared (FT-IR) spectroscopy. Non-specific binding properties and non-toxicity were confirmed, and magnetic resonance (MR) relaxivity of the IONPs was evaluated. Finally, the obtained IONPs were used as a T_1 magnetic resonance imaging (MRI) contrast agent for *in vivo* high-resolution angiography.

3.2 Experimental section

3.2.1 Materials

Poly(ethylene glycol) methyl ether acrylate (average M_n = 480) (APEG) and 2-(2-aminoethxy) ethanol (AEE) were purchased from Sigma-Aldrich. Dopamine methacrylamide (DMA) and dibenzyl trithiocarbonate (DTC) were synthesized, as previously reported.[17, 18] Organic solvents were obtained from SAMCHUN CHEMICALS. Azobisisobutyronitrile (AIBN) was obtained from Junsei.

3.2.2 Synthesis of MCP

DMA (0.6 mmol), APEG (2.4 mmol), DTC (0.15 mmol), and AIBN (0.075 mmol) were mixed in a 10 ml vial then dissolved in 2 ml of dimethylformamide (DMF). The resulting mixture was transferred to an ampule; the ampule was subjected to 3 cycles of freeze-pump-thaw, followed by sealing with a gas torch under vacuum, then reacting in an oil bath at 70 °C for 12 h. After the reaction, the crude solution was precipitated with diethyl ether and washed three times.

3.2.3 Synthesis of IONPs

3 nm-sized IONPs were synthesized using a protocol previously reported in literature.[3] Iron oleate (1 mmol) and oleyl alcohol (6 mmol) were dissolved in 5 g of diphenyl ether. The mixture was heated to 250 °C at a heating rate of 3.3 $°C \cdot min^{-1}$ under an Ar atmosphere and kept at that temperature for 30 min. The resulting solution was cooled under inert conditions, and the product was collected by centrifugation in acetone and ethanol for 3 min at 5000 rpm.

3.2.4 Surface engineering of IONPs with MCP

Oleic-acid-capped IONPs (3 mg) in 300 µl of chloroform were mixed with 0.002 mmol of MCP and 0.2 mmol of AEE. The solution was allowed to react overnight in a glass vial at 60 °C with magnetic stirring. The crude solution was precipitated with ethyl ether to remove chloroform, and the pellet was dispersed in deionized water (D.W.). The aqueous solution was purified using a centrifugal membrane filter (Amicon Ultra-4 50 k) for 4000 rcf.

3.2.5 Instrumentation and analyses

The sizes of NPs were measured by transmission electron microscopy (TEM, JEOL, JEM-2100) conducted at 200 kV, for which the dispersed samples were placed on a carbon copper grid for measurement. The hydrodynamic diameter was studied using a dynamic light scattering (DLS, Malvern Instruments, Zetasizer Nano-ZS90) at 25 °C. UV-Vis spectra were measured on a UV-Vis spectroscopy (Shimadzu, UV-1800) with a quartz cuvette. FT-IR spectra were measured by a FT-IR spectroscopy (Varian, 670/620). The molecular weight of the resultant polymers was measured using a gel permeation chromatography (GPC, Agilent, 1200S system) at 25 °C. All samples before measurement were filtered using a 0.2 μm PTFE syringe filter. Tetrahydrofuran was used as an eluent, and polystyrene standards were used for calibration.

3.2.6 Serum binding test

MCP-coated 3 nm IONPs (20 mM Fe) were incubated in 100% FBS at 37 °C for 30 min. Fast protein liquid chromatography (FPLC, GE Healthcare Life Sciences, AKTA pure) with a Superose 6 10/300 GL column was performed for analysis.

3.3 Result and discussion

Reversible addition-fragmentation chain-transfer (RAFT) polymerization method was chosen for the preparation of MCP (Figure 3.1a).[19, 20] This synthetic approach gives a synergistic effect for controlling the physical properties of IONPs with AACN, because of its uniform polymer length and controllable functional groups. In addition, RAFT polymerization is attractive owing to its functional versatility due to the existence of a vast library of vinyl monomers. We have synthesized various molecular weight controlled polymers and degree of polymer (DP) obtained by GPC gave a proportional relationship to [Monomer]:[RAFT] ratio with a narrow polydispersity index (PDI) about 1.3 (Figure 3.2). For example, in case of polymer with DP 20, the product was obtained with high conversion yield over than 95% with molecular weight of 8200 and narrow PDI with 1.19. Figure 3.1b shows the AACN on IONPs with MCP and amine additives (AA), using AEE as the amine. The scheme includes the reduction process of oxidized catechol by AA. The recovered catechol-amine adduct binds strongly on the surface of IONPs. In figure 3.1c, a detailed mechanistic description of the catecholic nanocoating with and without AA is shown. First, the coordination bond between catechol and the iron ion is facilitated in basic conditions by AA[21]. Catechol is oxidized due to a similar redox potential between catechol and Fe3+ (~0.75 V).[22] In the presence of AA, the semiquinones react with the nucleophilic AA, and the catechol-amine adduct is formed. The affinity of catechol can be recovered through the reaction and the generated adduct additionally stabilizes the coordination bond. However, consecutive electron transfers between catechol and the iron ions occur in the case of no AA, and the resultant quinones are detached from the IONPs. Oxidative polymerization was also possible from the resultant quinone, and aggregation of IONPs was caused by the loss of affinity and crosslinking of catechol.

Surface engineering a 3 nm-sized oleic acid-capped IONPs with MCP in the presence of AA is shown in Figure 3.3. The photograph was taken after MCP coating on 3 nm-sized IONPs with (IONP@MCP/AEE) and without AA (IONP@MCP). The IONPs were dispersed in D.W. after AACN with MCP. A significant precipitant occurred in the case of the MCP. A coating without AA is seen (Figure 3.3a). Dynamic light scattering (DLS) measurements show that the IONP@MCP/AEE has a monomodal and narrow size distribution in D.W. with a hydrodynamic diameter (HD) of 10.1 nm (Figure 3.3b). DLS of IONP@MCP shows a heterogeneous size distribution and signs of severe agglomeration (98.4 nm, 63%, and 370 nm, 37%). The TEM data for IONP@MCP/AEE and IONP@Oleic acid show an average particle size of 3.4 ± 0.40 nm and 3.2 ± 0.47 nm, respectively (Figure 3.4). The morphology of the IONPs is maintained and no evidence of etching is observed. From the DLS and TEM data, we concluded that the AACN with the polymeric ligand could be

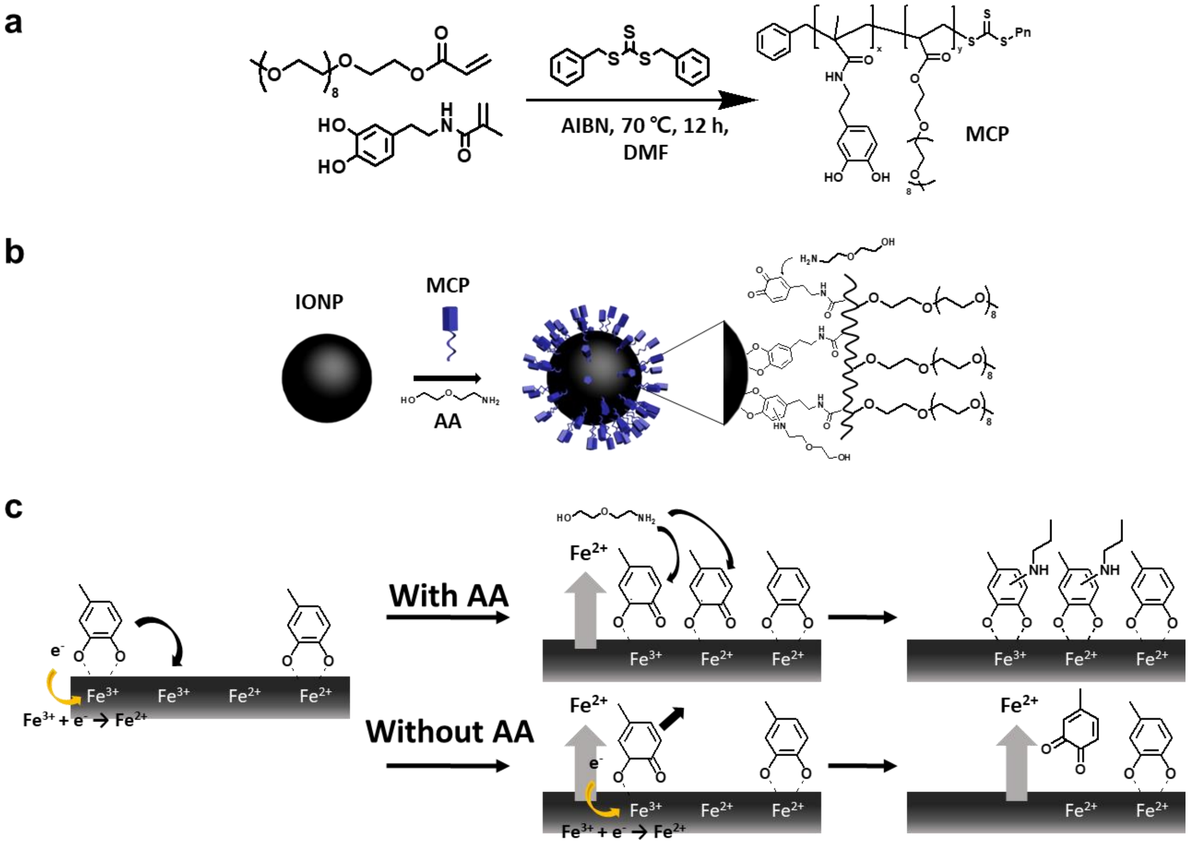

Figure 3.1. (a) Synthesis of MCP by RAFT polymerization, (b) Schematic illustration of AACN procedure with MCP and AEE on IONPs, and (c) a detailed mechanistic description of catecholic nanocoating with and without AA.

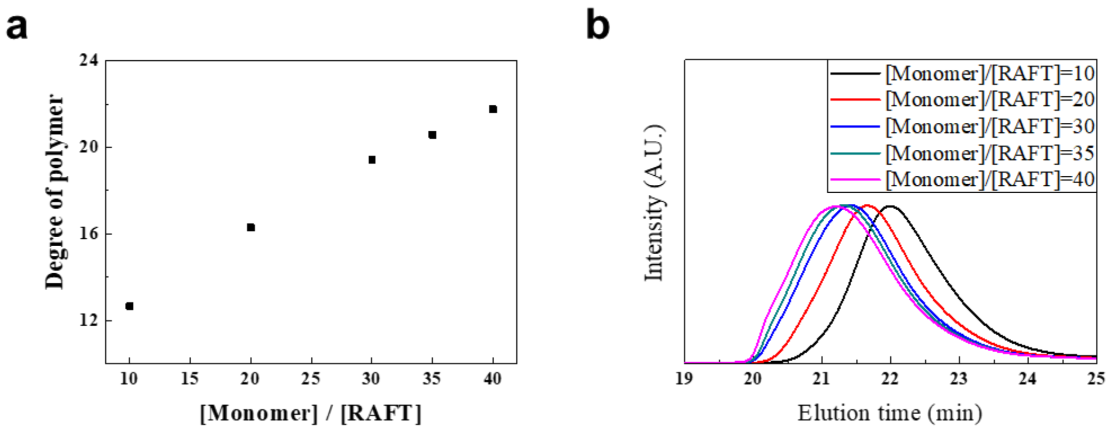

Figure 3.2. (a) Tunable DP of MCP as a function of [Monomer] to [RAFT] ratio, (b) GPC traces of MCP at different [Monomer] to [RAFT] ratios in synthetic procedures.

adjusted on ultrasmall IONPs containing high amount of Fe^{3+}.

The colloidal stability and nonspecific affinity were evaluated to study the potential for use *in vivo* application (Figure 3.5). The IONP@MCP/AEE is stable over a wide pH range (5-11) and in NaCl concentrations up to 2 M for at least one month (Figure 3.5a). The image shown in Figure 3.5c also exhibits high colloidal stability over the physiological pH range and in NaCl concentrations up to 2 M for 30 days. Nanocoated 8.5 nm and 12 nm-sized IONPs were also evaluated and showed similar stability for 3 nm IONP@MCP@AEE (Figure 3.6). The serum binding test for nanocoated IONPs was performed to elucidate its nonspecific affinity in protein, including in solutions such as fetal bovine serum (FBS), which is a widely used serum for cell experiments.[23] Size exclusion chromatography was used to investigate protein adsorption on NPs by comparing the change in size.[24] The IONP@MCP/AEE in 1x PBS and IONP@MCP/AEE in FBS solution were incubated at 37 °C for 30 min and then analyzed (Figure 3.5b). Interestingly, both IONP in 1x PBS and FBS showed nearly same elution time (41 min) and a monodispersed size distribution, meaning IONPs@MCP/AEE shows corona-free characteristics. Unstable or non-passivated NPs can interact with various proteins and lipids present in serum in vivo, resulting in corona structures.[25] The corona cause loss of targeting ability and accumulation of NPs by the mononuclear phagocytic system.[26,27] Unpredictable localization and reduced circulation time of NPs in vivo was adversely affected by the MR imaging process. Completely suppressed nonspecific interaction of NPs with biomedia could be achieved via amine-assisted MCP coating, which contains PEG molecules of a relatively short length (n ~9) compared to commonly available longer PEG molecules (n >50). Dense coating and strong binding affinity of the catechol-amine adduct to IONPs are reasons for the results reported herein.[13] Moreover, *in vitro* cell viability and cytotoxicity tests were performed using HeLa cells to prove the non-toxicity of IONP@MCP/AEE.

FT-IR studies were conducted on IONP@Oleic acid, MCP, IONP@MCP, and IONP@MCP/AEE to investigate the molecular structure of the surface. The full FT-IR spectra are described in Figure 3a. These spectra were analyzed by separating them into three regions, (I), (II), and (III). (I) is the 750–1000 cm-1 range. This region is optimal for the analysis of the aromatic groups in catechol (Figure 3b). The vibration at 850 cm-1 for MCP is reduced after AACN on IONPs. This result indicates that a substituent change in the aromatic group occurred when AEE was used during the MCP coating process.[28] The vibration band at 800 cm-1 is from the Fe-OH bond in the IONPs.[29] In region (II), MCP exhibited a catechol band (1450 cm-1). A clear peak split (1453 cm-1 and 1473 cm-1) of the band was observed in only IONP@MCP/AEE (Figure 3c). The splitting is evidence of metal binding, as reported in the literature.[30, 31] (III) shows an enlargement of the area between 1550 and 1800 cm-1 indicating the C=C vibration of the benzene ring (Figure 3d). The signal was dramatically reduced for IONP@MCP compared with MCP and IONP@MCP/AEE. The data demonstrate that oxidation and oxidative polymerization with molecules in the vicinity of catechol occurs after coating without AA.

r1 and r2 relaxivities were recorded on a 1.4 T magnet NMR minispec and 3T MR scanner to confirm the potential of the nanocoated IONP to have an MR contrast agent. Tables 1 and 2 summarize the relaxometric properties of various sized IONP@MCP/AEE. In particular, the r1 value for 3-nm-sized IONPs was 3.42 mM-1s-1, comparable to that of the 3-nm-sized IONPs reported in other papers.[3, 23] A low r2/r1 value is necessary for a satisfactory T_1-weighted MR image, and the r2 value for 3-nm-sized IONPs is the lowest among the studied IONPs, demonstrating that 3 nm IONP@MCP/AEE can be used as an efficient T_1 contrast agent.[3]

We used the amine-assisted MCP nanocoated 3 nm-sized IONP as an MR angiography contrast agent. The blood vessel imaging can provide important information related to diseases such as renal failure, thrombosis, tumor angiogenesis, and myocardial infarction. However, conventional imaging agents, like DOTAREM, are not adequately sensitive, because of their low circulation time in vivo. The blood pool MR image was recorded using a 3T MRI instrument, and the IONPs (2.5 mg Fe·kg^{-1}) were intravenously injected into a rat through the tail. High contrast in whole blood vessels was observed as soon as the IONPs were injected (Figure 3.8). IONP-enhanced MR images were tracked for up to 82 min with a dynamic time-resolved MR sequence. The aorta, axillary vein, jugular vein, carotid artery, and cerebral veins were detected as a two-dimensional MIP image due to signal enhancement of IONPs. In addition, the MR enhancement signal was maintained over 80 min, indicating the IONP@MCP/AEE is beneficial for achieving steady-state imaging.

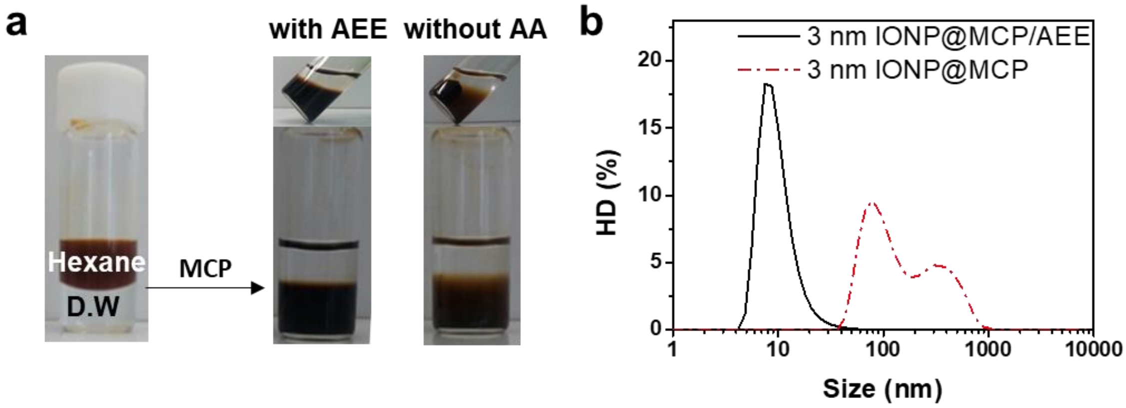

Figure 3.3. (a) Photograph of IONPs before (left), after MCP coating with AEE (middle), and without AA (right). (b) DLS data of IONP@MCP/AEE and IONP@MCP.

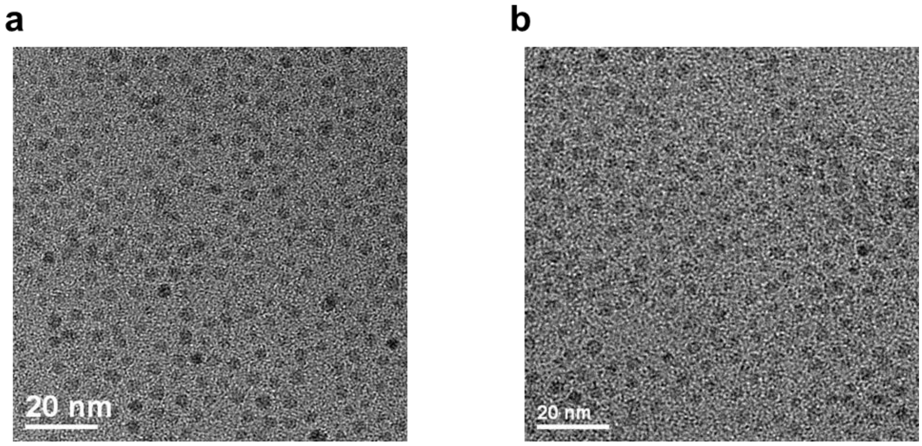

Figure 3.4. TEM image of (a) oleic acid-capped 3 nm-sized IONPs, and (b) MCP coated 3 nm sized IONPs by assistance of AEE.

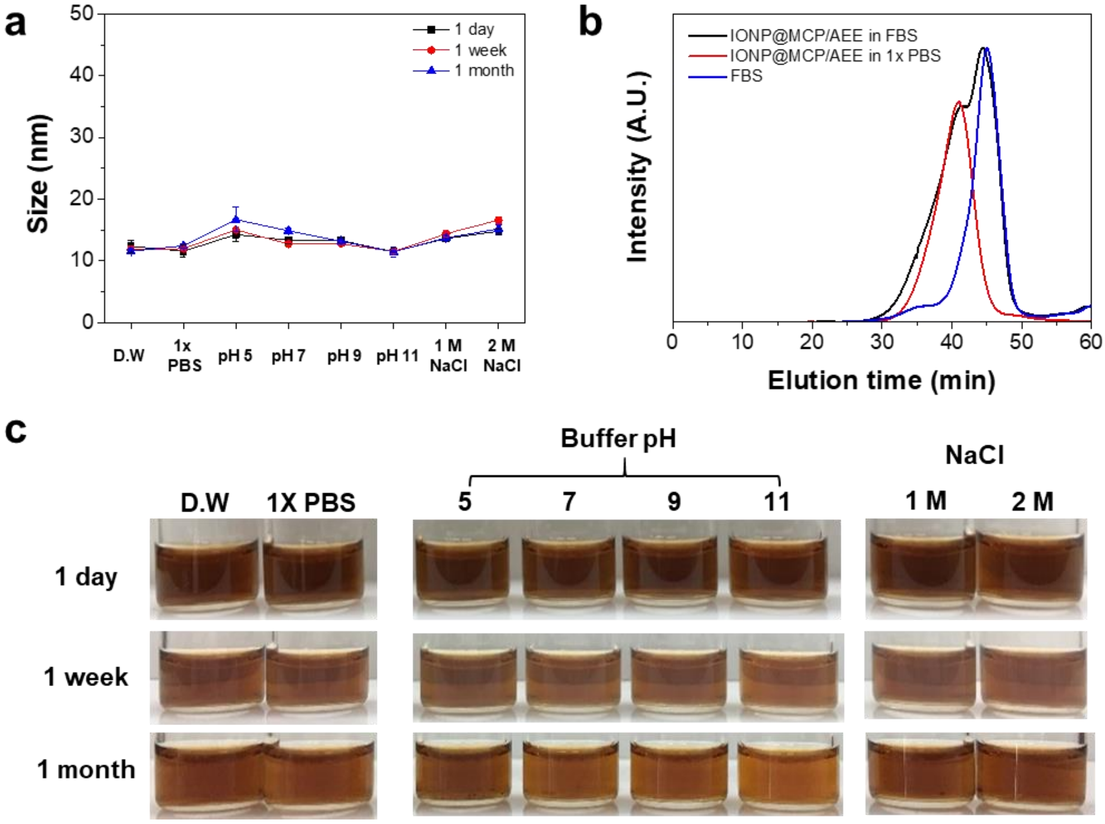

Figure 3.5. (a) HD of IONP@MCP/AEE in various pH and salt concentration over time. (b) Serum binding test through size exclusion chromatography. (c) Stability evaluation of IONP@MCP/AEE in various pH buffers and salt concentration.

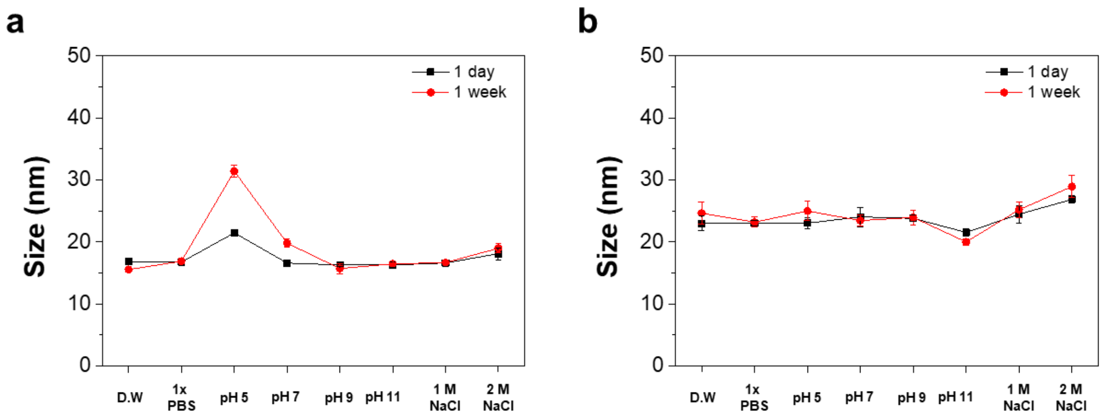

Figure 3.6. Stability measurement of MCP nanocoated (a) 8 nm and (b) 12 nm-sized IONPs by DLS in the wide range of pH and salt concentration.

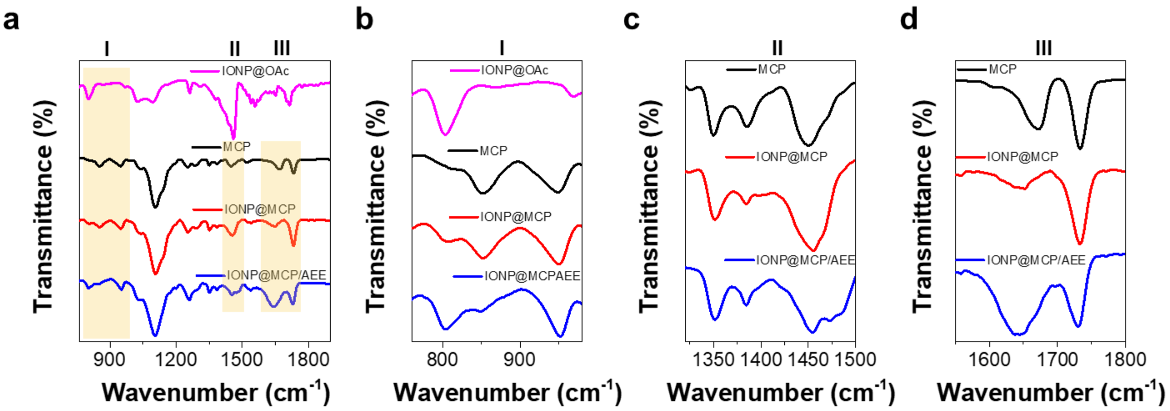

Figure 3.7. Structural analysis of nanocoating layer on IONPs by FT-IR. FT-IR spectra of (a) IONP@Oleic acid, MCP, IONP@MCP, and IONP@MCP/AEE. Enlarged version of yellow boxes (b) region I, (c) region II, and (d) region III.

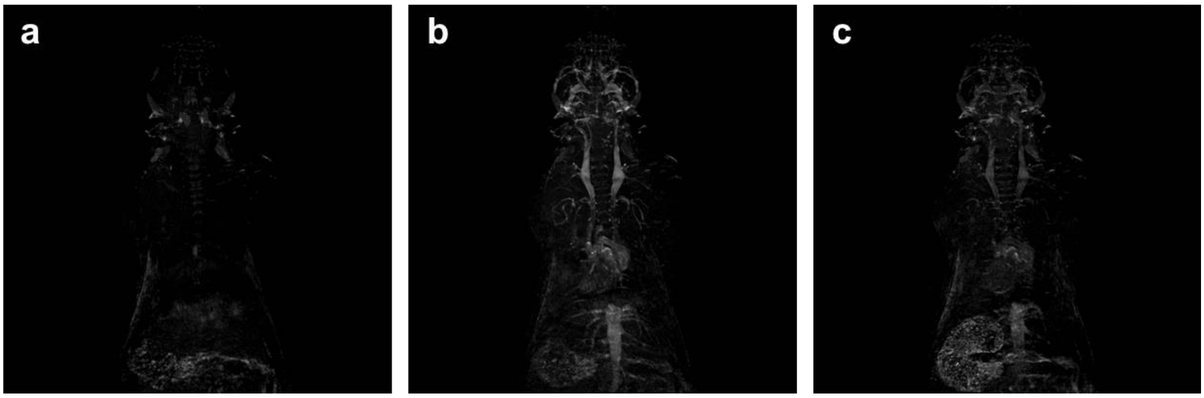

Figure 3.8. MR in vivo angiograohy with dynamic time-resolved MR sequence (a) before injection of IONPs, (b) after injection of IONPs, and (c) 1 hour after injection of IONPs.

3.4 Conclsuion

We reported the MCP coated IONPs by AACN method. The resultant product exhibited monodisperse, compact, and stable colloidal nanocrystals in aqueous solution. Oxidized catechols recover their affinity and uncontrolled cohesion is suppressed by addition reaction with primary amine additives. The simple coating strategy via separated amine shows that the catecholic ligand can efficiently passivate highly oxidized 3 nm-sized IONPs by modulation of catechol redox chemistry. We prove that the corona-free properties in biomedia, and high stability in wide range of pH and salt of the nanocoated IONPs promise the high resolution MR angiography *in vivo*.

3.5 References

1. El-Boubbou, K.; Zhu, D. C.; Vasileiou, C.; Borhan, B.; Prosperi, D.; Li, W.; Huang, X., Magnetic Glyco-Nanoparticles: A Tool To Detect, Differentiate, and Unlock the Glyco-Codes of Cancer via Magnetic Resonance Imaging. *J. Am. Chem. Soc.* **2010,** *132* (12), 4490-4499.

2. Tong, S.; Quinto, C. A.; Zhang, L.; Mohindra, P.; Bao, G., Size-Dependent Heating of Magnetic Iron Oxide Nanoparticles. *ACS Nano* **2017,** *11* (7), 6808-6816.

3. Kim, B. H.; Lee, N.; Kim, H.; An, K.; Park, Y. I.; Choi, Y.; Shin, K.; Lee, Y.; Kwon, S. G.; Na, H. B.; Park, J.-G.; Ahn, T.-Y.; Kim, Y.-W.; Moon, W. K.; Choi, S. H.; Hyeon, T., Large-Scale Synthesis of Uniform and Extremely Small-Sized Iron Oxide Nanoparticles for High-Resolution T_1 Magnetic Resonance Imaging Contrast Agents. *J. Am. Chem. Soc.* **2011,** *133* (32), 12624-12631.

4. Laurent, S.; Dutz, S.; Häfeli, U. O.; Mahmoudi, M., Magnetic fluid hyperthermia: Focus on superparamagnetic iron oxide nanoparticles. *Adv. Colloid Interface Sci.* **2011,** *166* (1), 8-23.

5. Boles, M. A.; Ling, D.; Hyeon, T.; Talapin, D. V., The surface science of nanocrystals. *Nat Mater* **2016,** *15* (2), 141-153.

6. Laurent, S.; Forge, D.; Port, M.; Roch, A.; Robic, C.; Vander Elst, L.; Muller, R. N., Magnetic Iron Oxide Nanoparticles: Synthesis, Stabilization, Vectorization, Physicochemical Characterizations, and Biological Applications. *Chem. Rev.* **2008,** *108* (6), 2064-2110.

7. Xu, C.; Xu, K.; Gu, H.; Zheng, R.; Liu, H.; Zhang, X.; Guo, Z.; Xu, B., Dopamine as A Robust Anchor to Immobilize Functional Molecules on the Iron Oxide Shell of Magnetic Nanoparticles. *J. Am. Chem. Soc.* **2004,** *126* (32), 9938-9939.

8. Yang, J.; Cohen Stuart, M. A.; Kamperman, M., Jack of all trades: versatile catechol crosslinking mechanisms. *Chem. Soc. Rev.* **2014,** *43* (24), 8271-8298.

9. Sara, M.; Carmelo, D.; Anna, M. F.; Alessandra, P.; Alessandro, P., Colloidal stability of iron oxide nanocrystals coated with a PEG-based tetra-catechol surfactant. *Nanotechnology* **2013,** *24* (10), 105702.

10. Li, P.; Chevallier, P.; Ramrup, P.; Biswas, D.; Vuckovich, D.; Fortin, M.-A.; Oh, J. K., Mussel-Inspired Multidentate Block Copolymer to Stabilize Ultrasmall Superparamagnetic Fe3O4 for Magnetic Resonance Imaging Contrast Enhancement and Excellent Colloidal Stability. *Chem. Mater.* **2015,** *27* (20), 7100-7109.

11. Shultz, M. D.; Reveles, J. U.; Khanna, S. N.; Carpenter, E. E., Reactive Nature of Dopamine as a Surface Functionalization Agent in Iron Oxide Nanoparticles. *J. Am. Chem. Soc.* **2007,** *129* (9), 2482-2487.

12. Xie, J.; Xu, C.; Xu, Z.; Hou, Y.; Young, K. L.; Wang, S. X.; Pourmand, N.; Sun, S., Linking Hydrophilic Macromolecules to Monodisperse Magnetite (Fe3O4) Nanoparticles via Trichloro-s-triazine. *Chem. Mater.* **2006,** *18* (23), 5401-5403.

13. Morgese, G.; Shirmardi Shaghasemi, B.; Causin, V.; Zenobi-Wong, M.; Ramakrishna, S. N.; Reimhult, E.; Benetti, E. M., Next-Generation Polymer Shells for Inorganic Nanoparticles are Highly Compact, Ultra-Dense, and Long-Lasting Cyclic Brushes. *Angew. Chem. Int. Ed.* **2017,** *56* (16), 4507-4511.

14. Gal, N.; Lassenberger, A.; Herrero-Nogareda, L.; Scheberl, A.; Charwat, V.; Kasper, C.; Reimhult, E., Interaction of Size-Tailored PEGylated Iron Oxide Nanoparticles with Lipid Membranes and Cells. *ACS Biomaterials Science & Engineering* **2017,** *3* (3), 249-259.

15. Amstad, E.; Gillich, T.; Bilecka, I.; Textor, M.; Reimhult, E., Ultrastable Iron Oxide Nanoparticle Colloidal Suspensions Using Dispersants with Catechol-Derived Anchor Groups. *Nano Lett.* **2009,** *9* (12), 4042-4048.

16. Amstad, E.; Gehring, A. U.; Fischer, H.; Nagaiyanallur, V. V.; Hähner, G.; Textor, M.; Reimhult, E., Influence of Electronegative Substituents on the Binding Affinity of Catechol-Derived Anchors to Fe3O4 Nanoparticles. *The Journal of Physical Chemistry C* **2010,** *115* (3), 683-691.

17. Lee, H.; Lee, B. P.; Messersmith, P. B., A reversible wet/dry adhesive inspired by mussels and geckos. *Nature* **2007,** *448* (7151), 338-341.

18. Aoyagi, N.; Endo, T., Functional RAFT agents for radical-controlled polymerization: Quantitative synthesis of trithiocarbonates containing functional groups as RAFT agents using equivalent amount of CS2. *J. Polym. Sci., Part A: Polym. Chem.* **2009,** *47* (14), 3702-3709.

19. Kwon, N. K.; Kim, H.; Han, I. K.; Shin, T. J.; Lee, H.-W.; Park, J.; Kim, S. Y., Enhanced Mechanical Properties of Polymer Nanocomposites Using Dopamine-Modified Polymers at Nanoparticle Surfaces in Very Low Molecular Weight Polymers. *ACS Macro Lett.* **2018,** *7* (8), 962-967.

20. Na, H.-K.; Kim, H.; Son, J. G.; Lee, J. H.; Kim, J.-K.; Park, J.; Lee, T. G., Facile synthesis and direct characterization of surface-charge-controlled magnetic iron oxide nanoparticles and their role in gene transfection in human leukemic T cell. *Appl. Surf. Sci.* **2019,** *483*, 1069-1080.

21. Yu, J.; Wei, W.; Menyo, M. S.; Masic, A.; Waite, J. H.; Israelachvili, J. N., Adhesion of Mussel Foot Protein-3 to TiO2 Surfaces: the Effect of pH. *Biomacromolecules* **2013,** *14* (4), 1072-1077.

22. Powell, H.; Taylor, M., Interactions of iron(II) and iron(III) with gallic acid and its homologues: a potentiometric and spectrophotometric study. *Aust. J. Chem.* **1982,** *35* (4), 739-756.

23. Tromsdorf, U. I.; Bruns, O. T.; Salmen, S. C.; Beisiegel, U.; Weller, H., A Highly Effective, Nontoxic T_1 MR Contrast Agent Based on Ultrasmall PEGylated Iron Oxide Nanoparticles. *Nano Lett.* **2009,** *9* (12), 4434-4440.

24. Wei, H.; Insin, N.; Lee, J.; Han, H.-S.; Cordero, J. M.; Liu, W.; Bawendi, M. G., Compact Zwitterion-Coated Iron Oxide Nanoparticles for Biological Applications. *Nano Lett.* **2011,** *12* (1), 22-25.

25. Lundqvist, M.; Stigler, J.; Cedervall, T.; Berggård, T.; Flanagan, M. B.; Lynch, I.; Elia, G.; Dawson, K., The Evolution of the Protein Corona around Nanoparticles: A Test Study. *ACS Nano* **2011,** *5* (9), 7503-7509.

26. Salvati, A.; Pitek, A. S.; Monopoli, M. P.; Prapainop, K.; Bombelli, F. B.; Hristov, D. R.; Kelly, P. M.; Aberg, C.; Mahon, E.; Dawson, K. A., Transferrin-functionalized nanoparticles lose their targeting capabilities when a biomolecule corona adsorbs on the surface. *Nat. Nano* **2013,** *8* (2), 137-143.

27. Alexis, F.; Pridgen, E.; Molnar, L. K.; Farokhzad, O. C., Factors Affecting the Clearance and Biodistribution of Polymeric Nanoparticles. *Molecular Pharmaceutics* **2008,** *5* (4), 505-515.

28. Wei, Q.; Achazi, K.; Liebe, H.; Schulz, A.; Noeske, P.-L. M.; Grunwald, I.; Haag, R., Mussel-Inspired Dendritic Polymers as Universal Multifunctional Coatings. *Angew. Chem. Int. Ed.* **2014,** *53* (43), 11650-11655.

29. Huang, X.; Schmucker, A.; Dyke, J.; Hall, S. M.; Retrum, J.; Stein, B.; Remmes, N.; Baxter, D. V.; Dragnea, B.; Bronstein, L. M., Magnetic nanoparticles with functional silanes: evolution of well-defined shells from anhydride containing silane. *J. Mater. Chem.* **2009,** *19* (24), 4231-4239.

30. Sever, M. J.; Weisser, J. T.; Monahan, J.; Srinivasan, S.; Wilker, J. J., Metal-Mediated Cross-Linking in the Generation of a Marine-Mussel Adhesive. *Angew. Chem. Int. Ed.* **2004,** *43* (4), 448-450.

31. Pecoraro, V. L.; Harris, W. R.; Wong, G. B.; Carrano, C. J.; Raymond, K. N., Coordination chemistry of microbial iron transport compounds. 23. Fourier transform infrared spectroscopy of

ferric catechoylamide analogues of enterobactin. *J. Am. Chem. Soc.* **1983,** *105* (14), 4623-4633.

Chapter 4. Facile synthesis and direct characterization of surface-charge-controlled magnetic iron oxide nanoparticles and their role in gene transfection in human leukemic T cell

4.1 Introduction

An important consideration for the practical biomedical application of nanoparticles (NPs) is the processes involved in their surface modification.[1-8] Indeed, many studies have concluded that the surface characteristics of NPs affect their interactions with biological systems, including proteins and cells.[9-12] For this reason alone, applying NPs to areas of biotechnology, including *in vitro* diagnosis and *in vivo* therapy, would necessitate designing and modifying their surfaces according to their purposes.[13, 14] However, other concerns also provide justification. Since the surface functionality of the NPs influences their cytotoxicity and cellular uptake efficiency, it is critical to be able to accurately predict and control the phenomena that occur at the interface between the NPs and biological systems. For example, since a generation of positively charged surfaces with suitable charge ratios is necessary in gene transfection for safe and efficient gene delivery, it is essential to prepare NPs surfaces that are conjugated with non-toxic and adequately positively charged molecules.[15-20] NPs with different surface charge states (positive, neutral, and negative) have been synthesized and evaluated their interaction with cells, however large (>30 nm), heterogeneous size, unstable and lack of characterization of NPs hamper exact evaluation of the NPs.[3, 21-24]. In addition, careful analysis of the modified NPs surface should be carried out to obtain reliable information on surface functionality-performance relationships. Purity verification is also needed because, once a reaction is complete, the remaining molecules must be removed to avoid unpredictable biological behavior when the modified NPs are applied to a living system.

Despite these important considerations, current characterization methods are limited to checking the bulk characteristics of surface-modified NPs rather than analyzing in detail the molecular structures of the NPs surfaces.[6] There is an urgent need, then, for precise characterization tools that can provide chemical information on the functional groups on NPs surfaces without additional labeling.[19] Mass-spectrometry-based imaging can provide direct evidence for the presence of molecules and functional groups on NPs surfaces after their modification, and, among the various mass spectrometry methods, time-of-flight secondary ion mass spectrometry (ToF-SIMS) has proved to be a sensitive surface analytical tool in industrial applications.[25] Due to its ability to provide chemical and spatial information on both surface functional groups and core NPs, ToF-SIMS analysis is useful for the direct observation of surface functional moieties on NPs, to verify their successful modification and purification. FT-IR-spectroscopy-based imaging can be used to corroborate the analytical data obtained by ToF-SIMS imaging[25, 26] as well as to provide further molecular structural and binding information. Recently, Lee *et al*. reported that the combination of composition and functional group analyses by ToF-SIMS and FT-IR imaging on micro-aggregated NPs sampled on a Si wafer was able to reveal the spatial distribution and binding schemes of NPs ligand candidates to provide accurate surface chemical information of the binding schemes of surface ligands.[27] A similar partnering of compositional analysis by ToF-SIMS and functional-group analysis by FT-IR may facilitate an accurate understanding of NPs surfaces modified with different charge states. Here, we present the facile synthesis and precise surface characterization of well-designed and charge-controlled (positive, neutral, and negative) iron oxide (Fe_3O_4) NPs based on the use of ligands bearing a dopamine-containing block copolymer; a thorough analysis of the ligand molecules; and the interactions of the resultant NPs with live cells. ToF-SIMS imaging analysis together with FT-IR spectroscopy imaging allowed the molecular identification and spatial distribution for both the NPs and the surface conjugate (and unconjugated) ligands, providing direct evidence for the presence and integrity of the ligands on the NPs. Using these well-designed and characterized Fe_3O_4 NPs, we investigated the influence of their surface charge properties on their interactions with mammalian cells. Furthermore, we demonstrated that an appropriate surface charge modification plays a key role in intracellular uptake as well as in efficient gene transfection into suspension type cell, the Jurkat human leukemic T cell, which is generally regarded as being very difficult.[28] Our study of surface-charge-controlled NPs for biomedical applications such as efficient gene transfection is summarized in Figure 4.1.

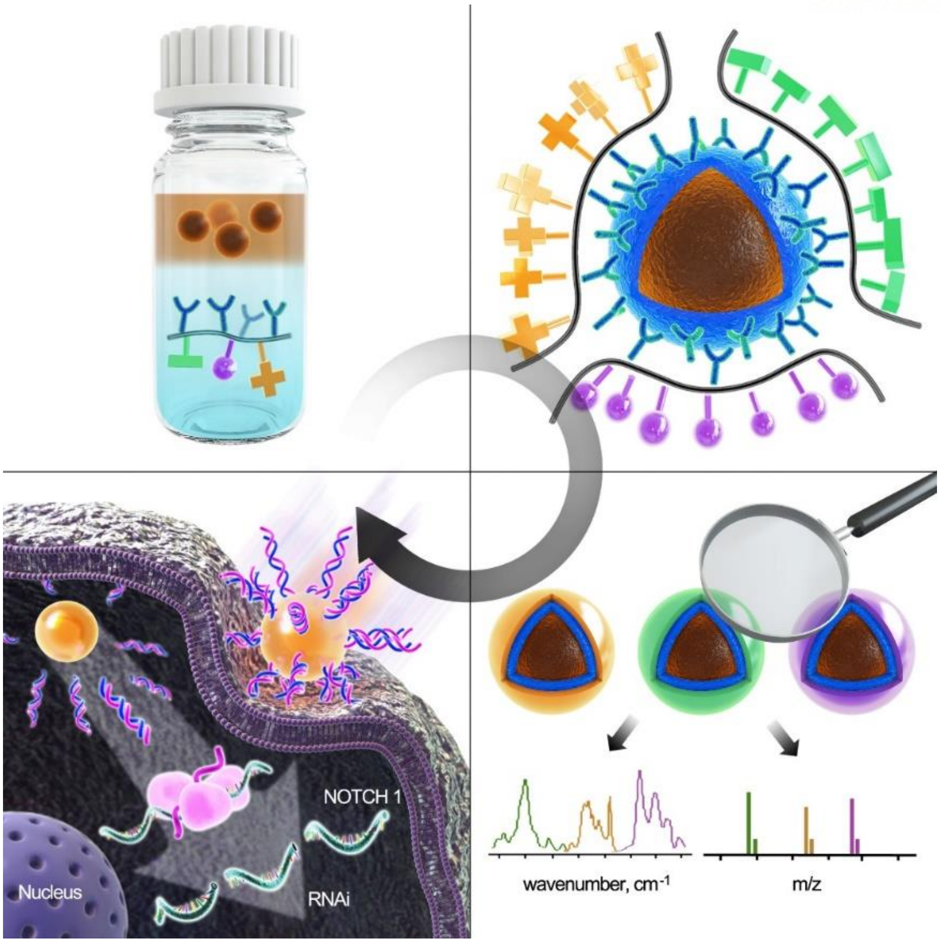

Figure 4.1. Our strategy for in-depth understanding of interactions between NPs and mammalian cells depends on the NP surface charge, brought about by well-designed surface chemistry; and chemical information based surface imaging analysis, and the NPs gene transfection efficiency.[42] Reproduced in part with permission from H.Na, H.H.Kim, and J.G.Son et al., Applied Surface Science, 2019, 483, 1069-1080, Copyright 2019 ELSEVIER.

4.2 Experimental section

4.2.1 Materials

Iron chloride hexahydrate (FeCl3·6H2O), sodium oleate, oleic acid, 1-octadecene, dopamine hydrochloride, sodium bicarbonate, methacrylate anhydride, N-[3-(dimethylamino)propyl]acrylamide, 2-acrylamido-2-methyl-1-propanesulfonic acid, poly(ethylene glycol) methyl ether acrylate (average Mn 480, PEG methyl ether acrylate), AIBN and $MgSO_4$ were purchased from Sigma-aldrich. Hydrochloric acid, ethylacetate, N,N-Dimethylformamide (DMF), tetrahydrofuran (THF), ethanol and diethylether were obtained from Samchun chemical, Korea. DMA and dibenzyl trithiocarbonate were synthesized from the literature.[29, 30]

4.2.2 Synthesis of iron oxide nanoparticles

The iron oxide NPs were synthesized using thermal decomposition of iron oleate precursors in organic solvent, as described in the current literature.[31] In a typical synthesis, iron oleate (1 mmol) and oleic acid (1 mmol) were dissolved in 5 g of 1-octadecene. The mixture was heated to 320 ^{o}C at a heating rate of 3.3 ^{o}C/min in an argon atmosphere. The resulting solution was cooled under inert conditions. The product was collected by centrifugation in an acetone and ethanol mixture.

4.2.3 Multidentate catechol based PEG ligand polymerization.

The polymer was synthesized via our previous reported method.[32] For the reaction, 0.05 mmol of DMA and 0.2 mmol of poly(ethylene glycol) methyl ether acrylate were dissolved in 400 µL of dry DMF; 0.013 mmol of dibenzyl trithiocarbonate and AIBN were added to the solution. The mixture was degassed by 4 freeze-pump-thaw cycles. The mixture was then sealed under vacuum using a torch and subsequently immersed in a 70 ^{o}C oil bath for 24 h. The final product was twice precipitated in diethyl ether and dried under vacuum at 40 ^{o}C. For synthesis of tertiary amine and sulfonic acid ligands, N-[3-(dimethylamino)propyl] acrylamide and 2-acrylamido-2-methyl-1-propanesulfonic acid were used instead of poly(ethylene glycol) methyl ether acrylate.

4.2.4 Typical ligand exchange of iron oxide nanoparticles

The 1 mg of iron oxide NPs dispersed into 100 µL of THF was added to a solution consisting of 10 mg polymer and 200 µL of ethanol, after which the mixture was stirred overnight. The product was then precipitated in hexane and dispersed in water. The excess ligands were removed using centrifugal filters (Milipore, Mw cut off=50kDa).

4.2.5 Instrumentation

PEG based polymer was measured by GPC (Agilent system) at 25 ºC using THF as eluting solvent. Molecular weight was calibrated using polystyrene MW standards. The obtained molecular weight (Mw) of PEG ligand was 8744 (PDI=1.17) and of Sulfonic acid based polymer was 3887 (PDI=1.32). Tertiary amine based polymer was measured by water GPC calibrated with polyethylene glycol MW standards. The obtained molecular weight (Mw) of tertiary amine ligand was 8860 (PDI=1.09).The morphologies and size analysis of the iron oxide NPs were investigated with transmission electron microscopy (TEM, JEOL, JEM-2100) which was operated at 200 kV. The average hydrodynamic si ze and distribution of the NPs in water were measured using dynamic light scattering (DLS, Nano ZS90, Malvern Instruments Ltd. Worcestershire, U.K.). All measurements were conducte d in disposable cuvette using a 4 mW laser operating at a wavelength of 633 nm at 25℃ an d the scattering angle was fixed at 90°. The surface charge (zeta potential) of the NPs in water were measured using electrophoretic light scattering (ELS, Nano ZS90, Malvern Instruments Ltd. Worcestershire, U.K.). All samples were prepared by diluting with deionized (DI) water. The operating temperature was kept constant at 25℃. ToF-SIMS spectra were obtained by using a TOF-SIMS V instrument (ION-TOF GmbH, Germany) with a 25-keV Bi_3^+ ion gun. The experiments were repeated three times but each measurement manifested different micropatterns due to uncontrolled self-aggregation of the NPs on the silicon wafer. However, we obtained the same conclusions regarding the ligand conjugated Fe_3O_4 NPs. For ToF-SIMS imaging, the primary ion gun was operated at 5 kHz with 0.16 pA (Bi_3^+) average current at the sample holder. A bunch pulse of 0.7 ns duration resulted in mass resolution (M/ΔM) higher than 8000 at 250 *m/z*. A 200 μm × 200 μm area was rastered by primary ions to obtain the spectra while maintaining the primary ion dose of 1×10^{12} ions/cm^2. The mass calibrations were internally performed by using the H^+, H_2^+, CH_3^+, $C_2H_3^+$ and $C_3H_5^+$ peaks for the positive ion spectra and H^-, C^-, CH^-, $C_2H^-$and C_4H^- for the negative ion spectra. All images presented in this work were taken in the positive and negative modes at 256 × 256 pixels with a spatial resolution of 1.5 μm. Fourier transform infrared (FT-IR) spectra of the NPs were taken with the Thermo Nexus 6700 FT-IR (Thermo-Nicolet, Inc.) equipped with an attenuated total reflectance (ATR) accessory (Smart Miracle, PIKE Tech.). A drop of NPs solution was placed on the ZnSe-ATR crystal and dried under vaccum (1×10^{-2} Torr) for 30 min. Mid-IR light was incident at 45° relative to the surface normal of the crystal under N_2. The reflected light was detected by a liquid N_2-cooled HgCdTe detector. 64 scans were averaged to yield a spectrum at 4 cm^{-1} resolution. FT-IR images were obtained with an iN10 MX (Thermo-Nicolet Inc.) equipped with a MCT-A detector cooled with liquid nitrogen. A 400 × 400 μm^2 area was analyzed by a 25 μm diameter focused IR beam at 20 μm steps.

4.2.6 Cell culture and cytotoxicity assay.

MDA MB 231 was cultured in Dulbecco's Modified Eagle's Medium (DMEM) containing 4.5 g/L D-glucose and supplemented with 10% FBS (fetal bovine serum), 100 units/mL penicillin and 100 μg/mL streptomycin at 37 ºC at 5% CO_2. To measure cell viability, MDA MB 231 cells were seeded at $1x10^4$ cells per well in a 96-well cell culture plate and incubated for 24 h at 37 ºC. The cells were then incubated with each NP at concentrations ranging from 0 to 300 μg/mL. MTT (3-(4,5-dimethylthiazol-2-yl)-2,5-diphenyltetrazolium bromide) reagent was used for quantification of the cell viability. After a 24 h incubation period with the NPs, the cells were treated with 20 μL of MTT stock solution (5 mg/mL). The cells were incubated for 3 h, and DMSO (200 μL) was added into each well to dissolve the insoluble formazan salt. The optical densities were measured at 560 nm and background absorbance at 670 nm (a reference wavelength) was subtracted using a microplate reader, SynergyH1 (Biotek, U.K.). The mean and standard deviation for triplicates were calculated. For the cytotoxicity test in Jurkat cells, CCK8 (cell counting kit 8, Dojindo) was used for quantification of cell viability. After 24 h incubation with the NPs, the cells were treated with 10 μL of CCK reagent. The cells were incubated for 3 h, and optical densities were then measured at 450 nm using a microplate reader, SynergyH1 (Biotek, U.K.). The mean and standard deviation for triplicates were calculated.

4.2.7 NOTCH1 knockdown in the Jurkat cell line

Jurkat cells were cultured in RPMI media supplemented with 10% FBS (fetal bovine serum), 100 units/mL penicillin and 100 μg/mL streptomycin at 37 ºC at 5% CO_2. The cells were seeded in a 6-well cell culture plate at a density of 5×10^5 cells per well, 24 h before transfection. After incubation for 24 h, the cells were treated with 50 nM siRNA targeting NOTCH1 complexed with positively charged Fe_3O_4 NP or Lipofectamine 2000^{TM} (Invitrogen, Carlsbad, CA). Following incubation for 48 h, the cells were collected and the total RNA was isolated using Trizol (Invitrogen, Carlsbad, CA) according to the manufacturer’s protocols. Real time PCR was performed using a Power SYBR green RNA-to-CT^{TM} 1-step kit (Applied Biosytems, California, USA). PCR primers for detection of human NOTCH1 (Primer #P320437) and GAPDH (Primer #P267613) were obtained from Bioneer, Inc. (Daejeon, Korea).

4.3 Result and discussion

To modify the surface of Fe_3O_4 NPs presenting different surface charges, ligands bearing a dopamine-containing block copolymer synthesized through RAFT polymerization were chosen (Figure 4.2 and 4.3). Each ligand contained the same polymer backbone and anchoring moiety (dopamine) with distinguishable side groups such as tertiary amines for positive (DOPA-Tertiary amine), PEG for neutral (DOPA-mPEG), and sulfonic acid for negative surface (DOPA-Sulfonic acid). Our ligand exchange approach employed fully synthesized polymers, and had the benefit of allowing facile control of the ratio of the anchoring groups to the side groups, which could previously only be obtained through the tedious process of post-modification after ligand exchange. Exchanging the ligands from oleic acid to a multi-dentate dopamine-based polymer converted the surface properties from hydrophobic to hydrophilic, resulting in stable mono-dispersions in aqueous phases, including water and buffers with various pH values and salt concentration in Figure 4.4a-c and Figure 4.5. Multidentate catechol and hydrophobic methyl group in polymer backbone endow resistance to approach of salt and detachment of ligands from surface of NPs. TEM images show that the oleic acid-coated and ligand-exchanged Fe_3O_4 NPs have monodisperse size distributions with an average size of 10.2 ± 0.53 nm (Figure 4.4a). DLS show an average hydrodynamic diameter of 22 nm for the tertiary amine-conjugated NPs (MNP@DOPA-Tertiary amine), 23 nm for the PEG-conjugated NPs (MNP@DOPA-mPEG), and 16 nm for the sulfonic acid-conjugated NPs (MNP@DOPA-Sulfonic acid). The Zeta potential values are +37 mV, −11 mV, and −31 mV, respectively (Figure 4.4b). The synthesized non-aggregated compact, stable and charge controlled surface of NPs enables to study elaborate effect of inorganic NPs in bio-application because of restriction of other variables except to charge.

To perform an in-depth surface- and free-ligand analysis for the charge-controlled Fe_3O_4 NPs, the ToF-SIMS technique was utilized for an examination of the molecular composition of conjugated and unconjugated ligands on the NPs because of its high atomic/molecular sensitivity and high spatial resolution. Further, ToF-SIMS was able to provide direct evidence for the presence of surface ligands on the NPs when the spatial distributions of the NP core ions and surface ligand ions were compared; these were measured from the micro-aggregated NPs sample surface. It can be assumed from the chemical structure of the ligand in Figure 4.2 that the dopamine region of the ligand is bound to the surface of the Fe_3O_4 NPs and that the other functional groups are exposed to the aqueous environment.[33] In Figure 4.6a-d, the bright red (R), green (G), and blue (B) areas indicate strong ionic distribution. By comparing the image patterns for Fe_3O_4-related core ions and fragment ions produced by the ligand, we can distinguish the ligands bound and unbound to the Fe_3O_4 NPs. Polymeric ligands

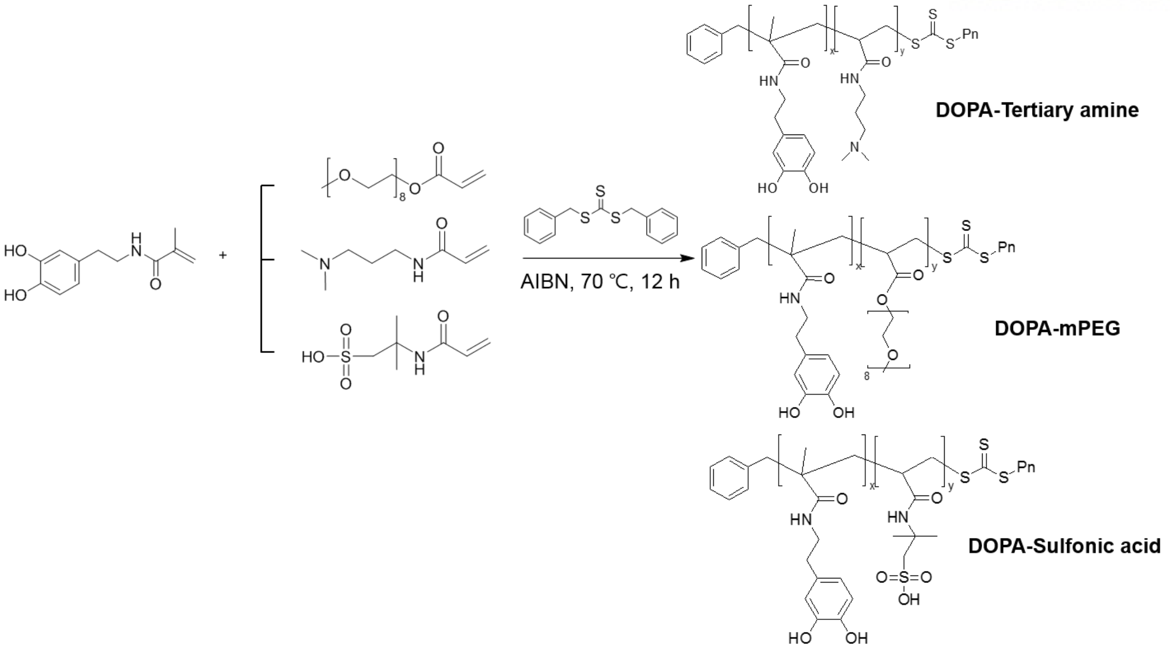

Figure 4.2. RAFT polymerization reaction for synthesis of ligands. For ligands possessing different surface charges, the polymer synthesis was designed by using two monomers, one as the common anchor (dopamine) and the other as the distinguishable functional group (tertiary amine for positive, PEG for neutral, and sulfonic acid for negative surface).[42] Reproduced in part with permission from H.Na, H.H.Kim, and J.G.Son et al., Applied Surface Science, 2019, 483, 1069-1080, Copyright 2019 ELSEVIER.

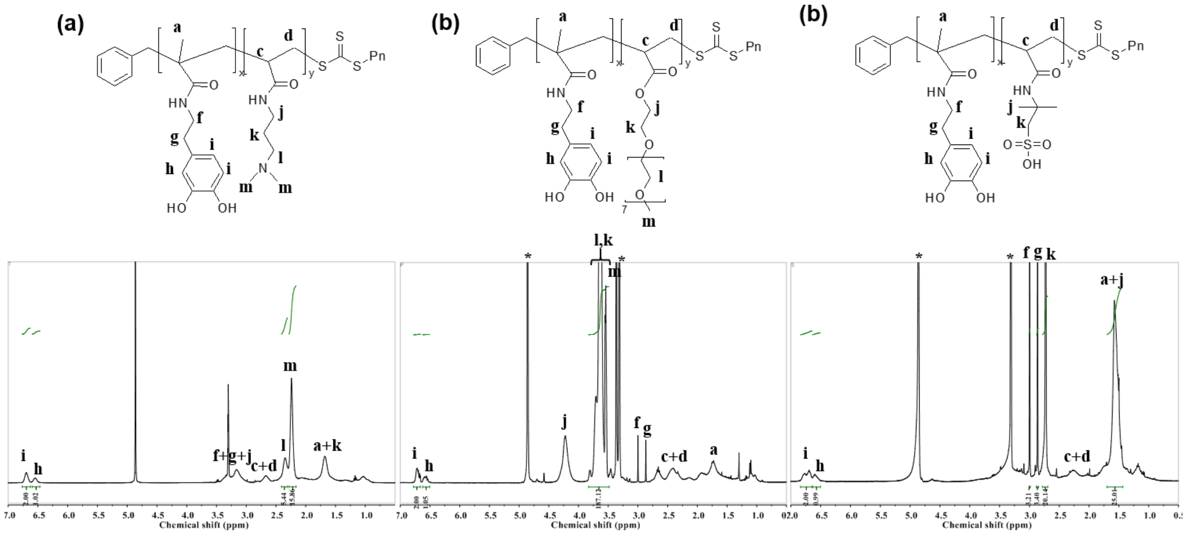

Figure 4.3. ^{1}H NMR spectrum of (a) DOPA-Tertiary amine, (b) DOPA-mPEG, and (c) DOPA-Sulfonic acid measured in MeOD.[42] Reproduced in part with permission from H.Na, H.H.Kim, and J.G.Son et al., Applied Surface Science, 2019, 483, 1069-1080, Copyright 2019 ELSEVIER.

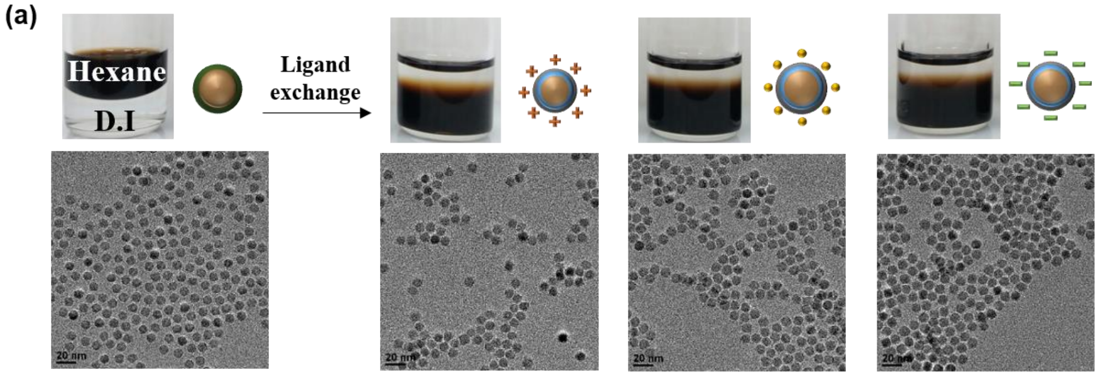

(b)

Surface ligand	DLS	Zeta-potential
Tertiary amine	22 nm	+37 mV
PEG	23 nm	-11 mV
Sulfonic acid	16 nm	-31 mV

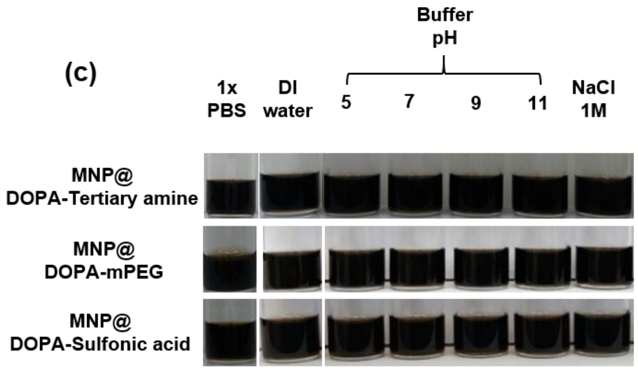

Figure 4.4. Characterization of Fe3O4 NPs. (a) TEM images of Fe3O4 NPs before and after ligand exchange with DOPA-Tertiary amine (positive), DOPA-mPEG (neutral), and DOPA-Sulfonic acid (negative). (b) DLS and zeta-potential of Fe3O4 NPs with different surface ligands (positive, neutral, and negative) (c) Images of ligand exchanged MNPs dispersed in various aqueous solutions. Results showed that surface modified Fe3O4 NPs were stable in various pH values and 1 M NaCl solution.[42] Reproduced in part with permission from H.Na, H.H.Kim, and J.G.Son et al., Applied Surface Science, 2019, 483, 1069-1080, Copyright 2019 ELSEVIER.

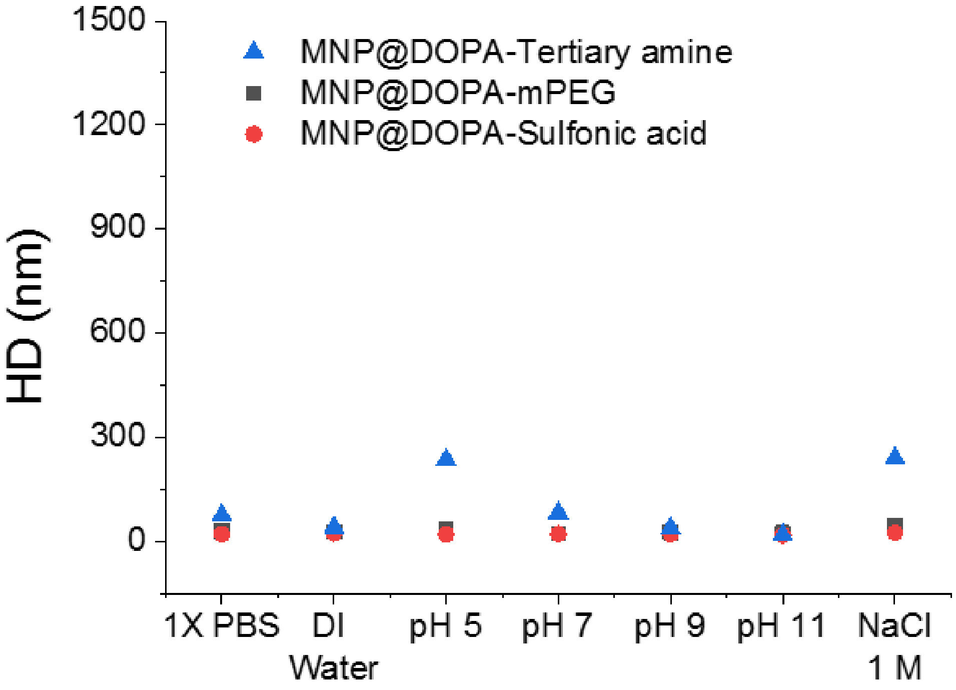

Figure 4.5. (A) DLS analysis to observe the stability of ligand exchanged MNPs in 1X PBS, DI water, buffer at pH ranging from 5 to 11 and in 1 M NaCl solution.[42] Reproduced in part with permission from H.Na, H.H.Kim, and J.G.Son et al., Applied Surface Science, 2019, 483, 1069-1080, Copyright 2019 ELSEVIER.

were used to not only reduce toxicity but also to control the surface charge state. In this work, DOPA-Tertiary amine, DOPA-mPEG, and DOPA-Sulfonic acid ligands were used to make positive, neutral, and negative Fe_3O_4 NPs, respectively. In the ToF-SIMS measurements, positive characteristic ion signals were generated from the tertiary amine and the PEG ligands, whereas negative characteristic ion signals were generated from the sulfonic acid ligands, as shown in Figure 4.7. Because the synthesized ligands have comparatively large molecular weights, they were barely detected as intact molecules in the ToF-SIMS spectra so that each polymer was characterized by their characteristic fragment ions. Characteristic fragment ions for each polymer and oleic acid ligand are listed in Figure 4.6e; their spectra are shown in Figure 4.7. The Fe_3O_4 NPs were analyzed at the same sample region in the positive and negative ion modes. Fe^+ and FeO_2^- (*m/z* 55.93 and 87.92) were observed for each NP type, and their spatial distributions correlated well in the ToF-SIMS images (Figure 4.6).

In Figure 4.6a, the $C_{18}H_{33}O_2^-$ (*m/z* 281.23) was detected as a characteristic peak of oleic acid ligands for the oleic-acid-coated Fe_3O_4 NPs and its spatial distribution was not precisely co-localized with the spatial distributions of Fe_3O_4-related core ions (Figure 4.6a), indicating that oleic acid exists not only on the surface of the Fe_3O_4 NPs but also in the solution as free ligands owing to incomplete ligand removal during the washing process. In the positively charged MNP@DOPA-Tertiary amine, the spatial distribution of the fragment ion of the tertiary amine ($C_6H_{13}N_2O^+$, *m/z* 129.10) also showed good correlation with those of the Fe_3O_4-related core ions (Fe^+ and FeO_2^-) (Figure 4.6b) due to the successful conjugation of the DOPA-Tertiary amine ligands and removal of the unconjugated ligands. In the neutral MNP@DOPA-mPEG, the spatial distribution of the PEG fragment ion ($C_5H_{11}O_2^+$, *m/z* 103.07) and those of the Fe_3O_4-related core ions (Fe^+ and FeO_2^-) correlated well, indicating that the neutral DOPA-mPEG ligand was bound to the Fe_3O_4 NPs surface (Figure 4.6c). Likewise, in the MNP@DOPA-Sulfonic acid, the spatial distribution of the sulfonic acid fragment ion ($C_7H_{12}NO_4S^-$, *m/z* 206.04) correlated well with those of the Fe^+ and FeO_2^- ions

(Figure 4.6d). However, when the Fe_3O_4 NPs were ligand exchanged by using the PEG polymer with no dopamine anchoring groups, the PEG-related ion distribution ($C_5H_{11}O_2^+$, *m/z* 103.07) was almost the reverse of the Fe^+ distribution (Figure 4.8).

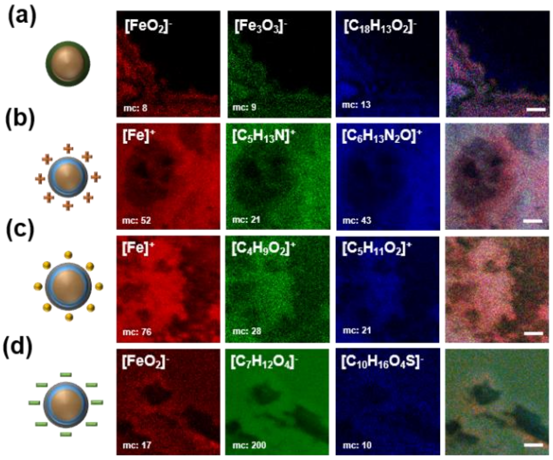

(e)

	Ion mass	Fragment ion	Assignment
Positive ion	55.93	Fe^+	Fe_3O_4 NPs
	87.10	$C_5H_{13}N^+$	Tertiary amine
	129.10	$C_6H_{13}N_2O^+$	Tertiary amine
	89.06	$C_4H_9O_2^+$	PEG
	103.07	$C_5H_{11}O_2^+$	PEG
Negative ion	87.92	FeO_2^-	Fe_3O_4 NPs
	215.77	$Fe_3O_3^-$	Fe_3O_4 NPs
	281.23	$C_{18}H_{33}O_2$	Oleic acid
	206.04	$C_7H_{12}NO_4S^-$	Sulfonic acid
	246.08	$C_{10}H_{16}NO_4S^-$	Sulfonic acid

Figure 4.6. (a) Oleic acid coated Fe_3O_4 NPs, (b) MNP@DOPA-Tertiary amine, (c) MNP@DOPA-mPEG, (d) MNP@DOPA-Sulfonic acid. Images show the distribution of selected ligands in micro-size pattern of Fe_3O_4 NPs. (mc = maximum counts in one pixel, scale bar = 50 μm). (e) Table of molecular weights, fragment ions and assigned ligands of ToF-SIMS secondary positive and negative ions obtained from ligand-conjugated Fe_3O_4 NPs.[42] Reproduced in part with permission from H.Na, H.H.Kim, and J.G.Son et al., Applied Surface Science, 2019, 483, 1069-1080, Copyright 2019 ELSEVIER.

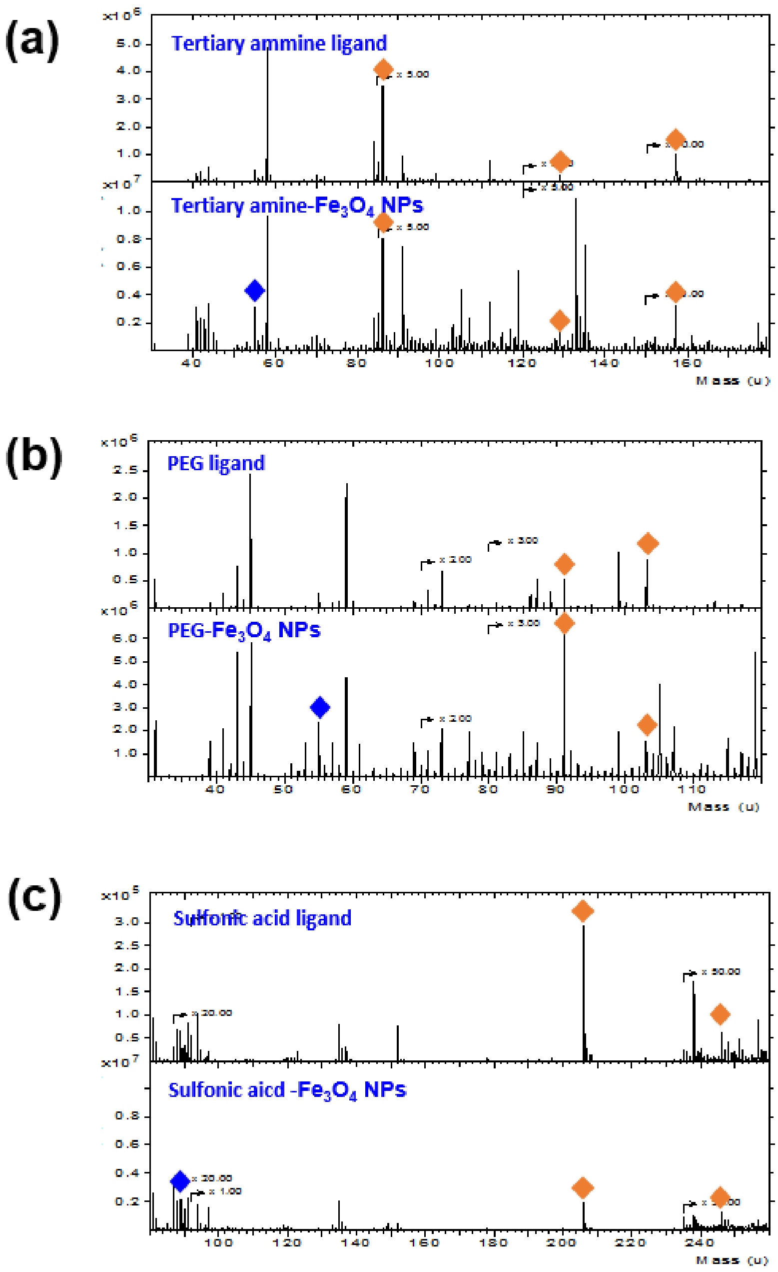

Figure 4.7. ToF-SIMS spectra of positive and negative ions related to Fe_3O_4 NPs and their ligands (a)-(c). The first layer shows free ligand and second layer represents ligand-conjugated Fe_3O_4 NPs; (a) tertiary amine, (b) PEG, and (c) sulfonic acid. Iron-related ions of Fe_3O_4 NPs ($[Fe]^+$ and $[FeO_2]^-$) are indicated by blue diamonds and fragment ions of polymer ligands for tertiary amine, PEG, and sulfonic acid are indicated by orange diamonds.[42] Reproduced in part with permission from H.Na, H.H.Kim, and J.G.Son et al., Applied surface science, 2019, 483, 1069-1080, Copyright 2019 ELSEVIER.

This may be clear evidence that the binding affinity of our ligand polymer (DOPA-Tertiary amine, DOPA-mPEG, and DOPA-Sulfonic acid) results from the dopamine anchoring groups. Based on these ToF-SIMS results, it is highly likely that the surface of the Fe_3O_4 NPs was modified by the synthesized ligands possessing different charges and that the free-ligand polymer remaining after the ligand exchange reactions was successfully removed. Since ToF-SIMS images showed good correlations between the spatial distributions of Fe_3O_4-related core ions and those of characteristic fragment ions of the charge-determining ligands, we were able identify the Fe_3O_4 NPs modified with different polymers. Next, a complementary study was conducted by using FT-IR microscopy imaging together with ToF-SIMS imaging to obtain the spatial distributions of the functional groups in each polymer ligand conjugated on each particle. The fabricated NPs surfaces were characterized by comparing the characteristic vibrational peak intensities and the Fe^+ distributions obtained from the same sample region. Initially, FT-IR spectra of tertiary amine, free PEG, and sulfonic acid ligands before being introduced to the NPs were obtained and assigned according to their characteristic vibrational modes, as summarized in Figure 4.9g. Subsequently, FT-IR spectroscopy measurements were conducted on the ligand-conjugated Fe_3O_4 NPs, and all samples presented similar characteristic peaks (Figure 4.10). The FT-IR peak assignments for the free ligands and ligand-coated Fe_3O_4 NPs are shown in Figure 4.9g. For example, the three kinds of polymer ligands have in common the dopamine moiety, which has characteristic peaks at around 1649–1645 cm^{-1} (C=O stretching mode, $\nu(C=O)$), 1548–1521 cm^{-1} (C–NH stretching mode, $\nu(C–NH)$), and 1470–1452 cm^{-1} (CH_2 bending mode, $\delta(CH_2)$). The distinguishable functional groups of each polymer present characteristic peaks. The asymmetric mode ($\nu_{as}(C–O–C)$) of PEG is presented at 1104 cm^{-1}; the C-N stretching mode ($\nu(C–N)$) of the tertiary amine is presented at 1257 cm^{-1}; and the asymmetric ($\nu_{as}(SO_2)$), stretching ($\nu(SO_3)$), and symmetric ($\nu_s(SO3)$) modes of the sulfonic acid are presented at 1212, 1182, and 1039 cm^{-1}, respectively (Figure 4.9g and Figure 4.10).

Since IR spectroscopy is unable to determine the spatial distribution of the candidate ligands, IR microscopy was utilized to analyze all of the samples. The characteristic peaks for each polymer were reconstructed into FT-IR microscopy images, shown in Figure 4.9a-c, and the regions abundant in polymer ligands were identified. The presence of Fe_3O_4 NPs was verified for the same region that was used for the complementary IR analysis, and the distributions of the Fe_3O_4-related ions were determined by using ToF-SIMS image analysis (Figure 4.9d-f). FT-IR images of the surface ligands at 1103, 1205, and 1184 cm^{-1}, which correspond to the C–O–C asymmetric stretching ($\nu_{as}(C–O–C)$), C-N stretching ($\nu(C–N)$), and SO_3 stretching ($\nu(SO_3)$) modes, show that each ligand is bound on the surface of the Fe_3O_4 NPs (Figure 4.9a-c). Furthermore, the signal distribution of the anchoring group ($\nu(C=O)$) at around 1649–1625 cm^{-1} and those of the surface ligands ($\nu_{as}(C–O–C)$, $\nu(C–N)$, and $\nu(SO_3)$) in the FT-IR images correlate well (Figure 4.9a-c), indicating that the surface ligands are

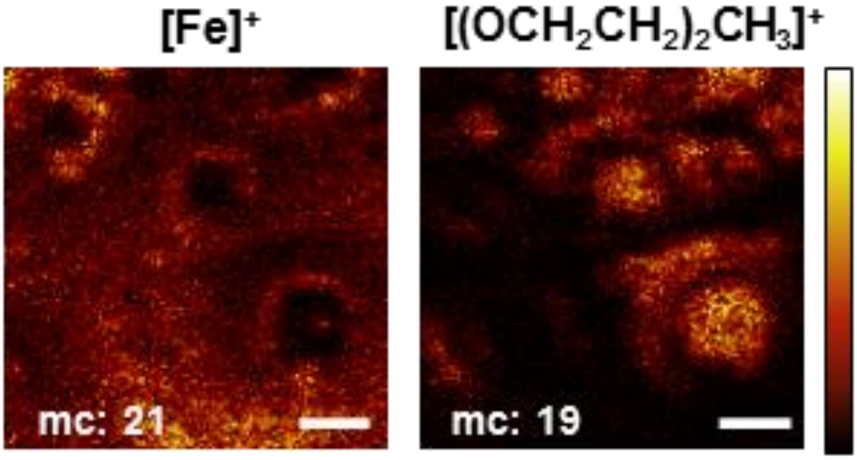

Figure 4.8. ToF-SIMS images of positive ions from PEG treated Fe_3O_4 NPs without an anchoring group. This image shows the distribution of Fe_3O_4 NPs- and PEG-related fragment ion in an area with micro-sized aggregations patterns. The spatial distribution of the $[(OCH_2CH_2)_2CH_3]^+$ ion was not overlapped with the Fe^+ distribution, indicating that the PEG ligands were not bound to the Fe_3O_4 NP surface.[42] Reproduced in part with permission from H.Na, H.H.Kim, and J.G.Son et al., Applied Surface Science, 2019, 483, 1069-1080, Copyright 2019 ELSEVIER.

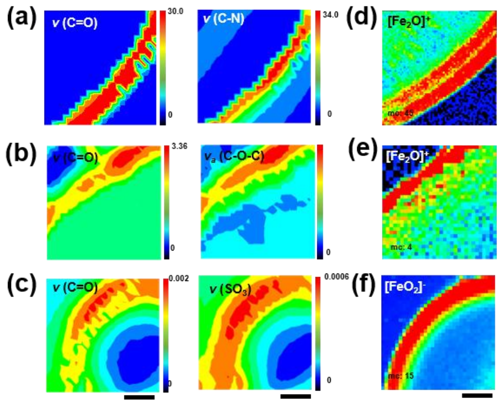

(g)

	Ligands		Ligand-conjugated NPs	
	Wavenumber (cm^{-1})	Assignment	Wavenumber (cm^{-1})	Assignment
Anchoring group branch	3435-3276 cm^{-1}	ν(OH)	3384-3309 cm^{-1}	ν(OH)
	1649-1645 cm^{-1}	ν(C=O)	1649-1625 cm^{-1}	ν(C=O)
	1548-1521 cm^{-1}	ν(C-NH)	1549-1539 cm^{-1}	ν(C-NH)
	1470-1452 cm^{-1}	δ (CH$_2$)	1470-1443 cm^{-1}	δ (CH$_2$)
Tertiary amine	1257 cm^{-1}	ν(C-N)	1205 cm^{-1}	ν(C-N)
PEG	1732 cm^{-1}	ν(C=O)	1729 cm^{-1}	ν(C=O)
	1104 cm^{-1}	ν$_{as}$(C-O-C)	1103 cm^{-1}	ν$_{as}$(C-O-C)
Sulfonic acid	1212 cm^{-1}	ν$_{as}$(SO$_2$)	1208 cm^{-1}	ν$_{as}$(SO$_2$)
	1182 cm^{-1}	ν(SO$_3$)	1184 cm^{-1}	ν(SO$_3$)
	1039 cm^{-1}	ν$_s$(SO$_3$)	1040 cm^{-1}	ν$_s$(SO$_3$)

Figure 4.9. FT-IR images of (a) MNP@DOPA-Tertiary amine, (b) MNP@DOPA-mPEG, and (c) MNP@DOPA-Sulfonic acid. FT-IR images obtained from related peaks of ligand-conjugated Fe3O4 NPs for anchoring group (ν(C=O)) and characteristic functional groups ((a) tertiary amine ligand (ν(C–N)), (b) PEG ligand (νas(C–O–C)), and (c) sulfonic acid ligand (ν(SO3))). ToF-SIMS images (d-f) show the [Fe2O]+ ion distributions from the same area that the FT-IR images were measured. (scale bar = 100 μm). (g) Assigned functional group of FT-IR vibrational modes of free ligands and ligand-conjugated NPs.[42] Reproduced in part with permission from H.Na, H.H.Kim, and J.G.Son et al., Applied Surface Science, 2019, 483, 1069-1080, Copyright 2019 ELSEVIER.

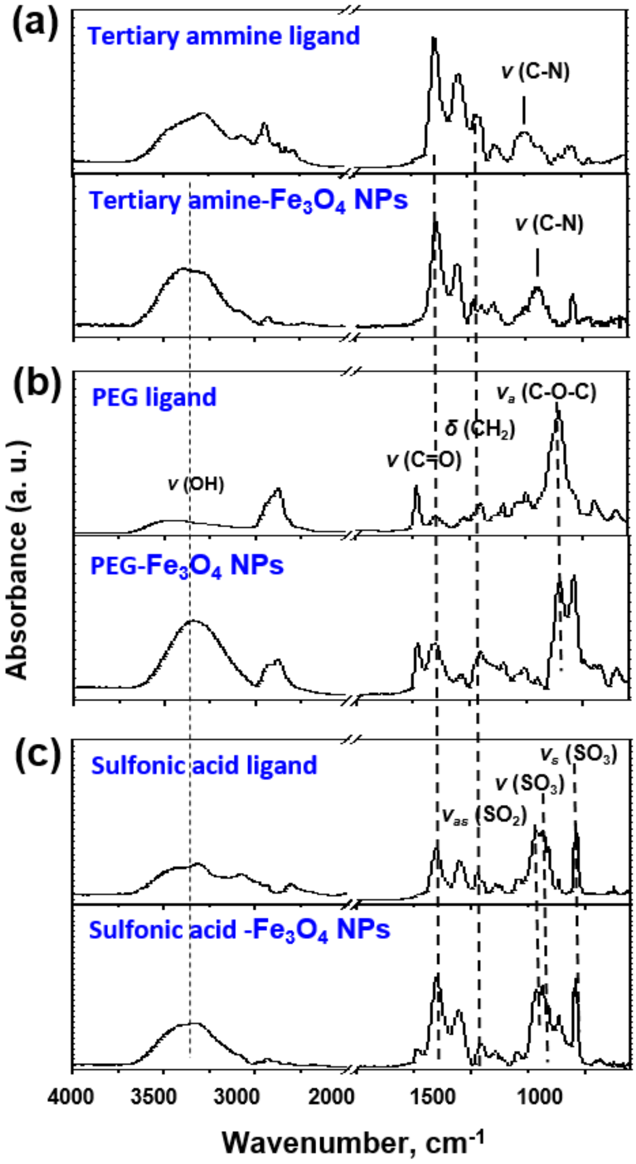

Figure 4.10. FT-IR spectra of (a) positively charged Fe_3O_4 NPs, (b) neutral Fe_3O_4 NPs, and (c) negatively charged Fe_3O_4 NPs. The first layer shows free polymer ligands and the second layer represents (a) tertiary amine, (b) PEG, and (c) sulfonic acid-coated Fe_3O_4 NPs, respectively.[42] Reproduced in part with permission from H.Na, H.H.Kim, and J.G.Son et al., Applied surface science, 2019, 483, 1069-1080, Copyright 2019 ELSEVIER.

bound to the Fe_3O_4 NPs. The spatial distributions of polymer ligands possessing different charge states and the Fe_3O_4-related ion distributions from each Fe_3O_4 NPs were compared using complementary FT-IR microscopy and ToF-SIMS imaging analysis, respectively. A successful surface modification was confirmed by the good correlation between the FT-IR signal distributions of the ligand-conjugated NPs and ToF-SIMS signal distributions of the Fe_3O_4-related ions. Using this analytical approach, we were able to characterize the surface of the Fe_3O_4 NPs after ligand exchange.

This method can confirm not only the presence of organic molecules on inorganic NPs, but also the absence of residual unbound polymer after purification.

We then performed cytotoxicity tests by incubating the different NPs for 24 h with the MDA MB 231 cell line to investigate the biocompatibility of our well-characterized Fe_3O_4 NPs.[34-36] It is widely accepted that the surface functionality of NPs plays a critical role in cyto-compatibility by affecting the interactions with cellular membranes.

In this regard, our surface-modified and fully characterized NPs is a promising system to elucidate the relationship between surface functionality (particularly, surface charge state) and cytotoxicity. As shown in Figure 4.11d, these three types of NPs do not exhibit significant cytotoxicity for the concentration range (0–300 µg/mL) in general use. However, the positively charged Fe_3O_4 NPs (i.e., MNP@DOPA-Tertiary amine) induced slight decreases in cell viability at high concentrations (150 and 300 µg/mL).

Surface modification, then, affects the cytotoxicity of the NPs even though the composition of their cores is identical to the Fe_3O_4. In addition, the intracellular Fe levels after incubation of the NPs with MDA MB 231 cells at various concentrations followed by extensive washing were quantified using ICP-MS analysis in order to investigate the influence of surface functionality on cellular uptake. Interestingly, a remarkably high quantity of Fe was detected in the cells treated with MNP@DOPA-Tertiary amine, indicating that a positive surface promotes sufficient interaction with cells and efficient intracellular uptake (Figure 4.11e). Moreover, PEGylated Fe_3O_4 NPs (i.e., MNP@DOPA-mPEG) were barely internalized into the cells, indicating negligible interaction with the cell membrane, which is in accordance with a previous report.[37] This suggests that in biomedical applications, surface properties of the NPs need to be taken into account for efficient circulation in the blood and cellular uptake.

For direct visualization of the intracellular uptake properties of each Fe_3O_4 NP, TEM analysis of cells was performed after treatment with NPs at 30 µg/mL. The Bio-TEM images in Figure 4.12 confirm the markedly different cellular uptake efficiencies. They also confirm that the high concentration of Fe for the MNP@DOPA-Tertiary amine as revealed by ICP-MS analysis is due to intracellular uptake rather than binding to the cellular membrane. Thus, surface functionality is an important factor for cell-NP interactions, and surfaces should be designed according to their applications.

Based on their remarkable cellular uptake efficiency in MDA MB 231, the cellular interaction of positively charged Fe_3O_4 NPs with suspension-type cells was also investigated. In our ICP-MS analysis, a high quantity of Fe was found in suspension Jurkat human leukemic T cells, whose transfection is known to be difficult, after treatment with positively charged Fe_3O_4 NPs.[38] (Figure 4.13) Furthermore, TEM images show the intracellular existence of Fe_3O_4 NPs in Jurkat cells. The red areas

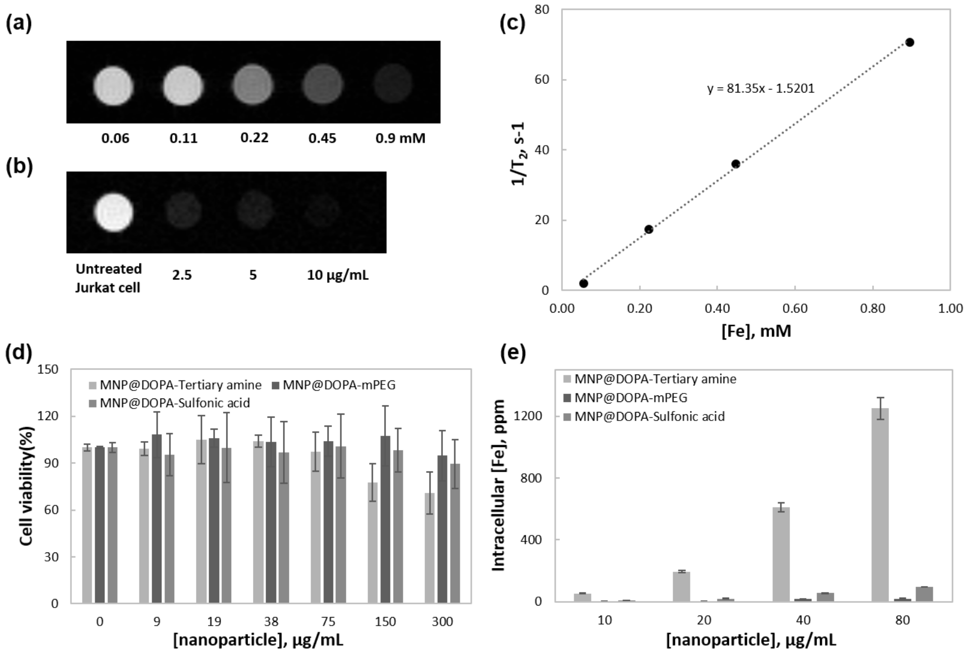

Figure 4.11. MR imaging and intracellular behavior of surface modified NPs. (a) T_2 weighted MR image of MNP@DOPA-Tertiary amine at various concentrations of iron. (b) T_2 weighted MR image of MNP@DOPA-Tertiary amine treated Jurkat cells (c) Relaxivity of MNP@DOPA-Tertiary amine. (d) Cytotoxicity for each particle with different surface functional groups using MTT assay; cytotoxicity was investigated for MNP@DOPA-Tertiary amine, MNP@DOPA-mPEG, and MNP@DOPA-Sulfonic acid on MDA MB cell line after 24 h incubation. The results showed that none of these NPs induced significant toxicity on cells up to 75 μg/mL concentration. Each data point represents the mean ± S.D. of the three experiments. (e) Quantification of intracellular Fe concentration through ICP-MS after treatment of each particle revealed that MNP@DOPA-Tertiary amine was highly efficient for intracellular uptake, unlike MNP@DOPA-mPEG and MNP@DOPA-Sulfonic acid.[42] Reproduced in part with permission from H.Na, H.H.Kim, and J.G.Son et al., Applied Surface Science, 2019, 483, 1069-1080, Copyright 2019 ELSEVIER.

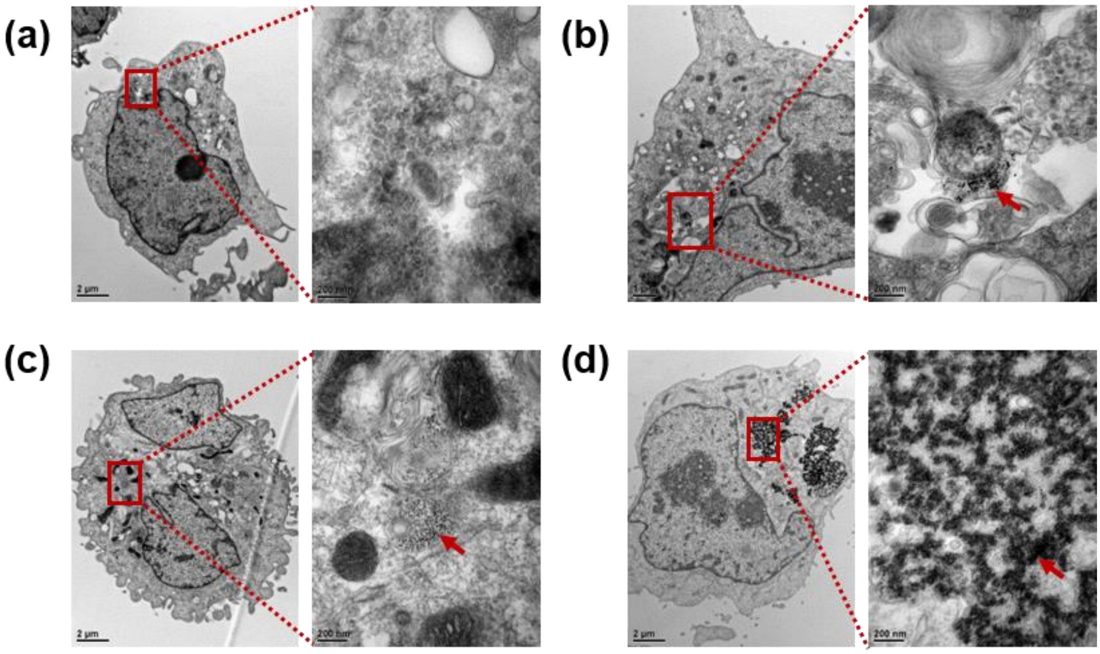

Figure 4.12. Bio-TEM images of MDA MB 231 cells in the absence (a) and presence of MNP@DOPA-Tertiary amine (b), MNP@DOPA-mPEG (c), and MNP@DOPA-Sulfonic acid (d). The presence of NPs can be clearly observed inside the cells due to the influence of the surface functionality, depending on the degree of cellular uptake.[42] Reproduced in part with permission from H.Na, H.H.Kim, and J.G.Son et al., Applied Surface Science, 2019, 483, 1069-1080, Copyright 2019 ELSEVIER.

in Figure 4.14a indicate the Fe_3O_4 NPs in the interior of the cells. Furthermore, magnetic resonance (MR) images of the NP-treated Jurkat cells in Figure 4.14b also point to the efficient intracellular uptake of positively charged NPs, as represented by the dark contrast images in a concentration dependent manner. These *in vitro* MR images (Figure 4.14a-b) show that our surface-modified NPs show a great deal of potential as efficient contrast agents.

Based on the efficient cellular uptake capability and their positive surface charges, the feasibility of MNP@DOPA-Tertiary amine as a gene transfection agent was examined in the Jurkat cell line. NOTCH1 was chosen as a target gene because NOTCH signaling has been extensively studied as a therapeutic target owing to its role as an oncogenic trigger in T-cell leukemia.[39,40] After formation of an NP-siRNA targeting NOTCH1 (siNOTCH1) complex by simple mixing, it was introduced to the Jurkat cells. Figure 4.14b shows that MNP@DOPA-Tertiary amine induced a considerable down-regulation of NOTCH1 mRNA expression with a higher efficiency (75.4%) than that of a commercially available transfection agent (49%). Although it is not easy to transfect suspension-type cell lines without magnetic assistance,[14, 41] our MNP@DOPA-Tertiary amine induced the efficient knockdown of target mRNA without significant toxicity to the NP itself (Figure 4.15) and hence showed the importance of surface modification. In short, we have found that a well-designed surface can be instrumental in interactions with the biological systems and uptake, whereas the core particle plays an important role as an imaging or therapeutic agent based on its shape and composition.

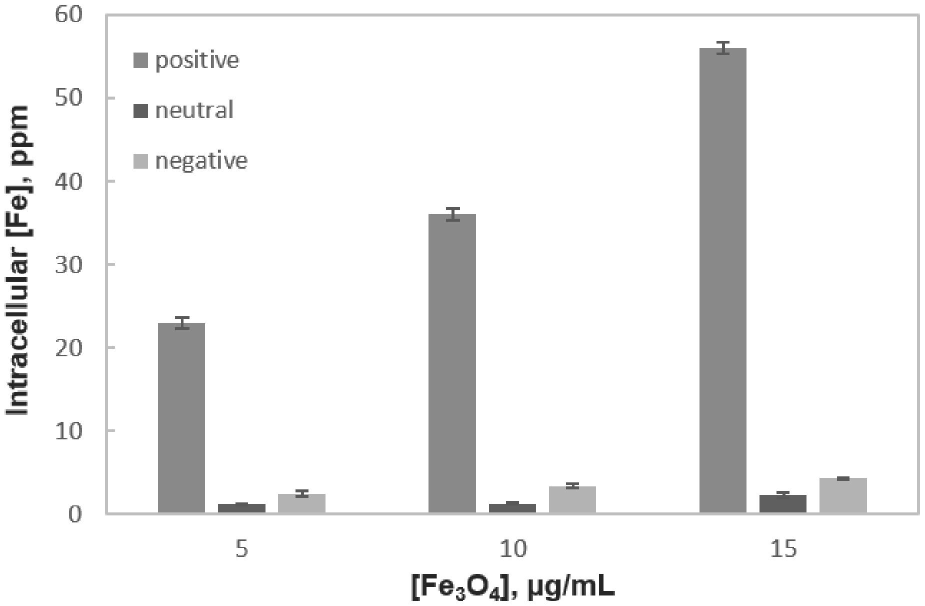

Figure 4.13. Quantification of intracellular Fe concentration through ICP-MS after treatment of each particle into the Jurkat cell line.[42] Reproduced in part with permission from H.Na, H.H.Kim, and J.G.Son et al., Applied Surface Science, 2019, 483, 1069-1080, Copyright 2019 ELSEVIER.

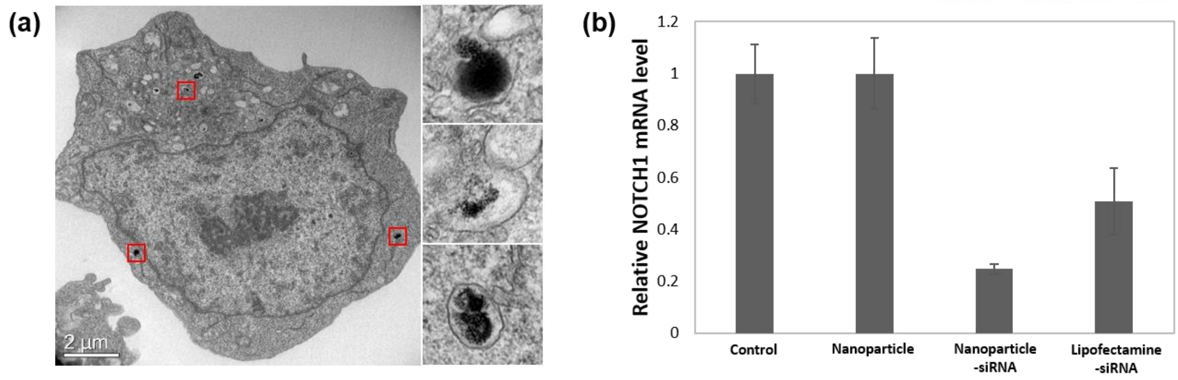

Figure 4.14. Biological interactions of suspension type Jurkat cells with positively charged Fe3O4 NPs. (a) Bio-TEM images of Jurkat cell after treatment with MNP@DOPA-Tertiary amine at 10 μg/mL concentration. NPs were clearly found inside the cell. (b) Gene knockdown efficiency of MNP@DOPA-Tertiary amine for NOTCH1; NP-siRNA targeting NOTCH1 complex induced down regulation of target mRNA up to 75% measured by real-time PCR ($n = 3$). *vs control, $P < 0.001$. Our results showed a more efficient target gene knockdown of MNP@DOPA-Tertiary amine compared to commercial transfection agent without magnetic assistance.[42] Reproduced in part with permission from H.Na, H.H.Kim, and J.G.Son et al., Applied Surface Science, 2019, 483, 1069-1080, Copyright 2019 ELSEVIER.

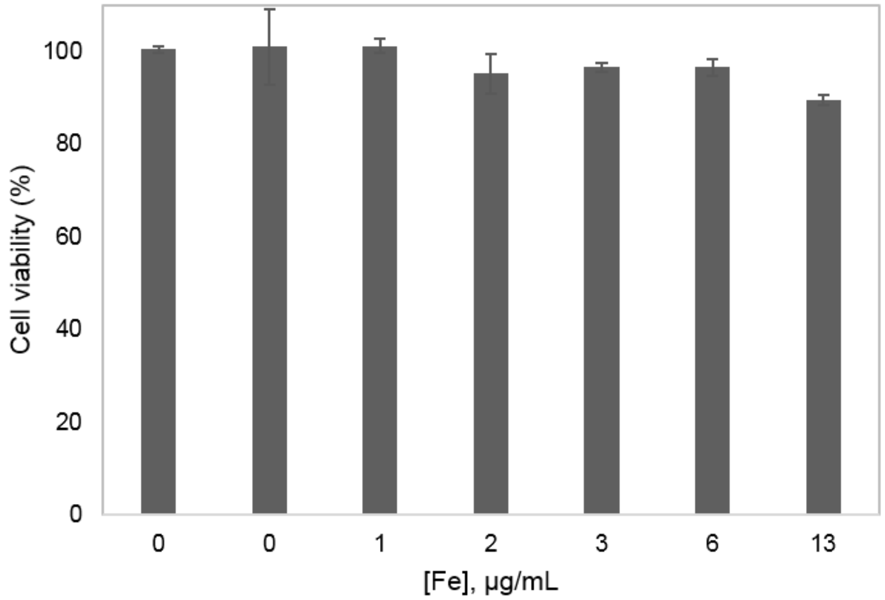

Figure 4.15. Cytotoxicity for positively charged Fe_3O_4 NPs in the Jurkat cell line, performed using CCK8 (cell counting kit 8) assay.[42] Reproduced in part with permission from H.Na, H.H.Kim, and J.G.Son et al., Applied surface science, 2019, 483, 1069-1080, Copyright 2019 ELSEVIER.

4.4 Conclusion

A unique modification strategy for surface-modified Fe_3O_4 NPs and tools for their precise surface characterization have been demonstrated. Through ligand exchange on Fe_3O_4 NPs using a fully synthesized polymer, NPs containing different surface charges were successfully obtained. In addition, the complementary use of ToF-SIMS imaging and FT-IR microscopy imaging provided direct information regarding the modified NPs surface. Based on the well-designed surface modification and direct surface characterization of the Fe_3O_4 NPs, their interaction with live cells depending on their surface charge was investigated, and surface charge was found to greatly influence cellular uptake efficiency. In the case of positively charged Fe_3O_4 NPs, large amounts of NPs were internalized in both adherent and suspension cell lines. Although transfection in suspension cells is difficult, it was efficiently achieved using the Fe_3O_4 NPs modified with a polymer containing amine moieties, which was prepared through RAFT polymerization of anchoring and functional monomers. By thorough investigation of the synthesis, characterization, and application of these NPs, it was proved that a well-designed surface can play a key role in both their interactions with biological systems and their uptake, whereas the core particle is important for its function as an imaging or therapeutic agent based on its shape and composition.

4.5 References

1. S.M. Ansari, R.D. Bhor, K.R. Pai, D. Sen, S. Mazumder, K. Ghosh, Y.D. Kolekar, C.V. Ramana, Cobalt nanoparticles for biomedical applications: Facile synthesis, physiochemical characterization, cytotoxicity behavior and biocompatibility, *Appl. Surf. Sci.* **2017**, 414, 171-187.

2. R. Mout, D.F. Moyano, S. Rana, V.M. Rotello, Surface functionalization of nanoparticles for nanomedicine, *Chem. Soc. Rev.* **2012**, 41, 2539-2544.

3. C. He, Y. Hu, L. Yin, C. Tang, C. Yin, Effects of particle size and surface charge on cellular uptake and biodistribution of polymeric nanoparticles, *Biomaterials* **2010**, 31, 3657-3666.

4. D.D. Herea, H. Chiriac, N. Lupu, M. Grigoras, G. Stoian, B.A. Stoica, T. Petreus, Study on iron oxide nanoparticles coated with glucose-derived polymers for biomedical applications, *Appl. Surf. Sci.* **2015**, 352, 117-125.

5. T.N. Le Thi, T.H. Nguyen, D.Q. Hoang, T.V. Tran, N.T. Nguyen, D.H. Nguyen, Development of new magnetic nanoparticles: Oligochitosan obtained by γ-rays and –coated Fe3O4 nanoparticles, *Appl. Surf. Sci.* **2017**, 422, 863-868.

6. R. Hao, R. Xing, Z. Xu, Y. Hou, S. Gao, S. Sun, Synthesis, Functionalization, and Biomedical Applications of Multifunctional Magnetic Nanoparticles, *Adv. Mater.* **2010**, 22, 2729-2742.

7. P.I.P. Soares, C.A.T. Laia, A. Carvalho, L.C.J. Pereira, J.T. Coutinho, I.M.M. Ferreira, C.M.M. Novo, J.P. Borges, Iron oxide nanoparticles stabilized with a bilayer of oleic acid for magnetic hyperthermia and MRI applications, *Appl. Surf. Sci.* **2016**, 383, 240-247.

8. E. Blanco, H. Shen, M. Ferrari, Principles of nanoparticle design for overcoming biological barriers to drug delivery, *Nat. Biotechnol.* **2015**, 33, 941.

9. N.M. Schaeublin, L.K. Braydich-Stolle, A.M. Schrand, J.M. Miller, J. Hutchison, J.J. Schlager, S.M. Hussain, Surface charge of gold nanoparticles mediates mechanism of toxicity, *Nanoscale* **2011**, 3, 410-420.

10. C.M. Goodman, C.D. McCusker, T. Yilmaz, V.M. Rotello, Toxicity of Gold Nanoparticles Functionalized with Cationic and Anionic Side Chains, *Bioconjugate Chem.* **2004**, 15, 897-900.

11. K. Chen, J. Xu, J.C. Luft, S. Tian, J.S. Raval, J.M. DeSimone, Design of Asymmetric Particles Containing a Charged Interior and a Neutral Surface Charge: Comparative Study on in Vivo Circulation of Polyelectrolyte Microgels, *J. Am. Chem. Soc.* **2014**, 136, 9947-9952.

12. A. Asati, S. Santra, C. Kaittanis, J.M. Perez, Surface-Charge-Dependent Cell Localization and Cytotoxicity of Cerium Oxide Nanoparticles, *ACS Nano* **2010**, 4, 5321-5331.

13. D. Ling, M.J. Hackett, T. Hyeon, Surface ligands in synthesis, modification, assembly and biomedical applications of nanoparticles, *Nano Today* **2014**, 9, 457-477.

14. M. Mahmoudi, H. Hofmann, B. Rothen-Rutishauser, A. Petri-Fink, Assessing the In Vitro and In Vivo Toxicity of Superparamagnetic Iron Oxide Nanoparticles, *Chem. Rev.* **2012**, 122, 2323-2338.

15. P.S. Ghosh, C.-K. Kim, G. Han, N.S. Forbes, V.M. Rotello, Efficient Gene Delivery Vectors by Tuning the Surface Charge Density of Amino Acid-Functionalized Gold Nanoparticles, *ACS Nano* **2008**, 2, 2213-2218.

16. J. Dobson, Gene therapy progress and prospects: magnetic nanoparticle-based gene delivery, *Gene Therapy* **2006**, 13, 283.

17. M. Babaei, H. Eshghi, K. Abnous, M. Rahimizadeh, M. Ramezani, Promising gene delivery system based on polyethylenimine-modified silica nanoparticles, Cancer *Gene Therapy* **2017**, 24, 156.

18. Y. Kapilov-Buchman, E. Lellouche, S. Michaeli, J.-P. Lellouche, Unique Surface Modification of Silica Nanoparticles with Polyethylenimine (PEI) for siRNA Delivery Using Cerium Cation Coordination Chemistry, *Bioconjugate Chem.* **2015**, 26, 880-889.

19. S. Guo, Y. Huang, Q. Jiang, Y. Sun, L. Deng, Z. Liang, Q. Du, J. Xing, Y. Zhao, P.C. Wang, A. Dong, X.-J. Liang, Enhanced Gene Delivery and siRNA Silencing by Gold Nanoparticles Coated with Charge-Reversal Polyelectrolyte, *ACS Nano* **2010**, 4, 5505-5511.

20. B.R. McNaughton, J.J. Cronican, D.B. Thompson, D.R. Liu, Mammalian cell penetration, siRNA transfection, and DNA transfection by supercharged proteins, *Proc. Natl. Acad. Sci. U. S. A.* **2009**, 106, 6111-6116.

21. Y. Xu, Y. Qin, S. Palchoudhury, Y. Bao, Water-Soluble Iron Oxide Nanoparticles with High Stability and Selective Surface Functionality, *Langmuir* **2011**, 27, 8990-8997.

22. M. Sara, D. Carmelo, M.F. Anna, P. Alessandra, P. Alessandro, Colloidal stability of iron oxide nanocrystals coated with a PEG-based tetra-catechol surfactant, *Nanotechnology* **2013**, 24, 105702.

23. L. Ma, C. Tu, P. Le, S. Chitoor, S.J. Lim, M.U. Zahid, K.W. Teng, P. Ge, P.R. Selvin, A.M. Smith, Multidentate Polymer Coatings for Compact and Homogeneous Quantum Dots with Efficient Bioconjugation, *J. Am. Chem. Soc.* **2016**, 138, 3382-3394.

24. H.-T. Song, J.-s. Choi, Y.-M. Huh, S. Kim, Y.-w. Jun, J.-S. Suh, J. Cheon, Surface Modulation of Magnetic Nanocrystals in the Development of Highly Efficient Magnetic Resonance Probes for

Intracellular Labeling, *J. Am. Chem. Soc.* **2005**, 127, 9992-9993.

25. R.N.S. Sodhi, Time-of-flight secondary ion mass spectrometry (TOF-SIMS):—versatility in chemical and imaging surface analysis, *Analyst* **2004**, 129, 483-487.

26. Y.-P. Kim, H.K. Shon, S.K. Shin, T.G. Lee, Probing nanoparticles and nanoparticle-conjugated biomolecules using time-of-flight secondary ion mass spectrometry, *Mass Spectrom. Rev.* **2015**, 34, 237-247.

27. J.G. Son, E. Choi, Y. Piao, S.W. Han, T.G. Lee, Probing organic ligands and their binding schemes on nanocrystals by mass spectrometric and FT-IR spectroscopic imaging, *Nanoscale* **2016**, 8, 4573-4578.

28. W. He, M.J. Bennett, L. Luistro, D. Carvajal, T. Nevins, M. Smith, G. Tyagi, J. Cai, X. Wei, T.-A. Lin, D.C. Heimbrook, K. Packman, J.F. Boylan, Discovery of siRNA Lipid Nanoparticles to Transfect Suspension Leukemia Cells and Provide In Vivo Delivery Capability, *Molecular Therapy* **2014**, 22, 359-370.

29. N. Aoyagi, T. Endo, Functional RAFT agents for radical-controlled polymerization: Quantitative synthesis of trithiocarbonates containing functional groups as RAFT agents using equivalent amount of CS2, *J. Polym. Sci., Part A: Polym. Chem.* **2009**, 47, 3702-3709.

30. H. Lee, B.P. Lee, P.B. Messersmith, A reversible wet/dry adhesive inspired by mussels and geckos, *Nature* **2007**, 448, 338-341.

31. J. Park, K. An, Y. Hwang, J.-G. Park, H.-J. Noh, J.-Y. Kim, J.-H. Park, N.-M. Hwang, T. Hyeon, Ultra-large-scale syntheses of monodisperse nanocrystals, *Nat. Mater.* **2004**, 3, 891-895.

32. N.K. Kwon, H. Kim, I.K. Han, T.J. Shin, H.-W. Lee, J. Park, S.Y. Kim, Enhanced Mechanical Properties of Polymer Nanocomposites Using Dopamine-Modified Polymers at Nanoparticle Surfaces in Very Low Molecular Weight Polymers, *ACS Macro Lett.* **2018**, 7, 962-967.

33. M. Mazur, A. Barras, V. Kuncser, A. Galatanu, V. Zaitzev, K.V. Turcheniuk, P. Woisel, J. Lyskawa, W. Laure, A. Siriwardena, R. Boukherroub, S. Szunerits, Iron oxide magnetic nanoparticles with versatile surface functions based on dopamine anchors, *Nanoscale* **2013**, 5, 2692-2702.

34. S.T. Kim, K. Saha, C. Kim, V.M. Rotello, The Role of Surface Functionality in Determining Nanoparticle Cytotoxicity, *Acc. Chem. Res.* **2013**, 46, 681-691.

35. A. Verma, F. Stellacci, Effect of Surface Properties on Nanoparticle–Cell Interactions, *Small* **2010**, 6, 12-21.

36. C.A. Fromen, T.B. Rahhal, G.R. Robbins, M.P. Kai, T.W. Shen, J.C. Luft, J.M. DeSimone,

Nanoparticle surface charge impacts distribution, uptake and lymph node trafficking by pulmonary antigen-presenting cells, *Nanomedicine: Nanotechnology, Biology and Medicine* **2016**, 12, 677-687.

37. R. Lee, D.h. Jo, S.J. Chung, H.-K. Na, J.H. Kim, T.G. Lee, Real-time and label-free monitoring of nanoparticle cellular uptake using capacitance-based assays, *Sci. Rep.* **2016**, 6, 33668.

38. N. Zhao, J. Qi, Z. Zeng, P. Parekh, C.-C. Chang, C.-H. Tung, Y. Zu, Transfecting the hard-to-transfect lymphoma/leukemia cells using a simple cationic polymer nanocomplex, *J. Control. Release* **2012**, 159, 104-110.

39. J.C. Aster, W.S. Pear, S.C. Blacklow, Notch Signaling in Leukemia, Annu. *Rev. Pathol.: Mech. Dis.* **2008**, 3, 587-613.

40. T. Palomero, A. Ferrando, Therapeutic Targeting of NOTCH1 Signaling in T-Cell Acute Lymphoblastic Leukemia, *Clin. Lymphoma Myeloma* **2009**, 9, S205-S210.

41. C.F. Adams, M.R. Pickard, D.M. Chari, Magnetic nanoparticle mediated transfection of neural stem cell suspension cultures is enhanced by applied oscillating magnetic fields, *Nanomedicine: Nanotechnology, Biology and Medicine* **2013**, 9, 737-741.

42. Na, H.-K.; Kim, H.; Son, J. G.; Lee, J. H.; Kim, J.-K.; Park, J.; Lee, T. G., Facile synthesis and direct characterization of surface-charge-controlled magnetic iron oxide nanoparticles and their role in gene transfection in human leukemic T cell. *Appl. Surf. Sci.* **2019**, 483, 1069-1080.

Chapter 5. Seed-Mediated Synthesis of Ultra-long Copper Nanowires and Their Application as Transparent Conducting Electrodes

5.1 Introduction

One-dimensional (1D) metal nanowires (NWs) have become one of the most appealing novel materials because of their unique properties such as catalytic activity, optical distinction, mechanical stability, and thermal resistance.[1-4] Therefore, tremendous effort has been devoted to the synthesis and applications of metal NWs.[5] Recently, re-illumination of these materials has been required to understand the profound characteristics of metal NWs, including localized surface plasmon resonance (LSPR), bandgap tuning, and the quantum confinement effect.[6-7]

While metal NWs can be employed for diverse purposes, one of the most lucrative applications is NW-based transparent electrodes to overcome the limitations of indium tin oxide (ITO).[8-9] NW electrodes exhibit the best performance in terms of both price and conductivity among other transparent electrodes prepared with carbon nanotubes, graphene, metal thin films, and metal nanogrids.[10] Among the various metal elements, copper is attractive as an electrode material because of its low price, natural abundancy, and high electrical conductivity comparable to that of Ag. It is a key necessity that the obtained Cu NWs have both a high aspect ratio and a small diameter for the production of transparent electrodes.[11] Generally, Cu NWs were synthesized via reduction of a copper precursor using hydrazine in aqueous systems but they have a large diameter of particles at the end of wires and low dispersibility.[12] Recently, synthetic methods of Cu NWs in organic system by using Ni(acac)$_2$ catalyst and in liquid crystalline medium via Pt catalyst have been reported. They have a high aspect ratio and good dispersibility.[13-14] However, expensive cost of catalyst and possibility of contamination from existence of a different kind of metal limit to obtain its applications. To make use of the price competitiveness of Cu metal, it is imperative to develop a new synthetic pathway wherein Cu NWs with high aspect ratios and small diameters can be produced through a scalable batch process, without a toxic and expensive catalyst. However, it is still a challenging task to synthesize Cu NWs without a strong reducing agent or catalyst, as the reduction of Cu^{2+} ions to Cu metal is less favorable because of its low reduction potential. Furthermore, it is difficult to control the morphology of the synthesized Cu nanomaterials because the induction of different growth rates for each facet of a Cu nanostructure is formidable. Similarly, the formation of a Cu NW architecture is also difficult. The aforementioned drawbacks must be overcome to fabricate Cu NW-based transparent electrodes.

Therefore, in this work, a new, simple, and cost effective seed-mediated synthetic method for the production of Cu NWs using copper nanoparticles (NPs) as an intermediate structure is demonstrated.

The use of toxic and expensive chemicals can be avoided during the synthesis. In addition, exclusive one-directional growth of NWs from the intermediate structures is achieved. Finally, the performance of the obtained Cu NW-based transparent electrodes was investigated.

5.2 Experimental section

5.2.1 Materials

Chemicals for synthesis of Cu NWs, Cu(acac)$_2$ (97%), CuCl$_2$ (≥99.995%), and oleylamine (≥98%) were purchased from Sigma-Aldrich and used without further purification. Acetone and hexane were purchased from Samchun Chemical (Korea) and used as received. Slide glass 25.4×76.2mm with 1 mm thickness was used for fabrication of the transparent conductive film.”

5.2.2 Synthesis of Cu NWs

The typical synthetic process for Cu NWs consists of two steps; synthesizing seed and growth solution injection. In the typical synthesis, stock solution for growth of Cu NWs was prepared by reacting 1.83 mmol of CuCl$_2$ and 5 ml of oleylamine at 70 °C. A mixture solution containing 100 mg Cu(acac)$_2$ (0.38 mmol) and 10 ml of oleylamine was slowly heated to 230 °C and kept at this temperature for 120 min under inert atmosphere, resulting in the synthesis of copper nanoparticles (Cu NPs). Then the growth solution was injected rapidly to the Cu NPs solution. The resulting solution was kept at 200 °C for 12 h, and cooled under a flow of argon. The Cu NWs was washed with acetone and re-dispersed in hexane. The Cu^{2+} :Cl^{-} ratios were controlled to be 100:0, 50:50, and 0:100 by varying the relative feeding compositions of Cu(acac)$_2$ and CuCl$_2$. The Cl^{-}/Cu^{2+} ratio was calculated according to the following equation { (2[CuCl$_2$]) / ([Cu(acac)$_2$]+[CuCl$_2$]) }.

5.2.3. Fabrication of transparent conductive Cu NWs films

Transparent conductive films were fabricated by vacuum filtration and transfer onto substrate.[14] Typically, Cu NWs dispersed in hexane with various concentration were treated by sonication for 1 min, and filtered onto nitrocellulose membrane filter by vacuum filtration method. The Cu NWs coated filter membrane was placed on selective area of slide glass and the glass was dried in a vacuum oven at 80 ºC for 2 h with pressure for increase adhesion between the Cu NWs on membrane filter and slide glass. After that, the membrane filter was carefully removed by dissolving with acetone until the filter was completely dissolved out. The as-prepared fabricated transparent conducting electrodes is not conductive because of separation between NWs and organic surfactant on NWs. Therefore, this film was treated at 200 °C for 1 h under inert atmosphere to remove surfactants and increase contact between Cu NWs. By controlling the concentration of NWs in hexane, transparent conducting electrodes with diverse transmittances and sheet resistances can be fabricated.

5.2.4 Instrumentation

The morphology of the samples was investigated with transmission electron microscopy (TEM, JEOL, JEM-2100) operated at 200 kV and scanning electron microscopy (SEM, Hitachi, S-4800). The high power X-ray diffactometer (HPXRD) data were obtained with a Rigaku D/MAZX 2500V/PC using Cu Kα radiation (λ=1.54180 Å). UV/Vis spectra were taken on a SHIMADZU UV-1800 by using a quartz cuvette. In addition, characterization of fabricated transparent electrodes was conducted with R_s measurement using a probe station (Keithley 4200-SCS semiconductor parametric analyzer). X-ray photoelectron spectroscopy (XPS, Thermo Fisher Scientific, ESCALAB 250XI) spectra data was recorded to survey oxidation states of Cu NWs.

5.3 Result and discussion

Cu NWs were synthesized by a separation nuclei formation from growth step. Copper(II) chloride in oleylamine were injected to copper NPs solution and aged at 200 °C. Figures 5.1a and 5.1b show typical SEM images of the resultant Cu NWs with an average diameter of 21.9±3.8 nm, as measured from 45 NWs randomly selected from Figure 5.1b and a maximum length of 77.1 μm (Figure 5.2). The aspect ratio of the Cu NWs is approximately 3520. It was confirmed that the obtained materials are highly flexible metal NWs. The coffee ring effect was observed during sample preparation because of the strong Van der Waals forces exerted by oleylamine on the surface of the Cu NWs as artifacts.[15] HRTEM observation of the microstructure in the Cu NWs supports the fact the presence of two types of lattices, with corresponding lattice spacings of 0.208 nm and 0.181 nm (Figure 5.1c). The former lattice is associated with the 111 planes of Cu, and the latter is attributed to the 200 planes. In addition, the selected area electron diffraction (SAED) patterns consisted of [110] and [111] zone diffraction of the face-centered cubic structure (Figure 5.1d). This means that the growth direction of the Cu NWs is <110>. The set of diffraction patterns represented a 5-fold twinned structure surrounded by (100) facets grown in the <110> direction.[16] The XRD pattern in Figure 5.1e shows peaks (2θ) at 43.5 °, 50.6 °, 74.3 °, 90.0 °, and 95.2 ° for the (111), (200), (220), (311), and (222) planes of fcc Cu (JCPDS #03-1018), respectively. This reveals that the NWs are composed of pure copper without any trace of CuO or Cu_2O. No peaks for copper oxides or impurities of NWs were discernible in the XRD profile. However, the XRD is not proper for detection of trace of oxide because of the ultra-thin and amorphous oxide layers. To study of oxidation state of Cu NWs extensively, we monitored oxidation of synthesized Cu NWs with X-ray photoelectron spectra (XPS) which is powerful technique to detect oxidation state of copper (Figure 5.3).[17] Only trace peak of CuO was detected in as-synthesized Cu NWs. The schematic model of the synthesized Cu NWs is shown in Figure 5.1f.

In order to synthesize Cu NWs with a high aspect ratio and small diameter, the focus has been on the effect of chloride ions, which are known to suppress the growth of the (100) plane in Cu by self-adsorption. It has been proven that the use of $CuCl_2$ leads to the production of Cu NWs with a relatively high aspect ratio when compared to those in the experiments conducted with CuCl.[18-19] Therefore, we selected $CuCl_2$ as a precursor for production of Cu NWs, which would be used for the formation of Cu NWs as a growth solution along with oleylamine. As will be described in detail, the preparation of copper NPs as seeds was first attempted. Notably, copper NPs were successfully fabricated with the $Cu(acac)_2$ precursor only (Figure 5.4a). On the contrary, when $CuCl_2$ was employed in oleylamine without $Cu(acac)_2$, it was impossible to obtain any product until the

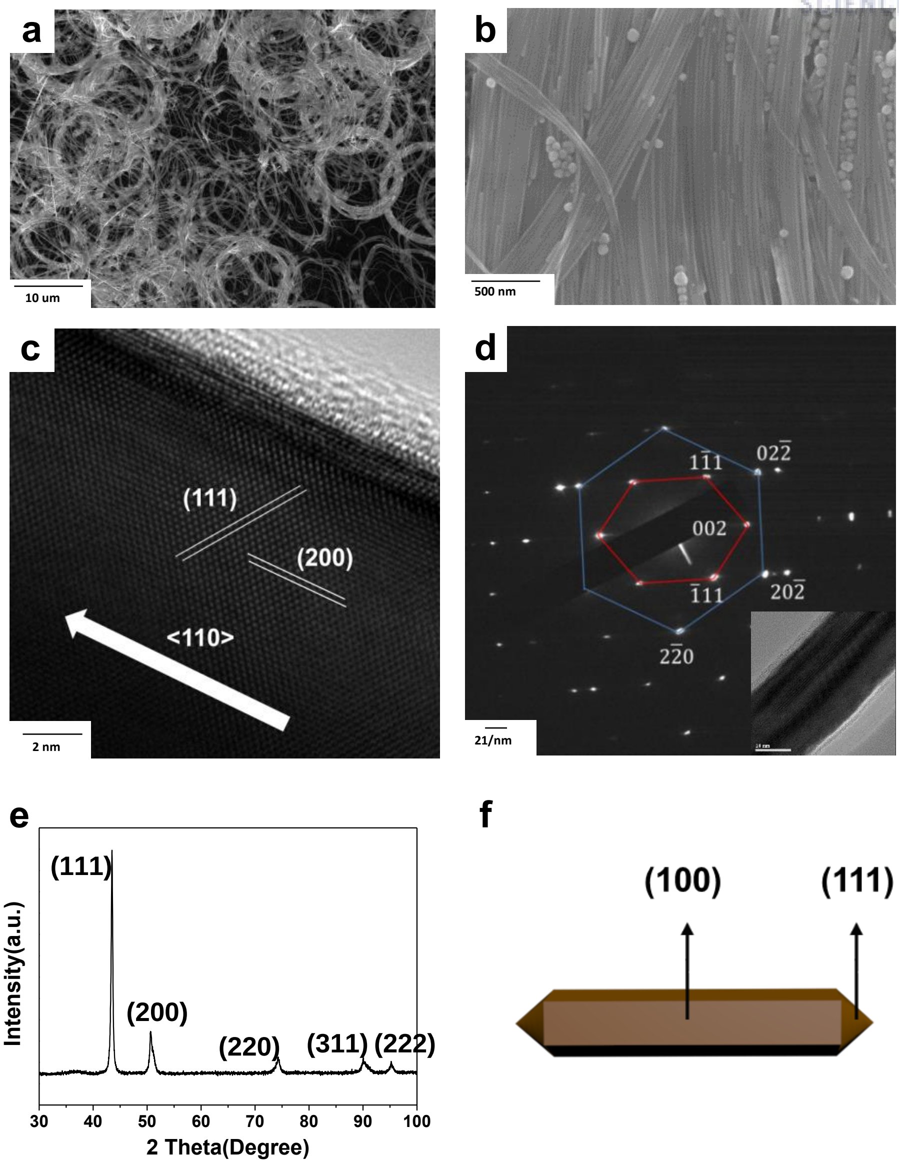

Figure 5.1. SEM images at (a) low and (b) high magnification, (c) HRTEM image, (d) SAED pattern, (e) XRD pattern, and (f) schematic model of the synthesized Cu NWs.[30] Reproduced in part with permission from H.H.Kim, et al., Applied Surface Science, 2017, 422, 731-737, Copyright 2013 ELSEVIER.

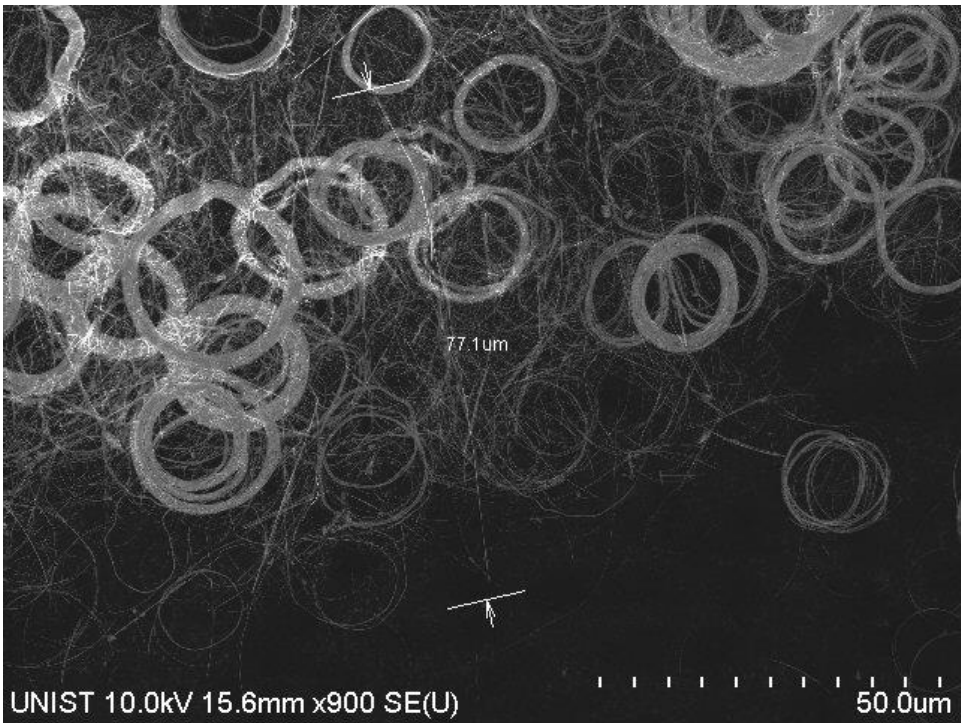

Figure 5.2. SEM image of the ultra-long Cu NWs.[30] Reproduced in part with permission from H.H.Kim, et al., Applied Surface Science, 2017, 422, 731-737, Copyright 2013 ELSEVIER.

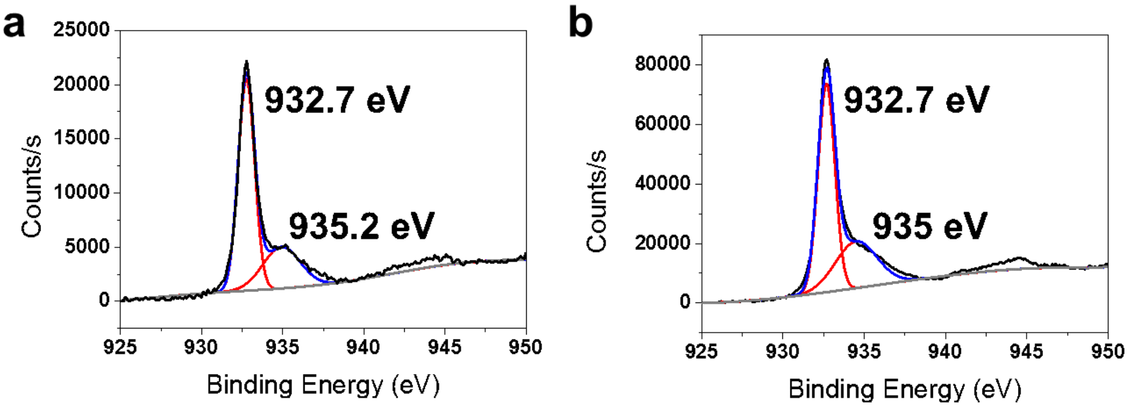

Figure 5.3. Cu 2p3/2 XPS spectrum of (a) as-synthesized Cu NWs and (b) Cu NWs kept at ambient condition for 15 days.[30] Reproduced in part with permission from H.H.Kim, et al., Applied Surface Science, 2017, 422, 731-737, Copyright 2013 ELSEVIER

temperature of solution reached 300 °C; this was because of the strong binding forces between the chloride ions and copper (Figure 5.4c).[13] The reaction solution remained yellowish transparent because of the presence of the metastable $CuCl_2$-oleylamine complex, as is well established.[20]

Accordingly, an additional experiment was conducted employing $Cu(acac)_2$ as a copper NP precursor and $CuCl_2$ in oleylamine as a growth solution. It could be inferred that $Cu(acac)_2$ not only played the role of NP precursor, but also aided in easy decomposition of the $CuCl_2$-oleylamine complexes through heating. Hence, it was expected that the decomposed components would act as nuclei for the growth of NWs. This strategy worked elegantly, but there was a limitation in that the nucleation and growth steps could not be clearly separated. As a consequence, a mixture of nanorods and NPs were obtained (Figure 5.4b).

To address this issue, the synthetic strategy was modified to separate the seed NP formation (nucleation) from the growth step. First, copper NPs were synthesized according to the method published elsewhere.[21] It was assumed that uniform and thin Cu NWs can be successfully prepared if the seed NPs could act as nucleation spots. This is considered reasonable because seed-mediated anisotropic growth is an accepted method.[22] However, this two-step process has been limited to special cases.[23-24]

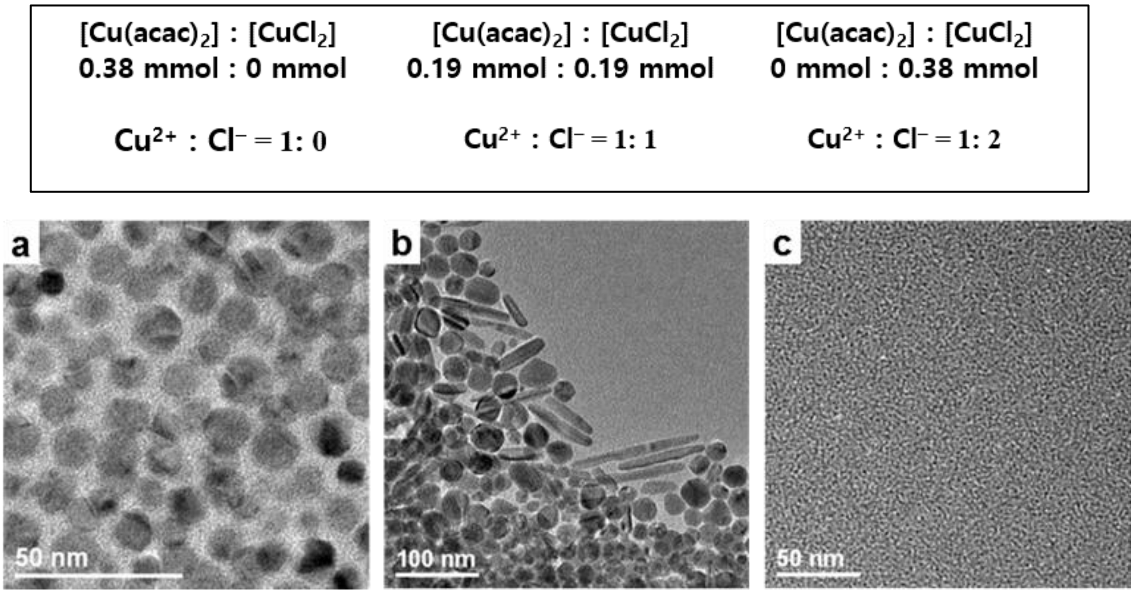

Figure 5.4. TEM images of products obtained under different chloride ion to copper ion ratios at (a) Cl−/Cu2+ = 0, (b) 1, and (c) 2.[30] Reproduced in part with permission from H.H.Kim, et al., Applied Surface Science, 2017, 422, 731-737, Copyright 2013 ELSEVIER.

Thus, the injection of $CuCl_2$ into the pre-existing solution and the presence of seed NPs are necessary prerequisites for obtaining Cu NWs. At the same time, a more systematic investigation on the effect of the $CuCl_2$ concentration and Cl^-/Cu^{2+} ratio would be quite valuable (Figure 5.4 and 5.5). It was essential to control the injected amount of $CuCl_2$ to monitor variations in the average diameter of the resulting Cu NWs. As the Cl^-/Cu^{2+} ratio in the injection solution increased, the apparent diameter of the Cu NWs decreased (Figure 5.5).

To examine the growth pathway, the external appearance of the reaction solution was monitored (Figure 5.6). A conspicuous color change during synthesis was observed with the naked eye. As soon as the copper NPs were synthesized, the solution turned purple black; the TEM image in Figure 5.7a shows that the average size is approximately 14.3 nm. After injection of the $CuCl_2$ solution, the solution color changed dramatically from purple black to pale brown within a few minutes (Figure 5.6a and 5.6b). This color change reflected that most of the NPs disappeared and only a small number of NPs remained intact in the solution. It is evident from Figure 5.7b that the average size of the NPs decreased from 14.3 nm to approximately 3 nm. This appeared to be a remarkable phenomenon that should be monitored. Finally, the UV spectra in Figure 5.7d is useful to provide evidence for the interesting occurrence depicted in Figure 5.7b. A strong plasmon resonance peak at 570 nm proved the presence of seed copper NPs in the solution before the $CuCl_2$ injection (top black line).[25] This peak diminished abruptly just after the $CuCl_2$ injection, and then, a new broad absorbance peak emerged (bottom blue line). This indicated that copper ion-oleylamine complexes were formed.[26] At the end of the reaction, a new plasmon peak (594 nm) was detected, which was associated with the prepared Cu NWs. It is important to understand the origin of the color change from purple black to pale brown along with the disappearance of the plasmon peak after injection of the the $CuCl_2$-oleylamine (growth solution). The most probable reason was the crumbling of the seed NPs *via* the following chemical reaction between the copper NPs and $CuCl_2$.[27]

$$CuCl_2 + \text{Cu NPs} \rightarrow 2CuCl$$

$$CuCl, CuCl_2 + \text{Cu seeds} \rightarrow \text{Cu NWs}$$

Cuprous ions are produced by the reaction between cupric ions and copper metal. Formation of smaller seed NPs by this reaction after the injection of $CuCl_2$ is the most crucial point for Cu NW formation. That is, the surviving seed NPs could act as nuclei

for unidirectional Cu NW growth. The high lattice energy of the created Cu nuclei may be an effective means to overcome the strong binding energy between copper and chloride ions. It is proposed that the surviving nuclei must have twin boundary defects because this structure can minimize their surface energy, so the final Cu NWs have a 5-fold twinned structure.[28]

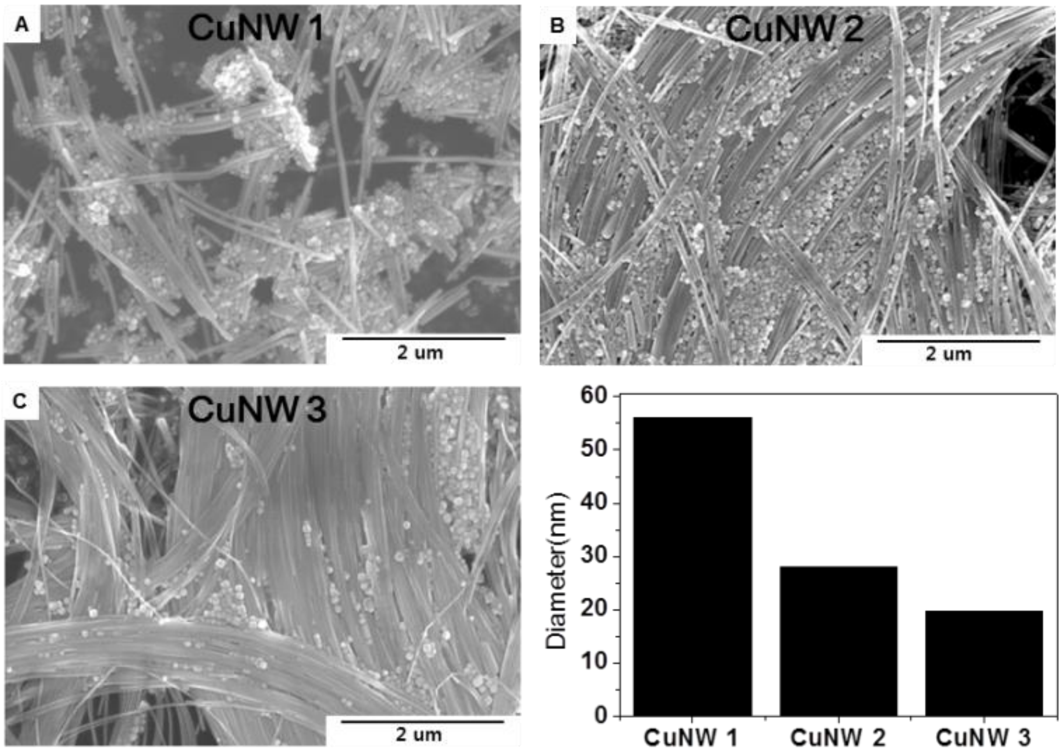

Figure 5.5. SEM images of Cu NWs synthesized with different amount of $CuCl_2$ (a) 0.92, (b) 1.29, and (c) 1.83 mmol.[30] Reproduced in part with permission from H.H.Kim, et al., Applied Surface Science, 2017, 422, 731-737, Copyright 2013 ELSEVIER.

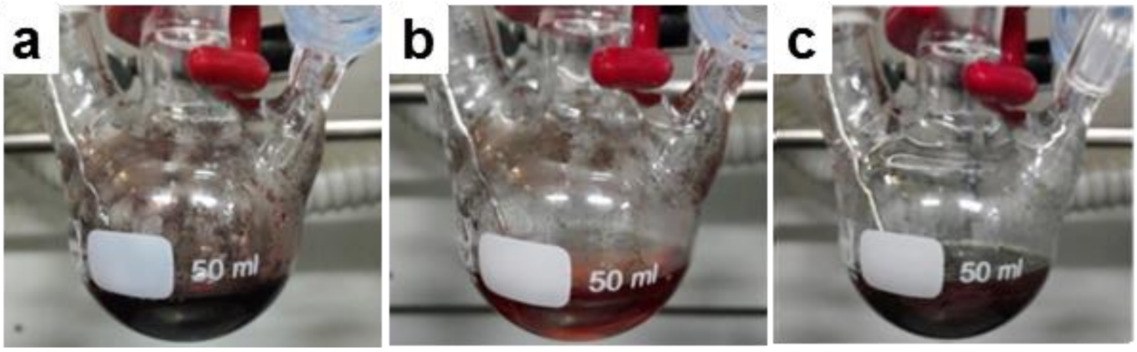

Figure 5.6. Photographs of a reaction vessel (a) before the injection of growth solution, (b) at 5 min, and (c) at 12 h after the injection of growth solution.[30] Reproduced in part with permission from H.H.Kim, et al., Applied Surface Science, 2017, 422, 731-737, Copyright 2013 ELSEVIER.

To confirm the reasoning outlined here and to prove the significance of the NP crumbling process, a complementary experiment was performed. In this experiment, instead of a blue $CuCl_2$ growth solution, a pale yellowish metastable $CuCl_2$-oleylamine compound solution was prepared and added to the copper NP intermediate solution. In this case, it was impossible to observe any color change after injection (metastable compound solution) step. Large irregularly shaped clusters of copper metal were generated (Figure 5.8). This indirectly supported the relevance of the proposed method and the importance of the seed forming step.

Considering all these observations, the growth mechanism is outlined in Figure 5.9. It is noteworthy that this mechanism is noticeably different from typical mechanisms, such as the solution-liquid-solid (SLS) or solution-solid-solid (SSS) mechanism.[29]

Finally, it has been accepted that Cu NWs have excellent electrical and optical properties owing to the nanoscale architecture. Thus, transparent electrodes were fabricated with the synthesized Cu NWs. Figure 5.10 depicts the transmittance of the Cu NW electrodes as a function of wavelength (UV/Vis) and sheet resistance. Sheet resistance was regulated by varying the amount of Cu NWs coated onto a glass substrate. The electrodes exhibited reliable transparency over the entire UV/Vis region, with a reasonable sheet resistance. In general, the transmittance is inversely proportional to sheet resistance. However, the sheet resistance is only 146 ohm/sq at even 87% transmittance. Figure 5.10c shows the corresponding SEM image of as-prepared transparent conducting electrodes with transmittances of 72% and demonstrate that continuous networks between Cu NWs were successfully created. This high performance originates from the inherent advantages of Cu NWs. The percolation threshold became significantly lower because of the high aspect ratio of the Cu NWs.

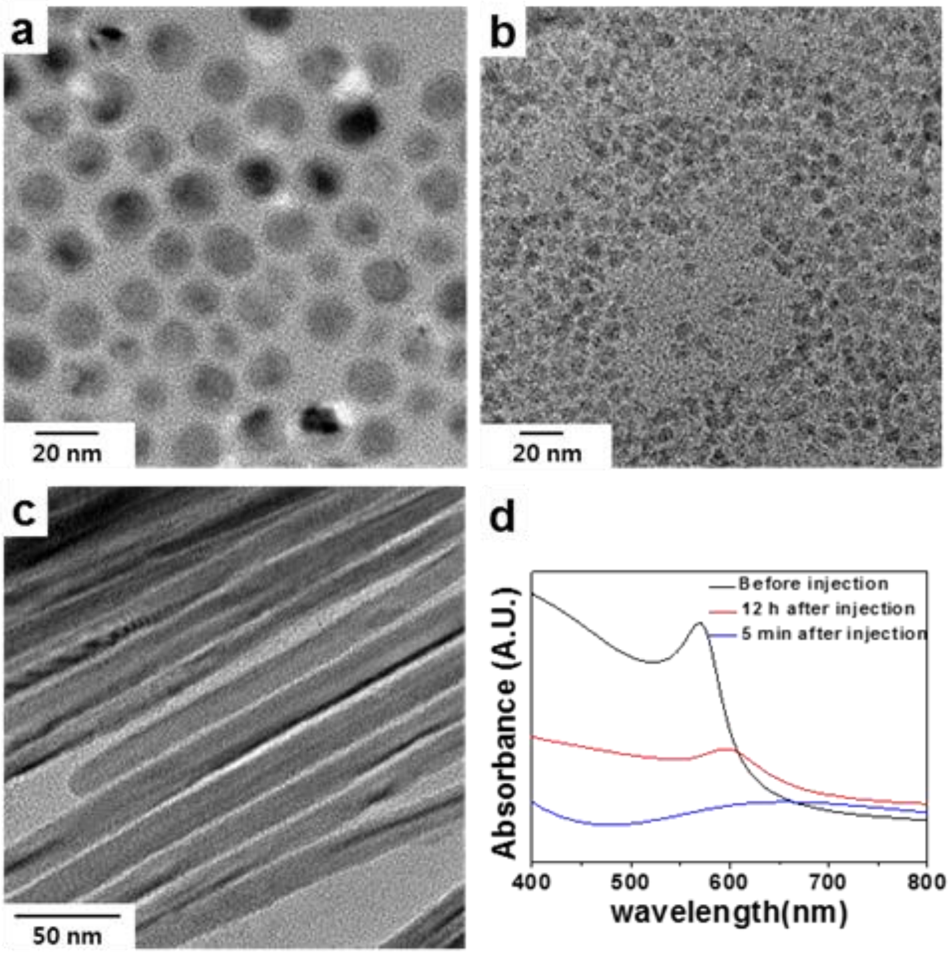

Figure 5.7. TEM images of copper nanoparticles obtained (a) before injection, (b) 5 min, (c) 12 h after injection of growth solution, and (d) UV/Vis spectra obtained from corresponding solutions.[30] Reproduced in part with permission from H.H.Kim, et al., Applied Surface Science, 2017, 422, 731-737, Copyright 2013 ELSEVIER.

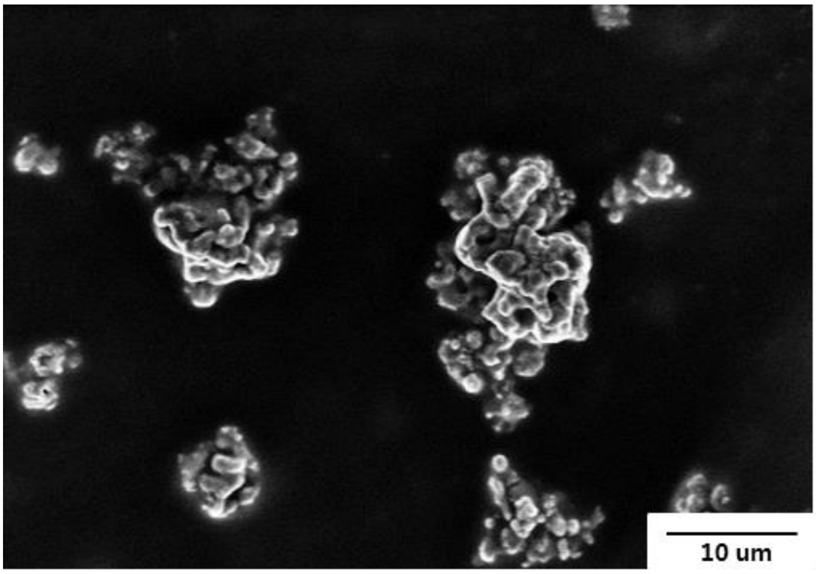

Figure 5.8. SEM image of irregular shaped large clusters of copper metal synthesized by injection of metastable $CuCl_2$-Oleylamine.[30] Reproduced in part with permission from H.H.Kim, et al., Applied Surface Science, 2017, 422, 731-737, Copyright 2013 ELSEVIER.

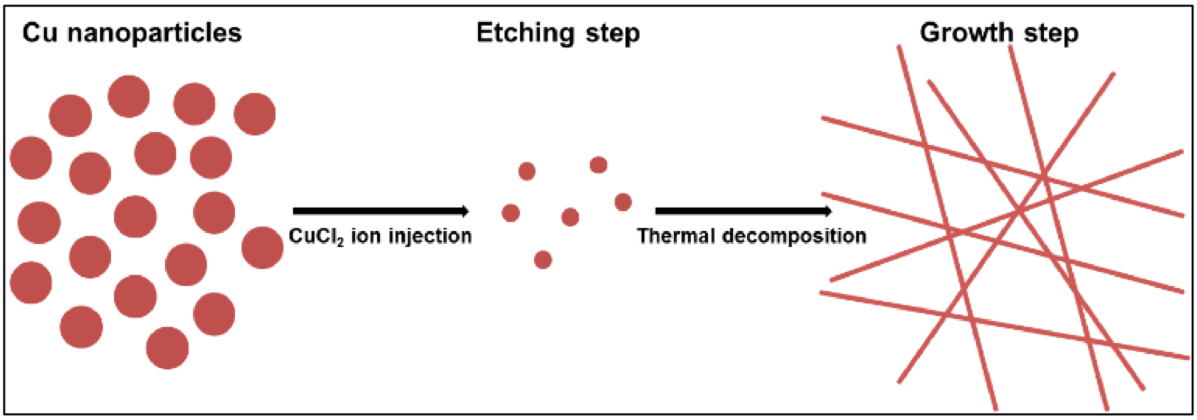

Figure 5.9. Proposed growth mechanism of Cu NWs.[30] Reproduced in part with permission from H.H.Kim, et al., Applied Surface Science, 2017, 422, 731-737, Copyright 2013 ELSEVIER.

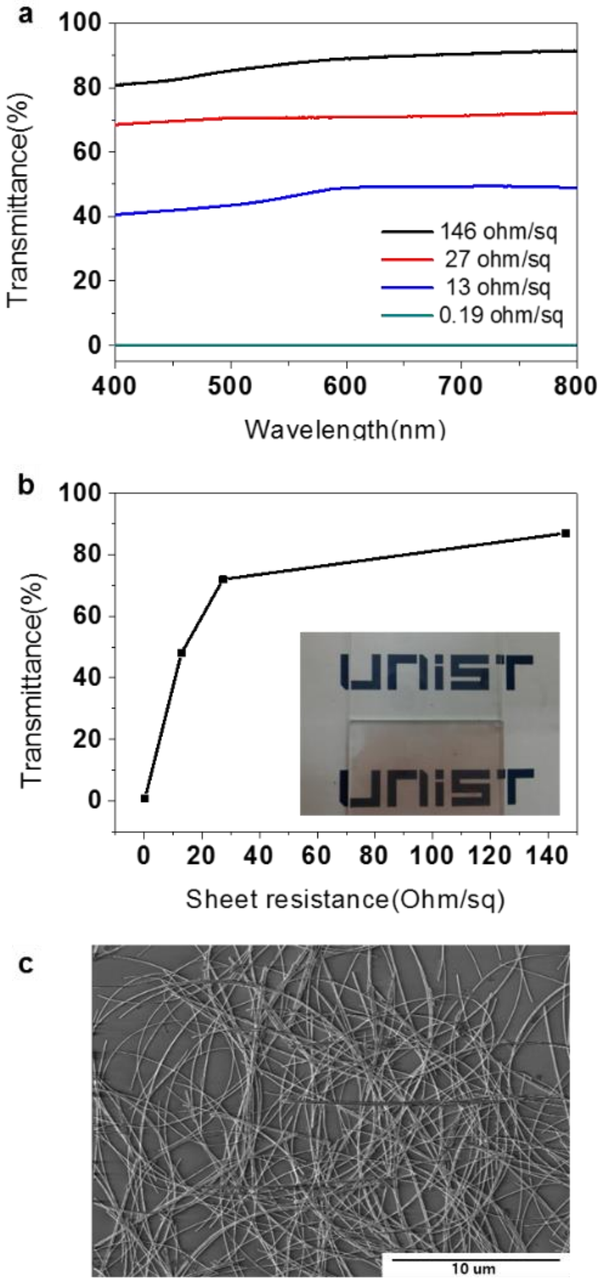

Figure 5.10. (a) Transmittance spectra of transparent electrodes containing Cu NWs for UV/Vis range depending on sheet resistance, (b) Transmittance *vs* sheet resistance relationship for various electrodes having Cu NWs at 500 nm wavelength, and (c) the corresponding SEM image of as-prepared transparent conducting electrodes with transmittances of 72%.[30] Reproduced in part with permission from H.H.Kim, et al., Applied Surface Science, 2017, 422, 731-737, Copyright 2013 ELSEVIER.

5.4 Conclusion

In summary, a new synthetic method has been demonstrated for Cu NWs that possess a high aspect ratio (~3520) and high crystallinity, without the use of expensive catalyst in a wet batch process. Control over subtle interactions between copper and chloride ions by tuning the stoichiometry and experimental parameters was the key to obtaining ultra-long Cu NWs. The reaction pathway was unique and distinctive as compared with conventional mechanisms, in which the unidirectional growth triggered by formation and crumbling of the seed NPs played a critical role. The excellent performance and economic feasibility might make Cu NWs a strong candidate for transparent conducting electrodes.

5.5 References

1. J. Liang, L. Li, X. Niu, Z. Yu, Q. Pei, Elastomeric polymer light-emitting devices and displays, *Nat. Photonics* **2013**, 7, 817-824.

2. J. Hu, T.W. Odom, C.M. Lieber, Chemistry and Physics in One Dimension: Synthesis and Properties of Nanowires and Nanotubes, *Acc. Chem. Res.* **1999**, 32, 435-445.

3. Y.-C. Yao, X.-R. Dai, X.-Y. Hu, S.-Z. Huang, Z. Jin, Synthesis of Ag-decorated porous TiO2 nanowires through a sunlight induced reduction method and its enhanced photocatalytic activity, *Appl. Surf. Sci.* **2016**, 387, 469-476.

4. F. Hoeng, A. Denneulin, N. Reverdy-Bruas, G. Krosnicki, J. Bras, Rheology of cellulose nanofibrils/silver nanowires suspension for the production of transparent and conductive electrodes by screen printing, *Appl. Surf. Sci.* **2017**, 394, 160-168.

5. A. Khalil, B. Singh Lalia, R. Hashaikeh, M. Khraisheh, Electrospun metallic nanowires: Synthesis, characterization, and applications, *J. Appl. Phys.* **2013**, 114, 171301.

6. Z.Y. Bao, D.Y. Lei, J. Dai, Y. Wu, In situ and room-temperature synthesis of ultra-long Ag nanoparticles-decorated Ag molybdate nanowires as high-sensitivity SERS substrates, *Appl. Surf. Sci.* **2013**, 287, 404-410.

7. A.V. Akimov, A. Mukherjee, C.L. Yu, D.E. Chang, A.S. Zibrov, P.R. Hemmer, H. Park, M.D. Lukin, Generation of single optical plasmons in metallic nanowires coupled to quantum dots, *Nature* **2007**, 450, 402-406.

8. D. Repetto, M.C. Giordano, C. Martella, F. Buatier de Mongeot, Transparent aluminium nanowire electrodes with optical and electrical anisotropic response fabricated by defocused ion beam sputtering, *Appl. Surf. Sci.* **2015**, 327, 444-452.

9. L. Hu, H.S. Kim, J.-Y. Lee, P. Peumans, Y. Cui, Scalable Coating and Properties of Transparent, Flexible, Silver Nanowire Electrodes, *ACS Nano* **2010**, 4, 2955-2963.

10. L. Hu, H. Wu, Y. Cui, Metal nanogrids, nanowires, and nanofibers for transparent electrodes, *MRS Bull.* **2011**, 36, 760-765.

11. C. Hwang, J. An, B.D. Choi, K. Kim, S.-W. Jung, K.-J. Baeg, M.-G. Kim, K.M. Ok, J. Hong, Controlled aqueous synthesis of ultra-long copper nanowires for stretchable transparent conducting electrode, *J. Mater. Chem. C* **2016**, 4, 1441-1447.

12. A.R. Rathmell, S.M. Bergin, Y.-L. Hua, Z.-Y. Li, B.J. Wiley, The Growth Mechanism of Copper Nanowires and Their Properties in Flexible, Transparent Conducting Films, *Adv. Mater.* **2010**, 22, 3558-3563.

13. H. Guo, N. Lin, Y. Chen, Z. Wang, Q. Xie, T. Zheng, N. Gao, S. Li, J. Kang, D. Cai, D.-L. Peng, Copper Nanowires as Fully Transparent Conductive Electrodes, *Sci. Rep.* **2013**, 3.

14. D. Zhang, R. Wang, M. Wen, D. Weng, X. Cui, J. Sun, H. Li, Y. Lu, Synthesis of Ultralong Copper Nanowires for High-Performance Transparent Electrodes, *J. Am. Chem. Soc.* **2012**, 134, 14283-14286.

15. R.D. Deegan, O. Bakajin, T.F. Dupont, G. Huber, S.R. Nagel, T.A. Witten, Capillary flow as the cause of ring stains from dried liquid drops, *Nature* **1997**, 389, 827-829.

16. H. Dong, M. Zhu, J.A. Yoon, H. Gao, R. Jin, K. Matyjaszewski, One-Pot Synthesis of Robust Core/Shell Gold Nanoparticles, *J. Am. Chem. Soc.* **2008**, 130, 12852-12853.

17. C. Lu, L. Qi, J. Yang, X. Wang, D. Zhang, J. Xie, J. Ma, One-Pot Synthesis of Octahedral Cu2O Nanocages via a Catalytic Solution Route, *Adv. Mater.* **2005**, 17 2562-2567.

18. E. Ye, S.-Y. Zhang, S. Liu, M.-Y. Han, Disproportionation for Growing Copper Nanowires and their Controlled Self-Assembly Facilitated by Ligand Exchange, *Chem. –Eur. J.* **2011**, 17, 3074-3077.

19. M. Jin, G. He, H. Zhang, J. Zeng, Z. Xie, Y. Xia, Shape-Controlled Synthesis of Copper Nanocrystals in an Aqueous Solution with Glucose as a Reducing Agent and Hexadecylamine as a Capping Agent, *Angew. Chem. Int. Ed.* **2011**, 50, 10560-10564.

20. S. Mourdikoudis, L.M. Liz-Marzán, Oleylamine in Nanoparticle Synthesis, *Chem. Mater.* **2013**, 25, 1465-1476.

21. S. Uk Son, I. Kyu Park, J. Park, T. Hyeon, Synthesis of Cu_2O coated Cu nanoparticles and their successful applications to Ullmann-type amination coupling reactions of aryl chlorides, *Chem. Commun.* **2004**, 778-779.

22. C.J. Murphy, N.R. Jana, Controlling the Aspect Ratio of Inorganic Nanorods and Nanowires, *Adv. Mater.* **2002**, 14, 80-82.

23. A. Gole, C.J. Murphy, Seed-Mediated Synthesis of Gold Nanorods: Role of the Size and Nature of the Seed, *Chem. Mater.* **2004**, 16, 3633-3640.

24. H.-J. Yang, S.-Y. He, H.-Y. Tuan, Self-Seeded Growth of Five-Fold Twinned Copper Nanowires: Mechanistic Study, Characterization, and SERS Applications, *Langmuir* **2013**, 30, 602-610.

25. J.C. Scaiano, K.G. Stamplecoskie, G.L. Hallett-Tapley, Photochemical Norrish type I reaction as a

tool for metal nanoparticle synthesis: importance of proton coupled electron transfer, *Chem. Commun.* **2012**, 48, 4798-4808.

26. M. Karbarz, J. Romanski, K. Michniewicz, J. Jurczak, Z. Stojek, Influence of polymer network-metal ion complexation on the swelling behaviour of new gels with incorporated [small alpha]-amino acid groups, *Soft Matter* **2010**, 6, 1336-1342.

27. O. Cakir, Copper etching with cupric chloride and regeneration of waste etchant, *J. Mater. Process. Technol.* **2006**, 175, 63-68.

28. J. Chen, B.J. Wiley, Y. Xia, One-Dimensional Nanostructures of Metals: Large-Scale Synthesis and Some Potential Applications, *Langmuir* **2007**, 23, 4120-4129.

29. A.J. Wooten, D.J. Werder, D.J. Williams, J.L. Casson, J.A. Hollingsworth, Solution−Liquid−Solid Growth of Ternary Cu−In−Se Semiconductor Nanowires from Multiple- and Single-Source Precursors, *J. Am. Chem. Soc.* **2009**, 131, 16177-16188.

30. Kim, H.; Choi, S.-H.; Kim, M.; Park, J.-U.; Bae, J.; Park, J., Seed-mediated synthesis of ultra-long copper nanowires and their application as transparent conducting electrodes. *Appl. Surf. Sci.* **2017**, 422, 731-737.

Acknowledgement

낯선 울산에서 길고도 짧았던 20 대를 보내며 많은 사람들의 도움과 응원으로 이 논문을 쓸 수 있었습니다. 새로운 지식뿐 아니라 삶을 대하는 태도, 소중한 인연을 만들 수 있었던 의미 있는 시간이었고 꿈을 키워갈 수 있던 소중한 장소이기도 합니다. 그 마음을 표현하기엔 부족하지만 짧게나마 이 글로 감사의 마음을 표현하고 싶습니다.

먼저, 부족한 저에게 아낌없는 가르침을 주시고 항상 따듯한 관심과 사랑으로 대해 주셨던 저의 은사 박종남 교수님께 진심으로 감사드립니다. 연구를 사랑하시는 교수님을 만날 수 있었던 것이 제 삶 가장 큰 행운이라 생각하며, 아낌없이 베푸시는 교수님 가까이에서 느낀 열정, 삶의 자세들은 앞으로 제 삶에 있어서 가장 중요한 양분이 될 것이라 생각합니다. 또한 바쁘신 와중에도 심사를 해주신 김소연 교수님, 손재성 교수님, 강세병 교수님, 그리고 홍성유 교수님께도 감사의 말씀드립니다.

연구실에서 만났던 선배와 후배, 동기분들께도 감사드립니다. 가장 가까운 곳에서 동고동락하며 만들었던 잊지 못할 추억과 경험들은 평생의 자산이 될 것입니다. 앞으로 실험실을 꾸려갈 추진력이 남달랐던 성환이형, 듬직한 현중이형, 긍정적이고 인자한 용훈이형, 번뜩이는 연구 아이디어가 많은 강용이 그리고 결혼하여 행복할 일들을 앞둔 선영누나. 앞으로 좋은 일 가득하기를 진심으로 바랍니다. 그리고 처음 실험실에서 만나 실험을 배울 수 있었던 창진이형, 기철이형, 대철이형, 그리고 충호형께도 감사드립니다. 먼저 졸업해서 꿈을 위해 공부중인 박사 요한이형, 짧은 시간이지만 함께했던 은별이, 진희, 임경이, 동우, 성현이형, 진환이, 태윤이, 창훈이형, 혜원이, 성원이에게도 감사합니다.

울산에 대학교를 처음 왔을 때부터 정말 가족처럼 지내왔던 친구들에게도 진심의 감사 메시지를 보냅니다. 대학원 다니는 동안 많은 힘이 되어준 준영이형, 재화형, 양석이형, 원경이형, 정말 고마웠고 함께한 즐거운 경험들이 힘들 때 마다 힘이 되어 줄 것 같습니다.

마지막으로 언제나 든든한 버팀목이 되어 주신 부모님에게 진심으로 감사합니다. 저를 키우느라 고생하셨을 시간과 그간 베풀어 주신 평생을 갚지 못할 은혜를 마음 속 깊이 새기고 살아가겠습니다. 집안의 희망 동생 태홍이, 앞으로 행복하고 좋은 일만 있을 태홍이게도 고맙다는 말을 전합니다.

2019 년 12 월

울산에서

Curriculum Vitae

Kim Hyunhong

School of Energy and Chemical Engineering

Ulsan National Institute of Science and Technology (UNIST)

UNIST-gil 50, Ulsan 689-798, Republic of Korea

Date of Birth: Feb 3rd, 1992

Email: kkh2008@unist.ac.kr

Education

2013 – 2019	Ulsan National Institute of Science and Technology (UNIST) M.S. & Ph.D. in Chemical Engineering Research advisor: Prof. Jongnam Park
2009 – 2013	Ulsan National Institute of Science and Technology (UNIST) B.S. in Interdisciplinary Green Energy
2007 – 2008	Gyeonggibuk Science High School

Research Interests

- ✓ Colloidal synthesis of inorganic nanomaterials
- ✓ Surface engineering of nanoparticles
- ✓ Design and synthesis of polymeric ligand
- ✓ Bio-molecular conjugation chemistry

Honors and Awards

2018 – present	Scholarship, LG hausys
2009 – present	Graduate School Scholarship, UNIST
2009 – 2013	Undergraduate School Scholarship, UNIST

Research Publications

1. Chungho Kim, Jin Wook Kim, **Hyunhong Kim**, Dong Hyeon Kim, Changhoon Choi, Yoon Seok Jung, and Jongnam Park*,
   "Graphene Oxide Assisted Synthesis of Self-assembled Zinc Oxide for Lithium-Ion Battery Anode" ***Chem. Mater.*** 2016, 28, 8498.
2. **Hyunhong Kim**, Seong-Hyeon Choi, Mijung Kim, Jang-Ung Park, Joonwon Bae*, and Jongnam Park*,
   "Seed-Mediated Synthesis of Ultra-long Copper Nanowires and Their Application as Transparent Conducting Electrodes" ***Appl. Surf. Sci.*** 2017, 422, 731.
3. Hyewon Jeong, Sinmyung Yoon, Jung Hwa Kim, Do-Hyun Kwak, Da Hwi Gu, Seung Hwae Heo, **Hyunhong Kim**, Sangmin Park, Hyeong Woo Ban, Jongnam Park, Zonghoon Lee, Jong-Soo Lee, Kwangjin An*, and Jae Sung Son*,
   "Transition Metal-Based Thiometallates as Surface Ligands for Functionalization of All-Inorganic Nanocrystals" ***Chem. Mater.*** 2017, 29, 10510.
4. Chungho Kim†, **Hyunhong Kim†**, Yonghoon Choi, Han Ah Lee, Yoon Seok Jung and Jongnam Park*,
   "Facile Method to Prepare for the Ni_2P Nanostructures with Controlled Crystallinity and Morphology as Anode Materials of Lithium Ion Batteries" ***ACS OMEGA*** 2018, 3, 7655.

   † These authors contributed equally to this work
5. Na Kyung Kwon, **Hyunhong Kim**, Im Kyung Han, Tae Joo Shin, Hyun-Wook Lee, Jongnam Park,*, and So Youn Kim*,
   "Enhanced Mechanical Properties of Polymer Nanocomposites Using Dopamine-Modified Polymers at Nanoparticle Surfaces in Very Low Molecular Weight Polymers" ACS Macro Lett. 2018, 7, 962.
6. Seungon Jung†, Hyeonjung Kim†, Junghyun Lee†, Gyujeong Jeong, **Hyunhong Kim**, Jongnam Park*, and Hyesung Park*
   "Bio-Inspired Catecholamine-Derived Surface Modifier for Graphene-Based Organic Solar Cells" ***ACS Appl. Energy Mater.*** 2018, 1, 6463.
7. Hee-Kyung Na†, **Hyunhong Kim†**, Jin Gyeong Son †, Ji Hong Lee, Jeong-Kwon Kim, Jongnam Park* and Tae Geol Lee*
   "Facile synthesis and direct characterization of surface-charge-controlled magnetic iron oxide

nanoparticles and their role in gene transfection in human leukemic T cell" ***Appl. Surf. Sci.*** 2019, 483, 1069.
† These authors contributed equally to this work

8. Changjin Yang†, Doo Jin Lee†, **Hyunhong Kim†**, Kangyong Kim, Jinwhan Joo, Yong Bae Song, Yoon Seok Jung, and Jongnam Park*
"Synthesis of Nano-sized Urchin-shaped $LiFePO_4$ for Lithium Ion Batteries" ***RSC Adv.*** 2019, 9, 13714.

   † These authors contributed equally to this work

9. Nabanita Pal, Seunghyeok Im, Eun-Bum Cho*, **Hyunhong Kim**, and Jongnam Park*
"Superparamagnetic NiO-doped mesoporous silica flower-like microspheres with high nickel content" ***J. Ind. Eng. Chem.*** 2020, 81, 99.

10. Sunyoung Woo†, Soojin Kim†, Jung-Hwa Oh, **Hyunhong Kim**, Seokjoo Yoon*, and Jongnam Park *
"Charge-Modulated Synthesis of Iron Oxide Nanoparticles via Radical Polymerization with Reversible Addition-Fragmentation Chain Transfer for In Vitro and In Vivo Toxicity Evaluation"
To be submitted.

11. Junghoon Jahng, Jin Gyeong Son, **Hyunhong Kim**, Jongnam Park, Taegeol Lee* and Eun Seong Lee*

    "Direct chemical imaging of ligand functionalized single nanoparticle in heterodyne photo-induced force microscopy"
submitted.

12. **Hyunhong Kim†**, Hyeonjung Kim†, Suhwan Kim, Sunyoung Woo, Yu Jin Jung*, Sang Kyu Kwak*, and Jongnam Park*
"Molecularly smooth and conformal nanocoating by amine-mediated redox modulation of catechol"
† These authors contributed equally to this work
submitted.

13. **Hyunhong Kim†**, Seung Ho Yook†, Yonghoon Choi, Kwan Young Lee, Jongnam Park*, and Jin Young Kim*
"Synergistic Radical Scavengers between Catechol-derived Ligands and CeOx Nanocrystals for High Performance & Durability PEMFCs"
† These authors contributed equally to this work
To be submitted.

14. Na Kyung Kwon, Hyunhong Kim, Tae Joo Shin, Kay Saalwächter§, Jongnam Park*, and So Youn Kim*
"Autophobic Dewetting Controlled Particle Dispersion, Polymer Dynamics, and Rheological Properties in Polymer Nanocomposites with Highly Extended Short Grafted Polymers"
To be submitted.